Study of the Effects of Long Carbamate Chain on Indigoid-Based Donor-Acceptor Polymers for Organic Electronic Applications

by

Daniel Afzal

A thesis
presented to the University of Waterloo
in fulfillment of the
thesis requirement for the degree of
Master of Applied Science
in
Chemical Engineering

Waterloo, Ontario, Canada, 2022

Author's Declaration

I hereby declare that I am the sole author of this thesis. This is a true copy of the thesis, including any required final revisions, as accepted by my examiners. I understand that my thesis may be made electronically available to the public.

Abstract

Novel donor-acceptor polymers based on indigoid building blocks, hemi-isoindigo and isoindigo, with the substitution of long carbamate side chains were synthesized for organic solar cells (OSCs) and organic field-effect transistors (OFETs) applications. The effects of the thermo-cleavable carbamate side chain are studied to demonstrate the potential influence on efficiency and performance for solar cell and transistor applications, respectively.

Regarding the first topic of this thesis, it addresses third-generation solar cells, organic solar cells as a potential for renewable source of energy due to their advantages of having low cost, light weight, flexibility, and roll-to-roll printing. These organic solar cells (OSCs) encompass a bulk heterojunction model (BHJ) in which the donor polymer and acceptor are used as an active material to achieve high efficiency. Currently, the leading OSCs reach over 18 % with the introduction of non-fullerene acceptors with wide-bandgap polymers. In this work, we introduce a D-A (donor-acceptor) copolymer system where benzodiothiophene is the donor backbone unit combined with the coplanar (Z)-3-(thiophen-2-yl-methylene)-indolin-2- acceptor unit. The acceptor unit consists of an electron-withdrawing carbamate side chain to be used in the wide-bandgap donor polymer system for organic solar cells. It is theorized that the introduction of the carbamate chain will deepen the HOMO level of the polymer to improve the optical bandgap and result in a better V_{OC}. Furthermore, the thermal labile property of the carbamate chain can prove useful for organic solar cells. This is because before removing the chain, it gives a reasonable amount of solubility to the polymer so that it can be processed. Once the polymer is deposited, the chains can be removed by heat as previously studied by our group. This can further improve the polymer's molecular backbone by making it more coplanar as the bulky groups are removed. This enhances the π-π stacking as the charge hoping distance between the individual polymer molecules are increased. All in all, providing a higher FF and J_{SC}. Thus, ultimately increasing overall PCE.

Based on the structure alone, 2-decyltetradecyl (Z)-3-((5-(4,8-bis(5-(2-ethylhexyl)thiophen-2-yl)-6-methylbenzo[1,2-b:5,4-b']dithiophen-2-yl)thiophen-2-yl)methylene)-6-methyl-2-oxoindoline-1-carboxylate or TEIBDT exhibits a very coplanar structure useful towards achieving high PCE, has straight-forward synthesis as well as high quenching efficiency making it a promising candidate for OSCs. The solar cell device based on TEIBDT: Y6 blend film showed an adequate efficiency of 8.00% with J_{SC} of 20.60 $mAcm^{-2}$, V_{OC} of 0.70 V and FF of 0.56. The carrier mobilities of the film for hole and electron were calculated to be 1.06×10^{-4} $cm^2V^{-1}s^{-1}$ and 8.855×10^{-5} $cm^2V^{-1}s^{-1}$, respectively. The high PCE is attributed to good film morphology with good crystallinity.

The second topic of this thesis focuses on the application of organic field-effect transistors. Isoindigo is known for being an excellent acceptor building block for donor-acceptor polymers with the advantages of simple synthesis, excellent air stability and high electrical performance. Thus, in this study, we explore the impact of the thermo-cleavable carbamate chain for the potential enhancement of mobility, solvent resistance, and morphological stability. The theory is that the thermally removable carbamate side chains on the isoindigo unit can help form intermolecular hydrogen bonds, which can afford excellent solvent resistance and morphological stability while also enhancing π-π stacking to improve upon charge carrier mobility as the charge hoping distance between the individual polymer molecules are increased.

Moreover, this study focuses on three novel isoindigo polymers, PIDMT, PIDBT and PIDBDT and are evaluated based on their transfer characteristics, mobility, and solvent resistance. With regards to solvent resistance, all the polymers exhibited resistance towards processing solvents such as chloroform and toluene when annealed at 250 ºC. In terms of performance, the PID polymers displayed ambipolar characteristics with p-type mode being the dominant function. The mobility performance for PIDMT, PIDBT and PIDBDT are the following 0.004, 0.01 and 0.007 $cm^2V^{-1}s^{-1}$, respectively, for p-type and 0.001, 0.004, 0.005 $cm^2V^{-1}s^{-1}$, respectively, for n-type with PIDBT being dominant for both modes.

Acknowledgements

I would like to express my sincerest gratitude towards Dr. Yuning Li who has been a fantastic supervisor, adviser, and friend. The opportunity he gave me to pursue higher education in the field of chemical engineering is greatly appreciated and that I am much obliged. His knowledge and skills have been very beneficial to me during the length of my study project. His encouragement enabled me to improve my research abilities and widen my horizons in the fields of science and engineering. I am forever grateful for his support. In addition, I would like to express my gratitude to the Natural Sciences and Engineering Research Council of Canada Green Electronics Network (NSERC-GreEN) for providing financing assistance for my experiments.

I would also like to give special thanks to Dr. Jenner Ngai for being an amazing friend, mentor, and teacher. He has taught me the proper techniques for organic synthesis which has made organic synthesis fun and rewarding. Not only that, he has been a great listener who has helped me stay positive and optimistic throughout my graduate studies.

Furthermore, I would like to thank my colleagues, Dr. Keqiang He, Yi Yuan, Dr. Xiguang, Zhe Huang, Yao Yao, John Polena, Merlan Nurzhanov, and Scott Flynn for aiding me with polymer synthesis, polymer characterization, device fabrication and device testing.

Last but not least, I would like to express my gratitude to my parents, Waqar and Shazia Afzal, for all of the encouragement, support, and financial assistance they have provided. They have been there for me through the good times and the bad, and for that I am grateful.

Table of Contents

List of Figures

List of tables

List of Abbreviations and Symbols

AFM	Atomic force microscopy
BDT	Benzodithiophene
BGBC	Bottom-gate bottom-contact
BT	Bithiophene
$CDCl_3$	Deuterated chloroform
CV	Cyclic voltammetry
D-A	Donor-acceptor
DCM	Dichloromethane
DDTS	Dodecyltrichlorosilane
DFT	Density functional theory
DMF	N-N-dimethylformamide
DMSO	Dimethyl sulfoxide DMSO-d6: deuterated dimethyl sulfoxide
DSC	Differential scanning calorimetry
FET	Field-effect transistor
E_g opt	Optical energy bandgap
FF	Fill factor
GPC	Gel permeation chromatography
HOMO	Highest occupied molecular orbital
HT-GPC	High-temperature gel permeation chromatography
$I_{ON/IOFF}$	Current ON/OFF ratio
J_{SC}	Short-circuit current
PCE	Power conversion efficiency
LUMO	Lowest unoccupied molecular orbital
M_n	Number-average molar mass
MO:	Molecular orbital
MOSFET:	Metal-oxide semiconductor field-effect transistor

MT	Mono-thiophene
Mw	Weight-average molar mass
NMR	Nuclear magnetic resonance
OECT	Organic electrochemical transistor
OFET	Organic field-effect transistor
OLED	Organic light emitting diode
OPT	Organic phototransistor
OPV	Organic photovoltaic
OSC	Organic solar cell
OSC	Organic semiconductor
OFET	Organic field effect transistor
OTFT	Organic thin film transistor
RMS	Root mean square
RT	Room temperature
TFT	Thin film transistor
TGA	Thermogravimetric analysis
TGBC	Top-gate bottom-contact
UV-Vis	Ultraviolet-visible
V_{DS}	Drain-source voltage
V_G	Gate-source voltage
V_{OC}	Open-Circuit voltage
V_{ON}	On voltage
V_T	Threshold voltage
XRD	X-ray diffraction
μ	Charge carrier mobility

Other abbreviations and symbols are defined in the text

Chapter 1 Part: I
Introduction to Organic Solar Cells

1.1 Synopsis of Solar Cells

As global energy consumption has expanded over the past few decades, the world's reliance on natural resources has become increasingly inadequate to meet global demand and poses a severe threat towards the environment. This mainly consists of fossil fuels, which is a non-renewable energy source that accounts for 80% of the world's energy source and is responsible for 89 % of global CO_2 emissions according to the United Nations. [1-3] Therefore, a cleaner and more sustainable renewable energy source must be used to guarantee a long-term future. The most common renewable energy source that is both green and renewable is solar energy. This type of resource does not have any negative environmental impact due to generating energy via sunlight with zero gas emissions making this a perfect candidate to be used as a sustainable energy resource. For decades, first-generation inorganic single crystal-based silicon solar cells have been dominating the solar market due to their high efficiency, excellent stability and low-cost power generation making them excellent for residential homes that have open access to sunlight. The drawbacks, however, are their initial manufacturing cost, hefty weight and rigid structure that precludes their use in other applications such as portable electronic gadgets**,** textiles, vehicles, etc**.**[4-5]

The second generation of solar cells are referred to as inorganic semiconductors such as cadmium telluride (CdTe) and copper indium gallium diselenium (CuIGD). They can be manufactured at a cheaper cost because they utilize smaller amounts of material, but the problem arises when creating large quantities of thin-film solar cells with the same degree of efficiency as single crystal silicon solar cells.[4,6] The third generation of solar cells which is being actively investigated are organic solar cells (OSC). There are three significant reasons that make them a promising candidate for the future. The first reason involves solution processability in which the polymers are solution treated, allowing for high-throughput production of solar cell panels via employing printing technology.[4,7] Using printing technologies instead of traditional methods for making inorganic solar cells will result in significant savings in production costs while also boosting output. [6,8] Second, the lightweight and flexibility of organic materials give them potential for state-of-the-art design. Most OSCs are a thousand times thinner than a normal silicon solar cell, which is approximately the same thickness as a human hair.[6,8] And thus, they can be fabricated on curved surfaces such as the fabrics of tents, backpacks, and clothing. This also gives the potential for portable electronic gadgets such as cell phones, laptops, headphones etc. It's evident that with this technology, the possibilities for where solar cells can be used are greatly expanded beyond just rooftops and solar farms.[6,8] Finally, the third reason allows for limitless combinations of organic materials to fine-tune and optimize to satisfy the requirements of the applications. And thus because of these reasons, OSCs have been hailed as one of the most promising photovoltaic technologies. [6,8]

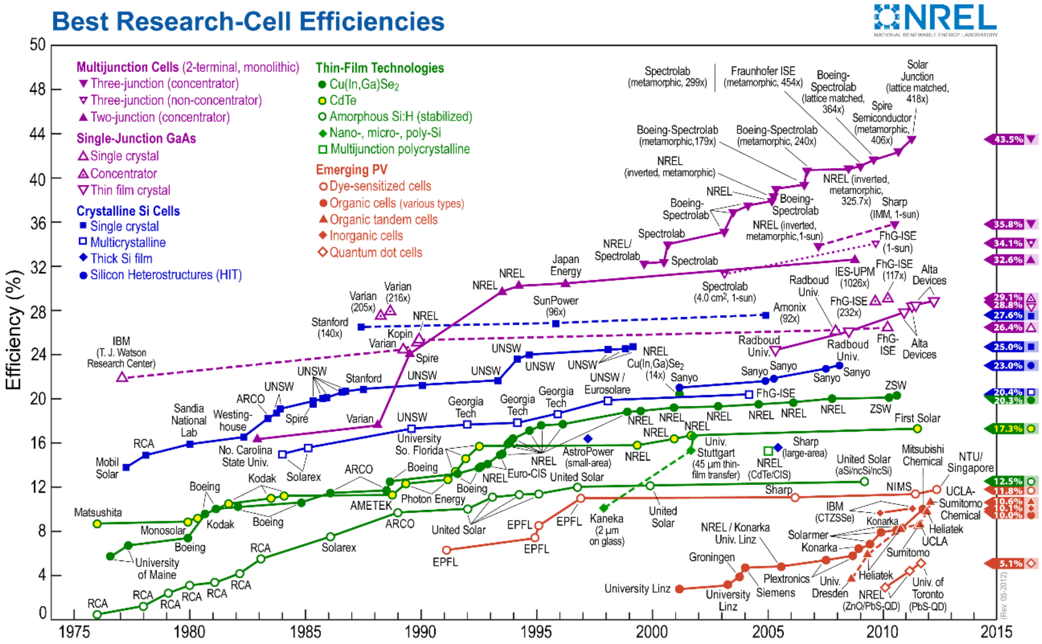

Figure 1-1 Evolution of Solar cell Technology [9]

1.2 Bulk Heterojunction (BHJ) Solar Cell

The first basic photovoltaic cell consisted of a planar junction in which the film is sandwiched between two contacts. The film contains the active layer such as a polymer or small molecule where excitons would be generated and would diffuse before recombining or separating. However, since the planar cells were thin, this meant films could not absorb light very well. Due to this disadvantage, BHJ junction types were developed to tackle carrier diffusion length by separating regions of each material by only a few nano meters. Following the invention of the first BHJ solar cell, OSC performance and stability have improved drastically.[10,12]

In a typical BHJ multilayer structure, the active layer is a mixture of a conjugated polymer donor and acceptor material. This active layer is inserted between the anode and cathode, which collects the holes and electrons. This ensures that the excitons can reach the donor-acceptor interface within a few nanometers, thus increasing the efficiency of the exciton dissociation as well as mitigating the limitations for film thickness.[10,12] Furthermore, the hole transport layer and electron transport layer are in between the anode-photoactive and cathode-photoactive layer to improve the performance and stability of the solar cell. Typically, the hole transport layer consists of MoO_3 or PEDOT: PSS which are effective materials to facilitate the collection of holes and blocking of electrons.[10,12] Whereas the electron transport layer consists of zinc oxide which is used to extract the electrons. The cathode or anode is composed of indium-doped tin oxide (ITO) metal which allows for the transmission of light. At the moment, an inverted device structure is used, with the bottom electrode serving as the cathode and the top electrode serving as the anode. This style of architecture maintains a higher level of environmental stability.[10,12] The schematic below illustrates the key differences between the conventional and inverted OSC structures.

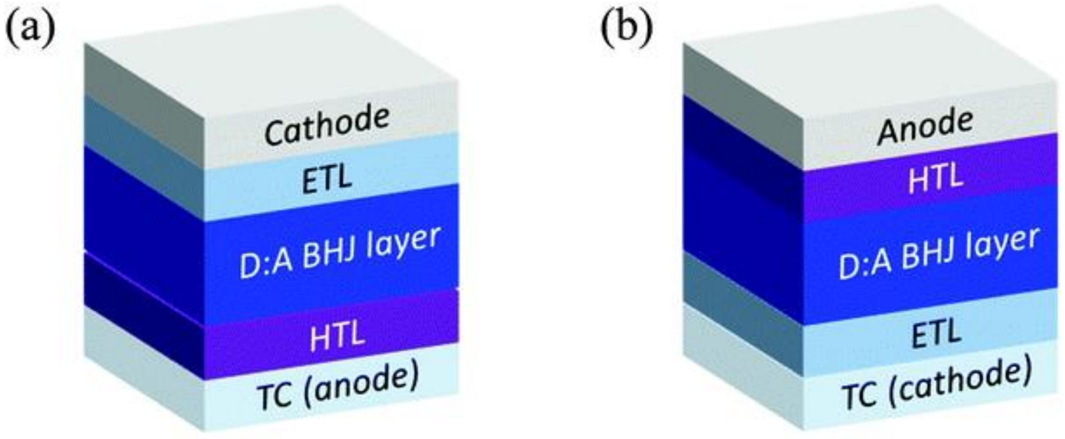

Figure 1-2 (a) Conventional OSC Structure [11] **(b)** Inverted OSC Structure [11]

1.3 The Working Principal of a BHJ Solar Cell

The mechanism of the BHJ solar cell can be described in four fundamental steps.

Step 1: **Exciton Generation.** As the light hits the photoactive layer, it is absorbed by the donor material. Upon absorption of the photon, the electron is excited from the HOMO to the LUMO, thus resulting in an electron-hole pair or excitons. The excitons are then migrated to the donor-acceptor interface.[10-12]

Step 2: **Exciton Diffusion and Splitting.** The break of Coulomb attraction occurs in LUMO between the donor and acceptor materials which causes the excitons to dissociate. Due to the limited lifetime of the excitons, it is imperative that the excitons must be generated within their diffusion length for efficient charge generation. As mentioned in step one, the holes generated at the donor/acceptor interface have a strong Columb binding in which it must be dissociated to get the free charge carriers. Charge transmission efficiency is contingent upon the efficient dissociation of excitons at the contact. Electrostatic forces are generated at the interface due to the difference in HOMO and LUMO between the donor and acceptor layers. When the materials are chosen properly, these differences provide an electric field that efficiently splits excitons into electrons and holes. Additionally, free electrons are accepted by materials with a greater LUMO level, while holes are accepted by materials with a lower HOMO level. Unfortunately, as they approach the electrodes, these free charge carriers may undergo recombination or become trapped in a disordered interpenetrating organic substance. Diffusion length can be defined as the distance travelled by an exciton before recombination.[10-12]

Step 3: **Charge Transportation**. Upon exciton dissociation into free charge carriers, the electrons are transferred to their respective electrodes via hopping from one localized state to the next. It is important to note that a bottleneck effect occurs during the transportation of charge carriers to the electrodes, in that they recombine before even reaching the electrodes. And thus, the charge carrier mobility in the active layer is important to minimize the recombination effect. The higher the mobility, the higher the chance of reaching the electrodes before recombination. [10-12]

Step 4: **Charge Collection**. If charge carriers are effectively transferred from the active layer to the electrode without recombination, the charge has been collected. This charge would then indicate the organic solar cell's photovoltaic performance. These performance parameters include but are not limited to J_{SC}, V_{OC}, and FF. [10-12]

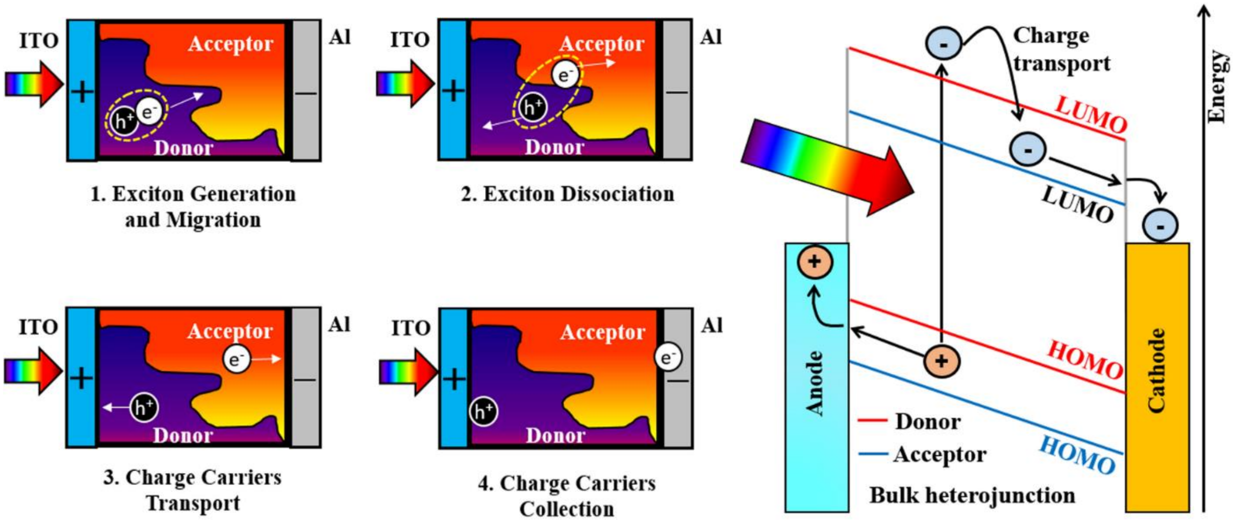

Figure 1-3 (a) Mechanism of BHJ Solar Cell [10] **(b)** BHJ Solar Cell Band Schematic [10]

1.4 Non-Fullerene Acceptors for Wide Bandgap Polymers

Fullerene acceptor (FA) materials were frequently used as the electron acceptor in OSCs in previous decades but recently have fallen off due to their restricted light absorption range, poor harvesting property, and poor synthetic flexibility. It is also reported that these acceptors are sensitive to light and oxygen making the performance degrade even quicker.[13] Their structures are similar to a bucky ball, containing both hexagons and pentagons. The most widely studied fullerene acceptors are $PC_{61}BM$ and $PC_{71}BM$ shown in **Figure 1-4**. Although the PCE for fullerene-based D-A polymers can be adequate, the constraints of the fullerene acceptors motivated the scientific community to produce a better acceptor.

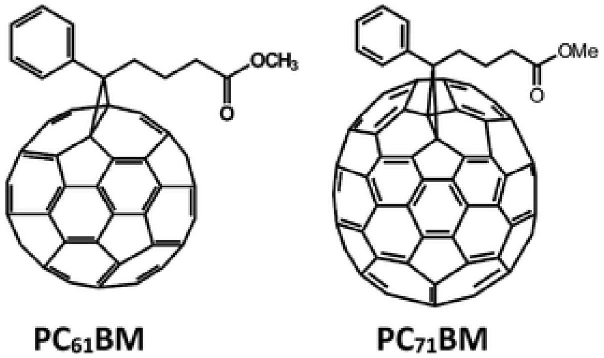

Figure 1-4 Structure of Fullerene Acceptor $PC_{61}BM$ and $PC_{71}BM$ [15]

As a result, non-fullerene materials have been more popular in OSCs. As of today, the highest PCE recorded is 18.22%.[14] Their flexible molecular structure allows for controlled light absorption spectrum expansion and the prospect of decreasing the energy barrier for charge transfer, resulting in improved optical and electrical features in OSCs. When compared to fullerene acceptors, NFA's is more promising in terms of morphological benefits, energy loss reduction, and absorption range expansion. Overall, a great candidate for the future of organic solar cells.

The resulting optical bandgap of a polymer can be divided into 3 distinct bands. A low bandgap (<1.6 eV), medium bandgap (1.6 eV <bandgap < 1.8eV) and wide bandgap (>1.8eV). A medium to wide bandgap is needed to form complementary absorption with non-fullerene acceptors. Usually, donor building blocks, involve thiophene moieties to match with NFA-based OSCs such as BDT due to its excellent electron-donating effect to tune E_{HOMO}, and its ability to maintain backbone coplanarity and its stability. Thus, good matching between donor and acceptor materials is necessary to achieve high efficiency. In this section, three non-fullerene acceptors are discussed, ITIC, IT-4F and Y6 which have been widely used to achieve excellent performance.[11-13]

In 2015, Lin et al., created a novel acceptor ITIC which has an electron-donating indacenodithienothiophene (IDTT) central unit, two electron-withdrawing 2-methylene-(3-(1,1-dicyanomethylene)-indanone) (IC) end groups with hexyl phenyl side chains to increase solubility and prevent excessive aggregation of molecules in the solid state. ITIC has a good SCLC mobility of $3.0 \times 10^{-4} cm^2V^{-1}s^{-1}$, which is almost identical to fullerene-based acceptors ($\sim 10^{-4}$-$10^{-2} cm^2V^{-1}s^{-1}$). It also has a high E_{LUMO} (-3.83 eV) which is vital to achieve a high V_{OC}.

However, its biggest restriction is the large bandgap (E_g = 1.59 eV), absorbing sunlight below 800 nm, which restricts J_{SC} when a wide band gap (WBG) polymer donor is used. Despite this, ITIC has been used on a large scale as a model acceptor in the investigation and development of a broad variety of polymer donors to give substantial insights into the structure-property–cell performance linkages of these polymer donors.[11]

Because of ITIC's huge restriction of J_{SC} due to the rather large bandgap (1.59 eV), Zhao et al. introduced fluorine atoms on the end of IC groups of ITIC to form IT-4F. This allowed a narrower bandgap of 1.52 eV with red-shifted absorption and higher $\alpha_{s\text{-max}}$ and $\alpha_{f\text{-max}}$ values along with lower E_{LUMO} (-4.14 eV) and E_{HOMO} (-5.66 eV). When compared to ITIC-based devices, OSCs based on IT-4F were shown to have superior photovoltaic performance. [11] Furthermore, in 2019, Yuan et al developed a more superior acceptor called Y6, a BT-based fused- core unit with 2FIC as the end groups. When compared with ITIC and IT-4F, Y6 has a narrower bandgap of 1.33 eV with a red-shifted optical absorption onset at 931 nm, and a higher α_{s-max} of $2.39 \times 10^5 \mathrm{M}^{-1}\mathrm{cm}^{-1}$.The absorption range of Y6 is 600–950 nm on the board, with the maximum absorption at approximately 810 nm. The absorption range may be expanded to roughly 1100 nm, allowing them to absorb infrared bands. The bandgap of Y6 is almost ideal for achieving the maximum PCE based on the Shockley–Queisser limit for single junction solar cells (at an E_g of 1.34 eV). The E_{LUMO} of -4.1 eV was between those of ITIC and IT-4F. Y6 is the only acceptor that has achieved the record PCE of 18.22% for OSCs so far. [11]

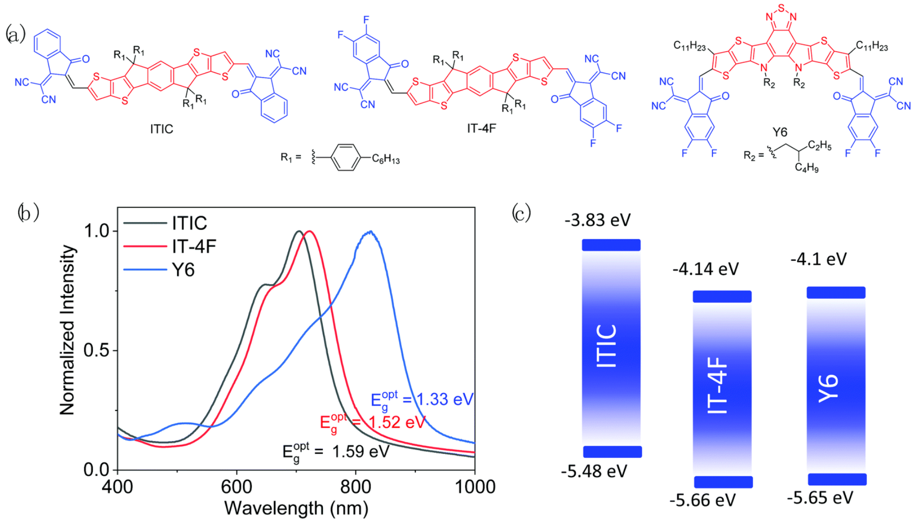

Figure 1-5 (a) Chemical Structures of ITIC, IT-4F and Y6 NFA's **(b)** UV-vis Spectra **(c)** Energy Level Diagram [11]

1.5 Defining OSC Performance Parameters

There are three critical characteristics that influence the power conversion efficiency (PCE) of organic solar cells. The first parameter refers to as short circuit current, J_{SC} which is the current that reaches the electrodes without any applied field. The second parameter is the open circuit voltage $V_{OC,}$ which is the maximum potential of the cell. The last parameter is the fill factor (FF) which refers to the quality of the cell. This is denoted by the ratio of the maximum obtained power to the product of J_{SC} and V_{OC}. [14]

1.5.1 The Influence of Short Circuit Density (J_{SC})

The impact of the J_{SC} on the PCE of a solar cell may be described by four processes that are linked to the solar cell's mechanism. The first process derives from the number of photons absorbed which is directly linked to the absorption coefficient (α) and the optical bandgap of the polymer donor. The second process is exciton diffusion which is influenced by the dielectric constant (ε), morphology and the electronic structure of the polymer. The third process involves exciton dissociation which is influenced by the electronic structure and the optical bandgap between the donor and acceptor. The last process, charge collection is determined by the balance ratio of the hole mobility of the donor and the electron mobility of the acceptor. As mentioned before, the higher the dielectric constant, the higher the chance to reduce exciton recombination. [10,16]

1.5.2 The Influence of Open Circuit Voltage (V_{OC})

To determine the maximum potential of a solar cell, the energy level of the LUMO of the acceptor and the energy level of the HOMO of the polymer donor are taken into account. The lower the HOMO of the polymer donor, the higher the V_{OC}. Additionally, a large dielectric constant can reduce the exciton binding energy which can help increase the V_{OC}.

1.5.3 The Influence of Fill Factor (FF)

As mentioned previously, the fill factor is referred to the quality of the solar cell. And is influenced by the hole mobility of the donor and its balance with the electron mobility of the acceptor. Typically, if the hole mobility and electron mobility are greater than $> 10^{-4}$ then the device should be able to achieve a high FF. To get good mobility, the structure of the polymer donor matters extensively. For example, side chain composition, side chain length, crystallinity, and film morphology all have a major impact on FF. Other examples include tuning of the surface of the film by additives such as DIO to achieve a homogeneous mixture between the doner polymer and acceptor to improve film morphology [12,18]

1.5.4 The Ultimate Performance Parameter PCE

PCE is defined as the ratio of the output power to the input power. A simple device metric that analyzes the performance of the device. The mathematical iteration of PCE is shown in **Equation 1-1**, in which the product of the V_{OC}, J_{SC} and FF is divided by the power input or the incident solar power. [10,16-18]

$$PCE = \frac{V_{\mathrm{OC}} \times J_{\mathrm{SC}} \times FF}{P_{\mathrm{in}}} \qquad \textbf{Eq. 1-1}\ ^{[10]}$$

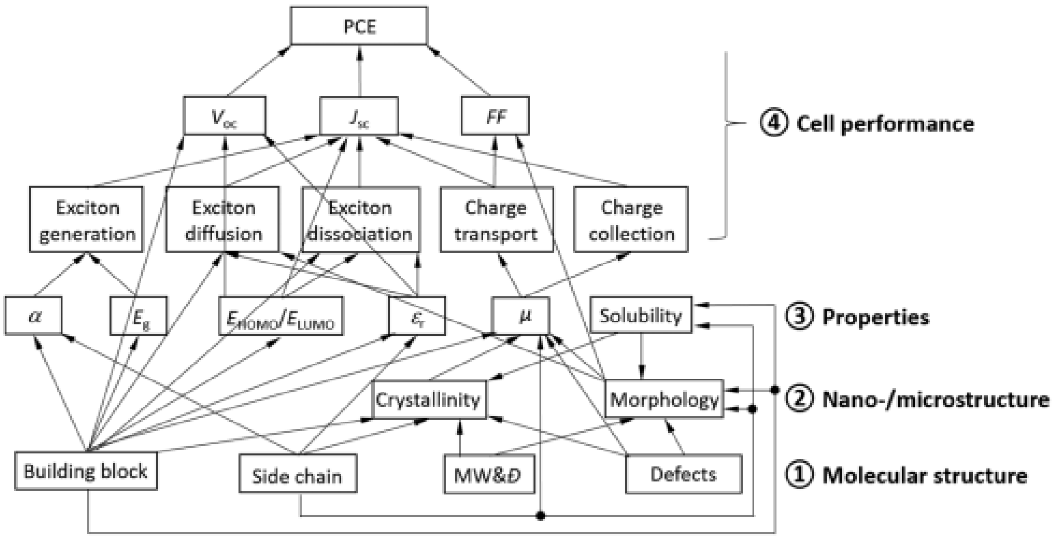

Figure 1-6 The relationship and influencing factors of PCE [11]

If the aforementioned characteristics are known, the J-V curve of an organic cell can be used to obtain the PCE. A straightforward J-V curve shows the voltage along the X axis and the current along the Y axis. The Y intercept is used to determine the J_{SC} value, which is the maximum photocurrent generation value. Since there is no current flowing through the device, the V_{OC}

value is determined from the X intercept. When the voltage and current's product is maximized, a maximum power point occurs between the J_{SC} point and the V_{OC} point. As illustrated in **Figure 1-7**, two squares may be created, and the ratio between them can be computed to get the cell's fill factor.[10,19]

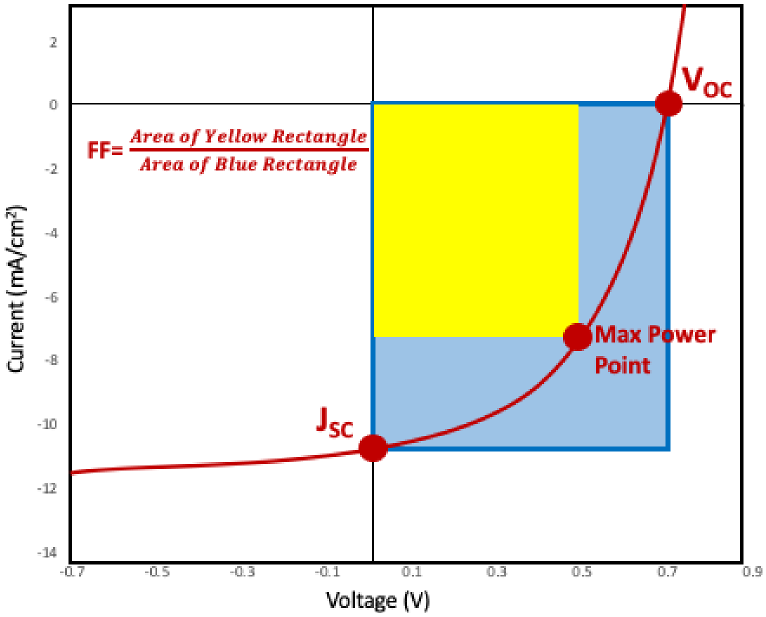

Figure 1-7 Schematic of a Typical J-V Curve for an Organic Solar Cell [19]

1.6 Characterization of Polymer Organic Solar Cells

The following will describe different characterization techniques via optical and chemical metrology used in this thesis.

NMR spectroscopy is a method that is used in the field of chemistry to explore and assess the purity and composition of a sample. NMR stands for nuclear magnetic resonance.[20-22] Both carbon and hydrogen nuclei may be investigated using NMR spectroscopy, with the parameters being adjusted accordingly. After the basic structure of the sample has been identified using NMR, the technique may then be used to investigate a variety of the sample's physical properties, including solubility, diffusion, and phase changes. [20-22] Because each nucleus has a charge, the ability to exchange energy between levels of lower and greater potential may occur when an external magnetic field is introduced. This energy transfer takes place at a wavelength associated with radio frequencies, which are subsequently detected and processed in order to create an NMR spectrum for the nucleus that is being investigated. The resonance frequency of the energy that is being transmitted is determined by the magnetic field that the nucleus has. Electron shielding has the potential to change the magnetic field, although this is very dependent on the surrounding chemical environment. [20-22] The resonant frequency may be used to extract information on the chemical environment of the nucleus since electron shielding is reliant on the chemical environment of the nucleus. A nucleus that has a greater electronegative charge will have a higher resonance frequency. [20-22]

Gel Permeation Chromatography (GPC) has two primary applications: characterizing polymers and separating mixtures into fractions such as polymer, oligomer, monomer, and non-polymeric additives. In our case, GPC is used for characterizing the molecular weight distribution of polymers, a characteristic shared by all synthetic polymers. The most important parameters are number average molecular weight (M_n), weight average molecular weight (Mw), size average molecular weight (Mz) and poly dispersity index which can be found in **Equation 1-2**. This equation models the variation based on size for a polymer. With regards to the working principle of the GPC, it works by pushing the solvent through the instrument via a pump and introducing the test sample into the column through an injection port. The sample is then detected as the components leave the column verified by a software that controls the different parts of the instrument and displays the results on a computer. [23-24]

$$\mathrm{PDI} = M_{\mathrm{w}}/M_{\mathrm{n}} \qquad \textbf{Eq. 1-2}\ [24]$$

Thermogravimetric analysis, also known as TGA is a technique for estimating the sample's mass as a temperature-dependent attribute. Change in mass as a function of temperature is a key feature of many materials as they degrade and lose volatile components. Important information on both physical and chemical events can be extracted such as phase transitions, absorption, adsorption, and desorption, as well as chemisorption, thermal breakdown, and solid-gas interactions (e.g., oxidation or reduction). [25-27]

Different Scanning Calorimetry: Differential Scanning Calorimetry (DSC) is a thermal analysis method that measures the heat flow into or out of a sample as a function of temperature or time while the sample is subjected to a controlled temperature program. It is a very effective method for assessing material attributes such as glass transition temperature, melting, crystallization, specific heat capacity, curing process, purity, oxidation behavior, and thermal stability. The analysis can be done on a wide range of materials including polymers, plastics, composites, laminates, adhesives, food, coatings, medicines, organic materials, rubber, petroleum, chemicals, explosives, and biological samples. [28-29]

Ultra-Violet Spectroscopy: UV-Vis Spectroscopy is a quantitative technique used to determine the extent to which a chemical component absorbs light. This is accomplished by comparing the amount of light that travels through a sample to the amount of light that travels through a reference sample, also known as a blank. This methodology is applicable to a wide variety of sample types, including liquids, solids, thin films, and even glass. For polymers specifically, it is used to detect the chromophores when the matter undergoes $\mathrm{n} \rightarrow \pi^*$ and $\pi \rightarrow \pi^*$ transitions. Furthermore, the extent of conjugation can be detected via UV-Vis. The greater the conjugation, the longer the wavelength of maximum absorption. Another advantage of this form of spectroscopy is the ability to determine the optical bandgap using the onset wavelength from the spectra using **Equation 1-3**. [30-34]

$$E_g(eV) = h \times f = h \times \frac{c}{\lambda_{\text{onset}}} \approx \frac{1240}{\lambda_{\text{onset}}\,(nm)}$$ **Eq. 1-3** [34]

Cyclic Voltammetry or CV is an electrochemical technique that predicts E_{HOMO} and E_{LUMO} through an oxidation and reduction process. This is done by measuring the current at the working electrode (polymer) under the conditions where voltage is in the excess predicted by the Nernst Equation. And thus, by measuring the redox potential, an energy diagram can be extrapolated using **Equation 1-4**. It is important to note that Ferrocene is used as the internal standard, E_{HOMO} = -4.83 eV. [35-36]

$$E_{\text{HOMO}}\ (\text{eV}) = -e(E_{\text{ox}}^{\text{onset}}) - 4.8\text{eV}$$ **Eq. 1-4** [34]

$$E_{\text{LUMO}}\ (\text{eV}) = -e(E_{\text{red}}^{\text{onset}}) - 4.8\text{eV}$$ **Eq. 1-5** [34]

Photoluminescence Spectroscopy is a technique that utilizes light energy or photons to produce the emission of a photon. For D-A organic solar cells, photoluminescence is used in fluorescence to determine the photoluminescence quantum efficiency (PLQE) which is an important parameter to check whether the excitons experience dissociation in the D-A interphase. Mathematically, this number is defined as the number of photons emitted as a fraction of the number of photons absorbed and can be calculated below, where PL_{blend} is the PL intensity of the D-A blend films and PL_{neat} is the PL intensity of neat films. [37-40]

$$PLQE = 1 - \frac{PL_{\text{blend}}}{PL_{\text{neat}}} \qquad \textbf{Eq. 1-6}$$

X-ray diffraction (XRD) is a technique used for polymers primarily for the determination of their degree of crystallinity. Other main features of XRD analysis include indexing of crystal structures, microstructure, and orientation. For this thesis, the degree of crystallinity and orientation of the polymer is concerned. To obtain XRD peaks, constructive interference between monochromatic X-rays and a crystalline sample are produced. A cathode-ray tube produces the X-rays, which are then filtered to create monochromatic radiation, and aimed onto the sample. When Bragg's Law (**Equation 1-7**) is satisfied, constructive interference (and a diffracted ray) results from the interaction of incoming rays with the sample. The wavelength of electromagnetic radiation is related to the diffraction angle and lattice spacing in a crystalline sample. The detected, processed, and counted diffracted X-rays are then analyzed.

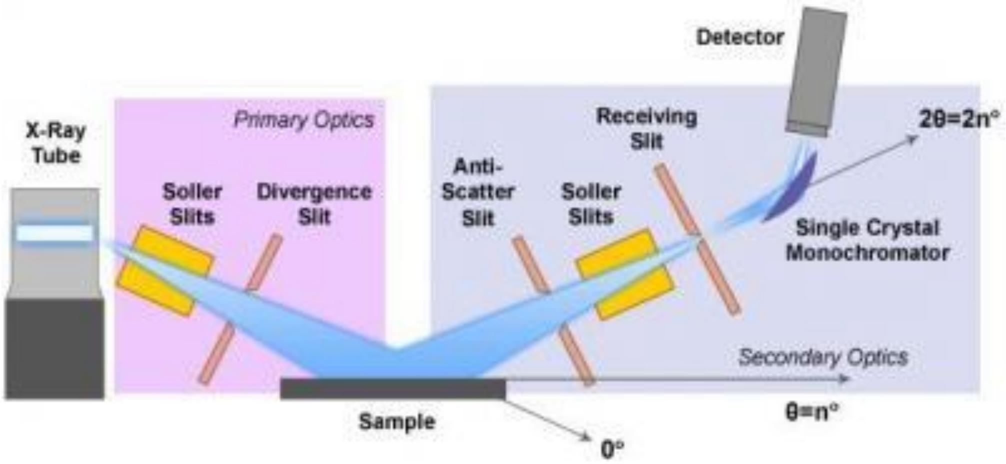

Figure 1-8 Operating Principle of an XRD between a monochromatic x-ray and sample [41]

$$n\lambda = 2d\sin\ \theta \qquad \textbf{Eq. 1-7}$$ [34]

Atomic Force Microscopy: AFM is a qualitative technique for surface analysis that involves topography imaging. It uses a probe to detect morphological features on the nanometer to micron-scale such as film roughness, phase segregation and domain size. To do the surface analysis, a cantilever is used to scan over the sample surface in which attractive force between the surface and the tip causes the cantilever to deflect towards the surface. When the raised and lowered cantilever influences the deflection, it results in a topographic image. [43]

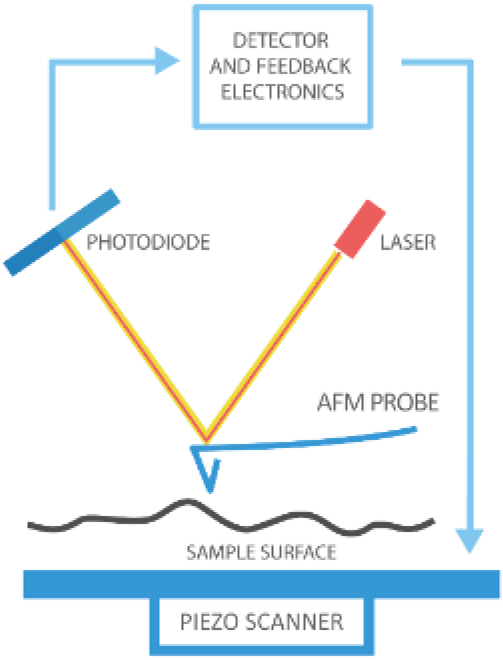

Figure 1-9 Operating Principle of an AFM [44]

Chapter 1 Part II:
Introduction to Organic Thin Film Transistors

This section of the thesis will address another type of application that proves useful towards electronical components which are organic field-effect transistors (OFETs). OFETs are a type of field-effect transistor that has a channel made out of an organic semiconductor which can be manufactured by vacuum evaporation of small molecules, solution-casting of polymers or small molecules, or the mechanical transfer of a single-crystalline organic layer onto a substrate. [45] They have already shown a great promise for light-weighted, portable and flexible device applications such as smart cards, OLEDs, pixel drivers, etc. [46] Their most attractive commodity is the utilization of efficient techniques such as printing, coating, and evaporation to generate organic electronic materials and their ability to be fabricated on flexible surfaces. Polymers with excellent solubility may be used to deposit thin-film organic layers on large-area substrates by inkjet printing, spin-coating, screen printing, etc.[46-49]

The very first thin film transistor was invented by John Bardeen, Willliam Shockley, and Walter Brittain in 1947 and ever since have been dominant in the microelectronics industry. [50] They utilized inorganic material that had a complicated fabrication process such as involving high temperatures, high vacuum deposition processes and sophisticated photolithographic patterning. [50] And thus, the introduction of OTFTs made it more convenient in the fabrication process which involves a low-temperature deposition process and solution processing. [50] The other main advantage is their mechanical flexibility allowing them to be paired up with plastic substrates for lightweight and foldable products. [50]

1.7 Design and Operation of an OFET

In terms of design and function, an OTFT is similar to its inorganic equivalent. It is a three-terminal device in which a voltage given to the gate electrode regulates the flow of current between the source and drain electrodes when a bias is applied. A FETs' ability to adjust the source-drain current through a third terminal has led to their widespread usage as switches. [46-50] In terms of their performance, they are evaluated based on mobility μ, which denotes the ease with which charge carriers may flow across the active layer under the influence of an electric field. [46-50] This value is determined by current-voltage measurements and should be as large as possible. Typical values for amorphous silicon devices range between 0.1 and 10 $cm^2V^{-1}s^{-1}$ with the best organic materials achieving mobilities between 1-10 $cm^2V^{-1}s^{-1}$. The current on/off ratio, which is defined as the ratio of the current in the "on" and "off" states, is the switching performance of OTFTs.[46 -50]

1.7.1 Types of OTFT Designs

The term OTFT can be used in a generic sense to refer to most of the different types of organic transistors. [49] However, organic transistors are typically categorized into one of several categories (depending on the mechanism used to achieve the current modulation. [49] Among these categories include, but are not limited to the following:

Table 1-1 Categorization of OTFTs [49]

Application Type	Description
Organic Field Effect Transistors (OFETs):	OFETS (organic field effect-transistors), like conventional MOSFET (metal-oxide-semiconductor field effect transistor) or TFT (thin film transistor) devices, have a gate electrode and a semiconductor layer separated by a dielectric layer. An electric field is created across the dielectric layer. As a result, this electric field may control the size and shape of a high-conductivity zone and change the flow of current through the semiconductor material (I_D).
Organic Electrochemical Transistors (OECTs)	When a voltage is applied to the gate electrode, organic electrochemical transistors (OECTs) may cause either an increase or decrease in I_D, depending on the kind of reaction being induced. The source, drain, and gate electrodes serve as the working, counter,

	and reference electrodes in standard three-terminal electrochemical cells. Some other types of OECTs are more like a standard OFET in which some electrochemical reaction is taking place at an interface of the semiconductor to modulate the current. There are several sub-categories of OECTs
Electrolyte-gated organic field effect transistors (EGOFETs)	A layer of electrolyte (either solid or liquid) is used in EGOFETs to keep the gate electrode apart from the semiconductor. There is an ionic mobility in this electrolyte layer that leads to charge accumulation at its interfaces and subsequent electrochemical reactions. Low operating voltage is a benefit of the EGOFET, but poor switching rates are a drawback because of their dependence on electrochemical activity. Several newly developed EGOFETs with membranes that are ion-selective have also been shown to be useful in sensing applications.

1.7.2 Working Principle of OTFTs

To understand how OTFTs work, the principle of conductivity must be recognized. For conductive materials, electrons move from the valence band to the conduction band. While for semiconductors, the movement of electrons from the valence band to the conduction band is difficult because of the band gap being too wide. [49-53] And thus, for polymer semi-conductors, the enhancement of conductivity is done via doping by either oxidation (p-type doping) or reduction (n-type doping) by chemical methods. Moreover, by combining p-type and n-type materials, a p-n junction might be created at the interface between the two materials. [53-56] Near their interface, negative charges from n-type material diffuse into the p-type area, while positive charges from p-type material diffuse in the other direction. The opposite charges and travelled charges from the other side create a "space charge area" (also known as depletion region). [53-56] This interaction is typically used in the fabrication of diodes and transistors. In OTFTs, charge injection is used to bend the energy level of the semiconductor and enable charge transport. Unlike metal-oxide semiconductor field-effect transistors (MOSFETs), an OTFT requires the accumulation of injected charge carriers to create current flow. [53-56] Holes are injected from the source contact of a p-type semiconductor by applying a negative V_{DS}. Under a negative bias, holes collect in the electric field of the active channel layer, with the HOMO level of the organic semiconductor subsequently bending upwards toward the Fermi level. Polarons hopping across the conjugated structure inside the OSC start to localize the delocalized state, as a result of these injected holes. [53-56] Consequently, the active channel acquires a positive charge. Similar phenomena occur with n-type semiconductors, with the exception that electrons are injected from a positive V_{DS} source, with the LUMO level of the OSC subsequently bending downwards. To accomplish charge transport in OTFTs, the driving forces V_{DS} and V_{GS} are necessary to create current. By raising V_{DS}, potential accumulates from the source to drain throughout the channel. With sufficient gate bias, charges might flow from the source to the drain. [53-56]

The design of an OTFT utilizes 4 types of structures a) bottom-gate, top-contact (BGTC), b) bottom-gate, bottom-contact (BGBC), c) top-gate, top-contact (TGTC), d) top-gate, bottom-contact (TGBC). [49-57] They all utilize an insulating substrate, a dielectric layer, a semiconducting layer and a gate, source and drain for contacts. [49-57] The injection and extraction of charge carriers is done by source and drain electrodes, respectively, which are in contact with the active layer.

On the contrary, an insulator that controls the conductivity of the channel separates the gate from the semiconductor film. For the interest of gas sensors, a bottom gate structure is desired because the organic semiconductor is exposed to the target analytes directly.[49] Structures that utilize top gate structures are usually for circuit fabrication such as amplifiers and switches.[49] As mentioned before the injection and extraction for charge carriers are by source and drains whereas the gate is separated from the semiconductor through a dielectric film. The semiconducting channel is determined by two parameters, width and length. [49]

There are three operating modes for field-effect transistors: i) gate to source voltage with respect to threshold voltage, ii) drain to source voltage with respect to the over drive voltage and iii) p-type or n-type mode. The p-type mode is when all the holes are the charge carriers and in n-type mode is when all the electrons are the charge carriers. Materials that possess both n-type and p-type modes are said to be ambipolar.

The first operation mode known as the cut off is defined by $V_{GS} > V_T$ as shown in **Figure 1-12 (b)**. The applied V_{GS} cannot form a conducting path between the source and drain and thus the drain to source current (I_D) is zero due to the depletion of holes in the channel. [57] When the V_{GS} is shifted lower than V_T, the holes are then accumulated at the dielectric/semiconductor interface. implicating a uniform charge distribution along the channel $|V_{\mathrm{DS}}| \ll |V_{\mathrm{OV}}|$ as shown in **Figure 1-12 (c)**. During these biasing conditions, I_D will be different from the zero and linearly dependent on V_{DS} according to this equation: [57]

$$I_D = \mu C_i (W/L)(V_{GS} - V_T)V_{DS}$$ **Eq. 1-8** [57]

where $C_i = \varepsilon_i / x_i$ is the gate capacitance density and ε_i gate electric permittivity.[57] Moreover, this operation mode is also said to behave as a voltage-controlled current source equal to $g_m V_{\mathrm{GS}}$. [57].The g_m refers to the transconductance which is related to the change in output of I_D to an input of V_{GS} change with constant V_D bias

$$g_m = \frac{\partial I_D}{\partial V_{\mathrm{GS}}} = \mu C_i (W/L) V_{DS}$$ **Eq. 1-9** [57]

When V_{DS} is approaching V_{OV}, it means that the charge carrier concentration is not uniform anymore and thus V_{GD} is less negative then V_{GS}. This also affects the charge accumulation around the drain as it becomes lower than at the source. According to the mathematical equation I_D changes from a linear to a parabolic dependence on V_{DS}.

$$I_D = \mu C_i (W/L) V_{DS}[(V_{GS} - V_T) - V_{DS}/2]$$

Eq. 1-10 [57]

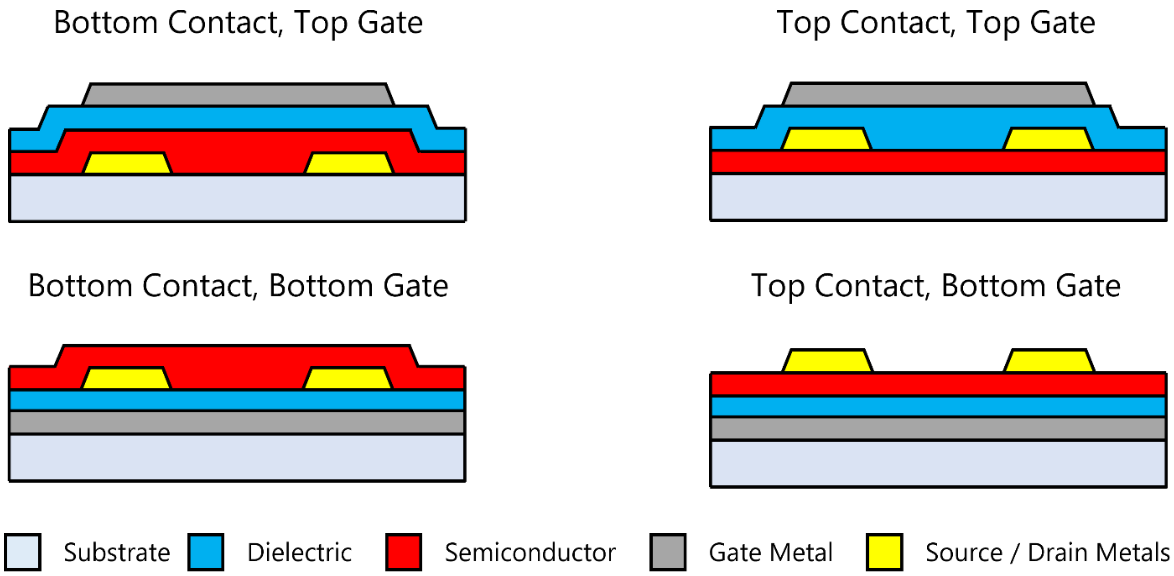

Figure 1-10 Cross sectional schematic of OTFT configurations [58]

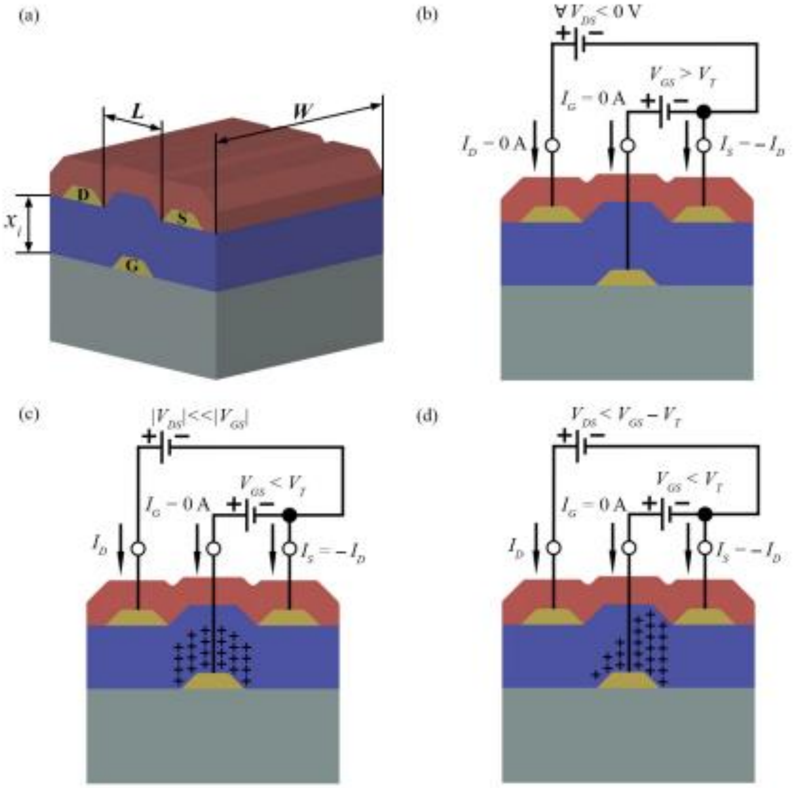

Figure 1-11 P-type field effect transistor **(a)** structural schematic and device electrodes **(b)** cut-off **(c)** triode **(d)** saturation operating modes [57]

1.7.3 Understanding OTFT Parameters

To gain a deeper understanding of the parameters we can describe the parameters using mathematical relationships.

Charge Carrier Mobility:

The charge carrier mobility can be described by μ as the average charge carrier drift velocity per unit of electric field along the channel

$$\mu = v_{\text{drift}} / E_{DS} \qquad \textbf{Eq. 1-11}\ [57]$$

It is a measure of efficiency of the charge carriers moving along the conducting channel. And can be directly related to the conducting channel g_m, which is the slope of the I_D versus V_{GS}. It should also be noted that the μ is related to the slope of I_D versus V_{DS} and is usually not considered as a constant which is why a linear fit of the I_D versus V_{DS} is used to extract the average mobility value. Furthermore, the mobility is dependent on the overdrive voltage by a factor (gamma).

$$\mu_{lin} = \frac{g_m}{C_i(W/L)(V_{DS})} \qquad \textbf{Eq. 1-12}\ [57]$$

$$\mu(V_{GS}) = k(V_{GS} - V_T)^{\gamma} \qquad \textbf{Eq. 1-13}\ [57]$$

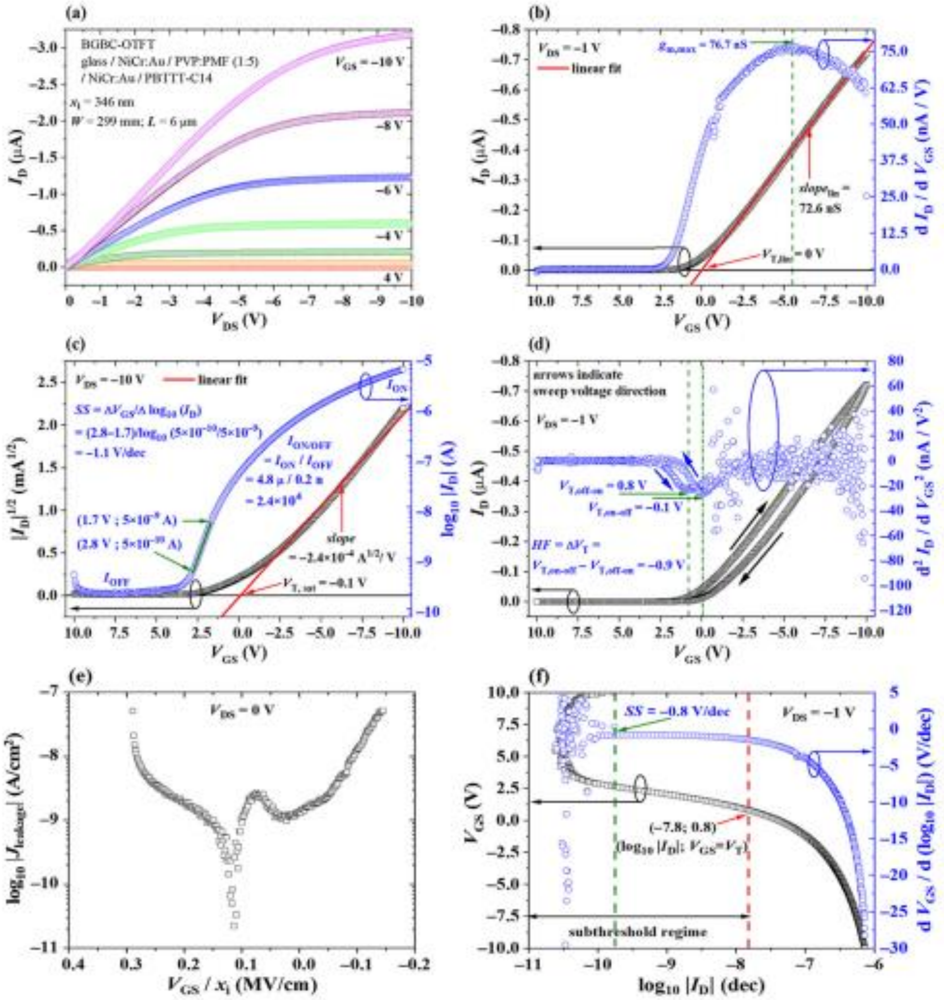

Figure 1-12 (a) I_D vs V_{DS} for V_{GS} from 4 to −10 V. (**b)** I_D vs V_{GS} for V_{DS}=−1 V (**c)** I_D vs V_{GS} for V_{DS}=−10 V to illustrate the linear fit for µ and V_T calculation in saturation. (**d)** I_D versus V_{GS} scans for V_{DS}=−1 V featuring hysteresis. (**e**) $J_{leakage}$ vs the perpendicular electric field in the channel (V_{GS}/x_i) for V_{DS}=0 V. (f) V_{GS} versus $\log_{10}|I_D|$ and its first derivative to illustrate SS calculation. [57]

The k refers to the constant mobility value whereas γ is a parameter that is lower than one and is dependent on the conduction mechanism of the device, doping density and dielectric permittivity of the active material. The grain's size and the inter-grain defects can also influence the k value as it depends on the surface formation of the semiconductor. For thinner dielectrics, a lower current and larger mobility is preferred because of the larger switching speeds in digital circuits but it does not necessarily mean a fast-sensing response and better sensitivity.

The slope of the current versus the voltage curve turns zero when the V_{DS} approaches the V_{OV} which means the OTFT device is in saturation. This is also familiar to when the V_{GS} approaches V_T. Because the channel is close to the drain contact, the slope cannot be taken as it is depleted of carriers. However, an estimation can be obtained by using the following equation.

$$\mu_{sat} = \frac{2}{C_i(W/L)}\left(\frac{\partial\sqrt{I_D}}{\partial V_{GS}}\right)^2 \qquad \textbf{Eq. 1-14}\ [57]$$

To extract the mobility, a voltage scan is necessary. Usually, in a BGBC TFT, the charge injection barriers and high disorder in the semiconductor film can degrade the slope.

Threshold voltage:

Threshold voltage refers to when V_T is the minimum gate to source voltage required for accumulating charge carriers at the semiconductor/dielectric interface and forming a conducting path between the source and the drain electrode. [57] Generally, V_T is preferred to be desired as close to zero which translates into a low operating voltage, and thus low power consumption for portable devices. To increase gate capacitance, it is recommended to decrease the thickness of the dielectric film or increase the dielectric constant.

Figure 1-12 (d) illustrates the hysteresis effect that is quantified into the shift of the threshold voltage. It is not desirable for a shift in the transistor characteristics depending on the voltage scanning parameters and thus pertains to bias stress. A shift in V_T is an important parameter because it can influence the gas sensor’s response. And thus, charge trapping must be reduced to get a better sensor response. To help improve the bias stress, the semiconductor/dielectric interface should be improved by surface treatments. Another way to minimize the bias stress is to bias the sensor device at low voltages, for shorter times and at less frequency. The hysteresis effect can be determined below.

$$HF = \Delta V_T \qquad \textbf{Eq. 1-15}\ ^{[57]}$$

Current On/Off Ratio:

The on/off ratio refers to the ratio of the current accumulation and depletion. The off current depends upon the channel conductivity σ_s and dimensions. The equation below demonstrates that phenomenon.[57]

$$I_{OFF} = \sigma_s x_s \frac{W}{L} V_{DS} \qquad \textbf{Eq. 1-16}\ ^{[57]}$$

To demonstrate the on/off ratio for a device from cut-off to saturation the following equation can be used:

$$I_{ON/OFF} = \frac{\mu C_i (V_{GS} - V_T)^2}{\sigma_s x_s V_{DS}} \qquad \textbf{Eq. 1-17}\ ^{[57]}$$

It is quite evident that a high dielectric constant and a thinner dielectric film are needed to increase C_i. However, this can negatively affect the I_{OFF} due to an increase of leakage current density from the gate electrode as shown in **Figure 1-12 (e).** Although a higher on/off ratio is desired for applications such as display monitors, it is not needed for sensors.

Subthreshold Slope:

The variation in the gate biasing to result in one decade change in the drain current refers to the subthreshold slope. It is demonstrated by a logarithmic scale where I_D is the y axis and V_{GS} is the x-axis. For OTFTs, the subthreshold slope is similar to mobility enhancement for carrier hopping and thus a lower trap density is needed to achieve steeper slopes. It can sometimes be used as a sensitivity parameter but that is quite rare. The lower the subthreshold value, the less bias stress is resulted. For gas sensors specifically, the interaction between the gas molecules and trap sites are monitored through mobility and threshold voltage shifts.

1.7.4 Evaluation of OTFT devices

The OTFT devices will be tested using an Agilent B2912A Precision Source/Measure Unit probe station. The three probes are manually guided by hand to their respective contacts (source, drain and gate) with the aid of an optical microscope. After the probes are successfully contacted, a program will run a series of sweeps drains and drain voltage while simultaneously measuring the current through the source and drain.

For an ideal case, the output curve is generated through **Equation 1-18** for the linear region and **Equation 1-19** for the saturation region where I_D is the drain current, W and L are the channel width and length, Ci is the capacitance per area of the dielectric (~11.6 nF cm^{-2} for SiO_2), V_G is the gate voltage and V_T is the threshold voltage. At low drain voltages, a linear region can be seen but at higher drain voltages the saturation region occurs.

To obtain the threshold voltage and the charge carrier mobility of a polymer, a transfer curve is plotted as drain current vs gate voltage current. For any p-type or n-type device, the mobility is obtained through the slope, and the threshold voltage is obtained through the extrapolation of the slope to the x-axis intercept. The current on/off ratio is calculated by dividing the drain current at saturation for a given gate voltage by the drain current when no gate voltage is applied

$$I_D = \mu C_i \frac{W}{L}\left((V_G - V_T) - \frac{V_D}{2}\right)V_D \qquad \textbf{Eq. 1-18}$$

$$I_D = \mu C_i \frac{W}{2L}(V_G - V_T)^2 \qquad \textbf{Eq. 1-19}$$

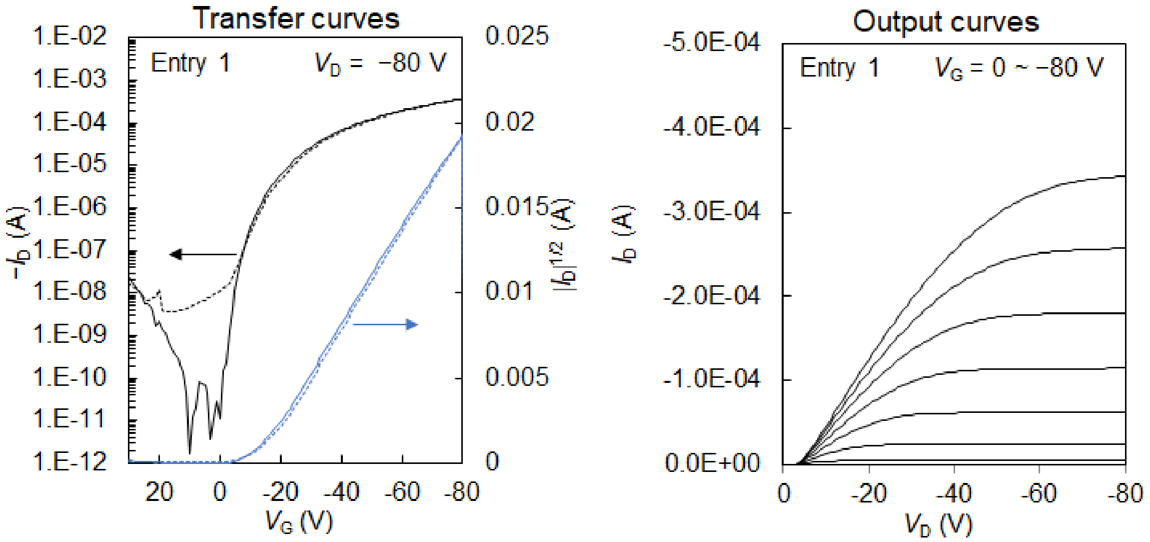

Figure 1-13 Ideal transfer and output curves of a typical p-type OTFT device [59]

Chapter 1: Part III
Objective and Structure of Thesis

Two different applications will be explored in this thesis with the aim to improve performance. The first application addresses organic solar cell that utilizes renewable solar energy as a way to combat global emissions and conserve natural resources. While the second application addresses organic field effect transistors to be useful for sensors.

With regards to the second chapter of this thesis, a novel polymer donor PTEI is synthesized to be used as the active layer in organic solar cell. Its simple synthetic complexity, low-lying orbital energy level, strong absorption in the visible region and good solubility after alkylation make it a great candidate for solar cell applications. For this polymer, we are studying a novel C24 carbamate chain to replace the C20 alkyl chain to study the impact on the overall PCE by tuning the acceptor polymer component. Based on our previous findings about the carbamate chain, it can be thermally cleaved by thermal evaporation. This could potentially improve the coplanarity of the TEI structure thus increasing the mobility resulting in a higher V_{OC}, and increasing π-π stacking for better morphological stability and higher FF. The polymer will be characterized by using TGA, GPC, UV-vis, and CV to study the thermal, optical, and electrochemical properties. Based on the DFT simulation alone, PTEI exhibited a deeper HOMO level than alkyl substituted PTEI meaning that the V_{OC} can be improved further. Moreover, PTEI will be blended with Y6 small molecular acceptor and used in an inverted OSC structure to study its photovoltaic performance. SCLC, XRD and AFM will be used to further investigate the mobility and film morphology.

The third chapter focuses on three novel isoindigo polymers, PIDMT, PIDBT and PIDBDT for their use in OFETs. Isoindigo is known for being an excellent acceptor building block for donor-acceptor polymers with advantages of simple synthesis, excellent air stability and high electrical performance. This chapter explores the impact of the thermo-cleavable carbamate chain for the potential enhancement of mobility, solvent resistance, and morphological stability. Although alkyl substituents can improve solubility, it reduces the charge carrier mobility by hindering the π-π stacking by acting as an insulator. Thus, by substituting a thermally removable side chain on the isoindigo unit, the π-π stacking would be more profound, helping form intermolecular hydrogen bonds, to afford excellent solvent resistance and morphological stability as well as enhancing the mobility of isoindigo.

The fourth chapter will summarize all the findings along with some future improvements for the photovoltaic properties and performance.

Chapter 2: TEI-BDT Based Organic Solar Cell

2.1 Introduction

For organic photovoltaic applications, it has been known that isoindigo based polymers exhibit excellent optoelectronic characteristics with excellent flexibility and long-term stability. Isoindigo derives from the structural isomer, indigo, which is a common naturally occurring pigment made by a specific plant, isatis tinctoria. [60-62] The very first isoindigo D-A photovoltaic performance was reported by Zhang et al, Liu et al. and Wang et al, in 2011 with PCEs ranging from 1 to 3%. It was soon after Wang et al, developed a bulk heterojunction solar cell with $PC_{71}BM$ as the acceptor to give a PCE of 6.3 %. [60-62] It was until then that the scientific community realized that this electron deficient building block is a good candidate for organic solar cells. Since then, isoindigo materials were categorized into 5 types, standard, halogenated, heterocycle-substituted, peripherally expanded, and core-expanded. An important characteristic of the isoindigo material is the nitrogen atom on the lactam ring, as this position allows for further tunability of the monomer. [63-66] This could include improving the solubility of the material with an alkyl chain or extending the pi-pi conjugation of the structure. Furthermore, other materials that utilize halogen atoms such as chlorine or fluorine are used to lower the optical bandgap to further increase the charge carrier mobility. [63-66] An improved carrier mobility means that the interchain packing of the polymer leads to an increase in crystallinity, thus ultimately improving the charge transport.

Their structure consists of a benzene ring and are connected via an exocyclic double bond at the 3 and 3’ positions. [63-66] The core expanded isoindigo that were previously been studied for treating neuro-degenerative diseases has been utilized for solar cell application by incorporating bis(oxindole) as the core expansion. [67] This created an electron-deficient building block for donor/acceptor, wide bandgap conjugated polymer. [67] The features of this polymer also include simple synthetic complexity with high yield, a low-lying orbital energy level, strong absorption in the visible region and good solubility after alkylation. [68] According to Jian et al [67], the inverted bulk heterojunction polymer solar cell PTEI-T (shown in **Figure 2-1**) exhibited a high PCE of 7.32 %, J_{SC} value of 13.4 $mAcm^{-2}$, a fill factor of 0.65 and an open circuit voltage of 0.85 V when pairing with $PC_{61}BM$ as the acceptor [67].

After the introduction of non-fullerene acceptors, H. Li et al, synthesized the same monomer TEI with n-alkylation and polymerized it with halogen-substituted benzodithiophene (BDT) to produce three copolymer donors (PTEI-H, PTEI-F and PTEI-Cl) shown in **Figure 2-1 (a)**. It was concluded that PTEI-H exhibited the best performance of 8.27 % PCE with a V_{OC} of 0.75 V, J_{SC} of 21.90 $mAcm^{-2}$ and a FF of 50.1 %.[68] Meanwhile, PTEI-F and PTEI-Cl exhibited 7.22 % and 6.50% due to their low short-circuit density and poor fill factor. The reasons for their low J_{SC} and FF is attributed to their unstable charge transfer, deficient photo-induced charge transfer and increased trap-assisted recombination. [68] All in all, H. Li et al took the same PTEI monomer and enhanced the overall photovoltaic performance by 0.95% through fine tuning the small molecule acceptor and introducing BDT halogenated donor variants.

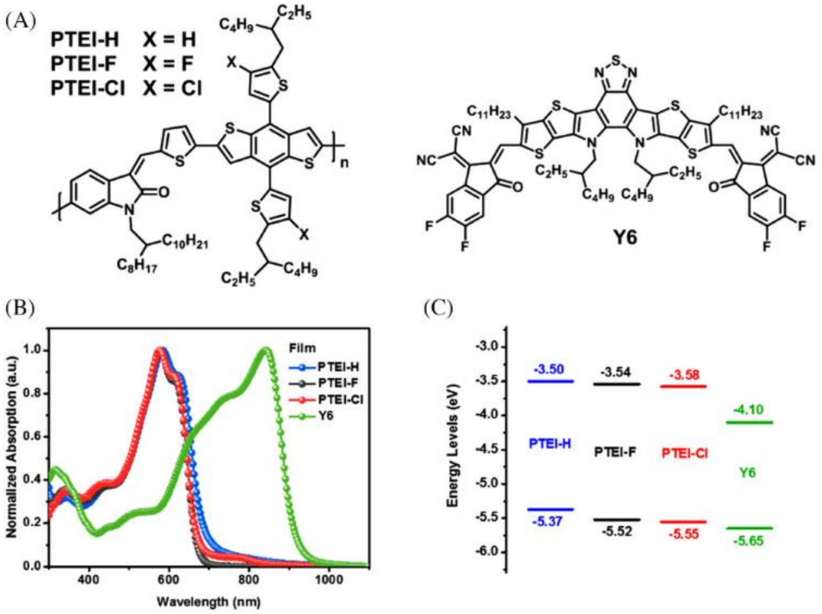

Figure 2-1 (a) Molecular structure of TEIBDT alkyl substituted polymer with Y6 **(b)** UV-vis absorption spectra **(c)** Energy level diagrams [68]

Based on these findings, adjusting the donor component of the TEI polymer can have a substantial impact on power conversion efficiency. Despite the aforementioned findings, tuning the acceptor component of the polymer might prove to be a fascinating endeavor and is scarcely reported for amine-based donor-acceptor polymers. To be more specific, the n-alkylation group, which works to increase solubility can be further tuned to study the effect on PCE. In this thesis, we have chosen a novel C24 carbamate chain to replace the C20 alkyl chain to study the impact on the overall PCE by tuning the acceptor polymer component. Based on our previous findings about the carbamate chain by Ngai et al, [77] it can be thermally cleaved under mild conditions. This could potentially improve the coplanarity of the TEI structure thus increasing the mobility resulting in a higher V_{OC}, and increasing π-π stacking for better morphological stability and higher FF. Thus, ultimately increasing overall PCE.

2.2 Polymer Structure and Design

2.2.1 Computational Study of Polymer Structure

To evaluate the effects of the electron donating carbamate group on the TEI unit, a density functional theory simulation was performed. The electron distribution and E_{HOMO}/E_{LUMO} are calculated and compared for both alkyl and carbamate TEI structures in a vacuum environment. It is necessary to evaluate the structure to determine the degree of coplanarity so it could be viable for photovoltaic solar cells. As mentioned before, a coplanar and rigid backbone is necessary to achieve a high charge carrier mobility which is achieved through strengthening the intermolecular interactions through side chain engineering. In this section, we study a novel hemi-isoindigo unit comprised of a thiophene spacer unit between the indigo moiety and benzodithiophene donor unit with a long decyl-tetradecyl chloroformate chain substituted on the indigo nitrogen atom. It is theorized that the carbamate chain will give good coplanarity and rigidity compared to the n-alkyl chain due to increased intermolecular interactions.

The simulations are calculated under quantum mechanical iteration techniques provided in Avogadro 1.2.0, Gaussian 09, and Gaussian 16 software. Using the Merck molecular force field (MMFF94s) approach in Avogadro 1.2.0, a low-level energy minimization of the model compounds was done. Then, higher level geometry optimization and energy minimization of the model compounds were performed using Gaussian 16 with the B3LYP level of theory and the 6-31G(d) basis set under tight convergence to investigate the optimized geometry and molecular orbital (MO) energy levels, respectively. It should be noted that a methyl group was replaced instead of the long decyl-tetradecyl chain to avoid computational complexity and time.

(a)

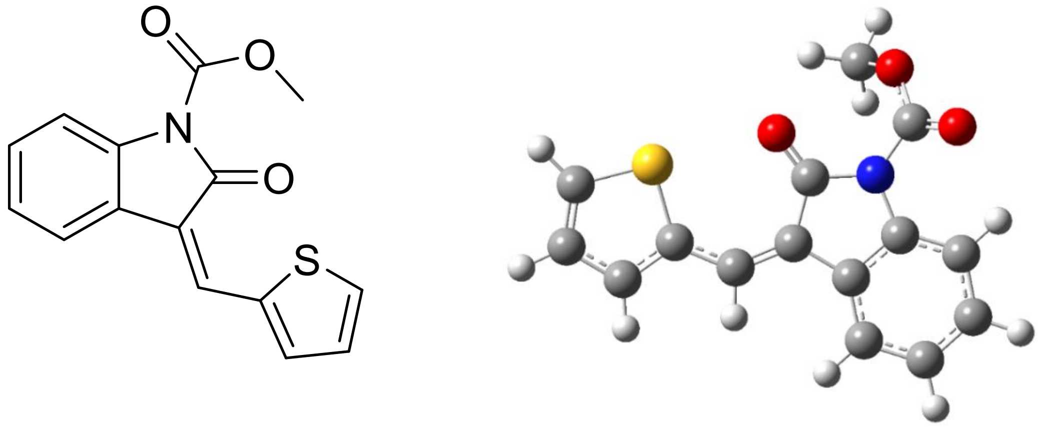

(b)

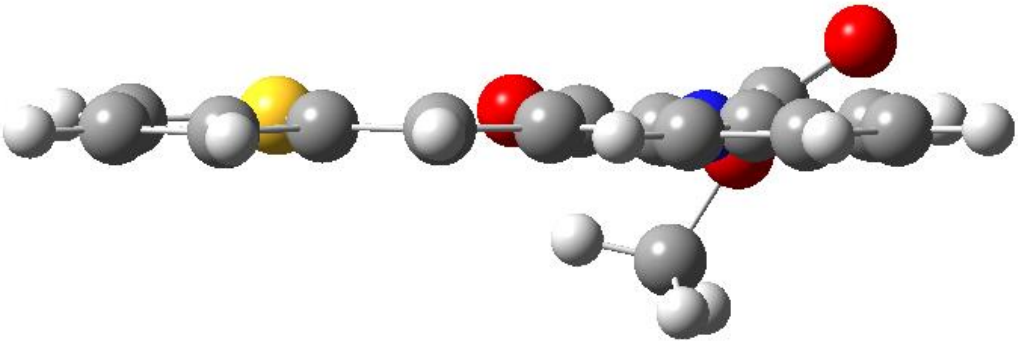

(c)

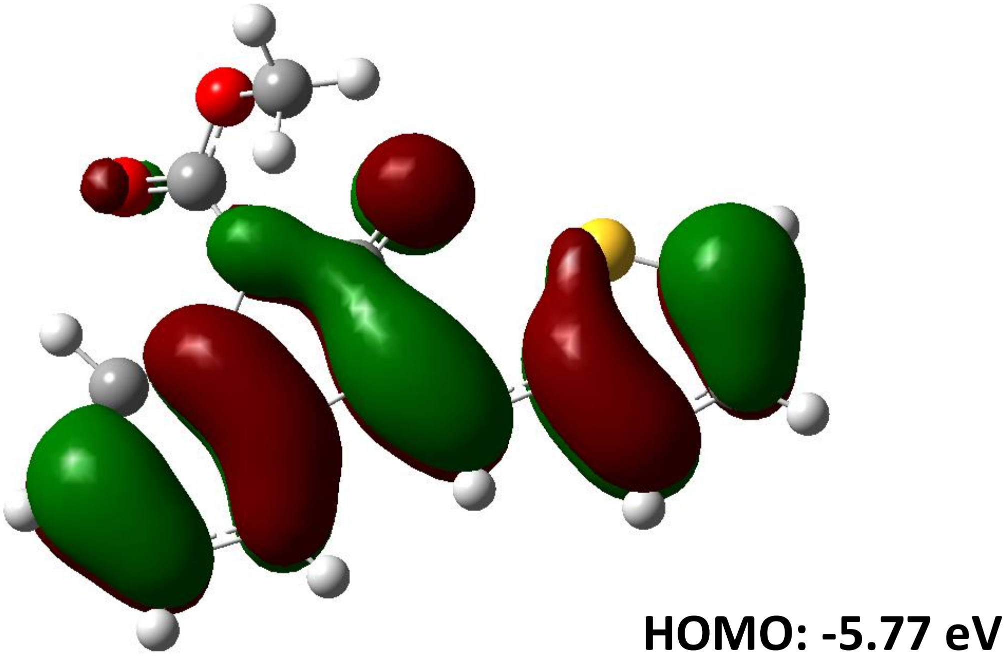

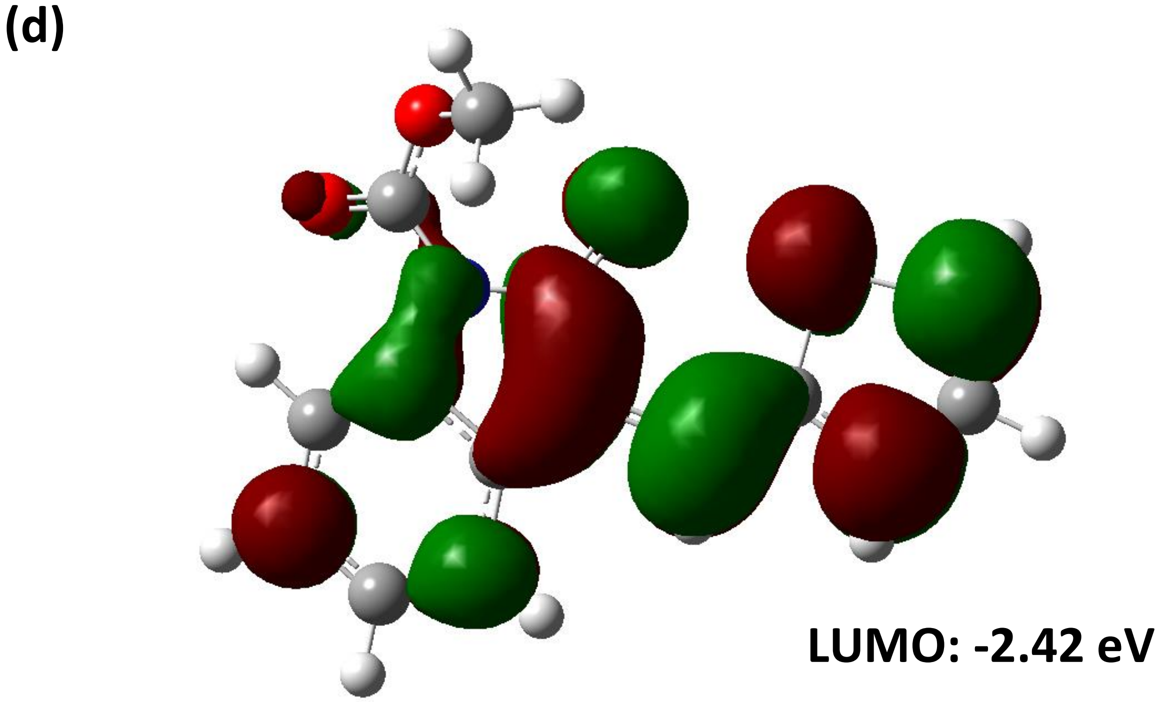

Figure 2-2 (a)/(b) Geometry of TEI optimized by DFT simulation **(c)** HOMO/(**d**) LUMO orbitals of TEI with energy level respect vacuum (0 eV)

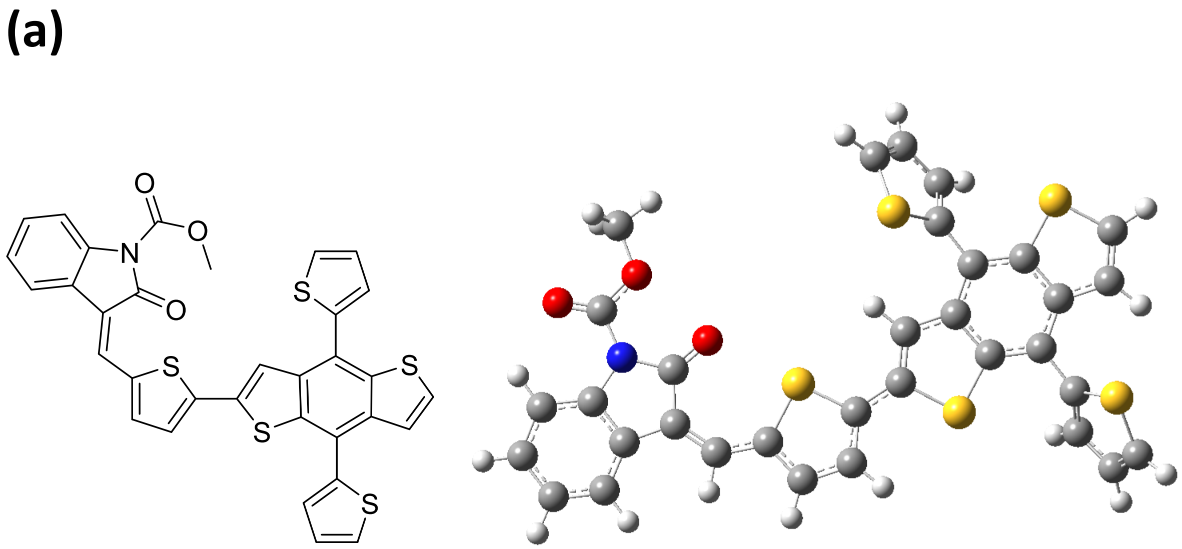

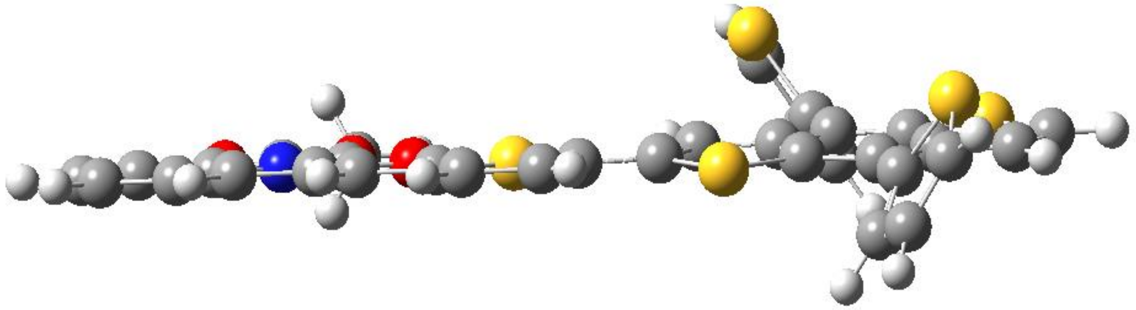

(b)

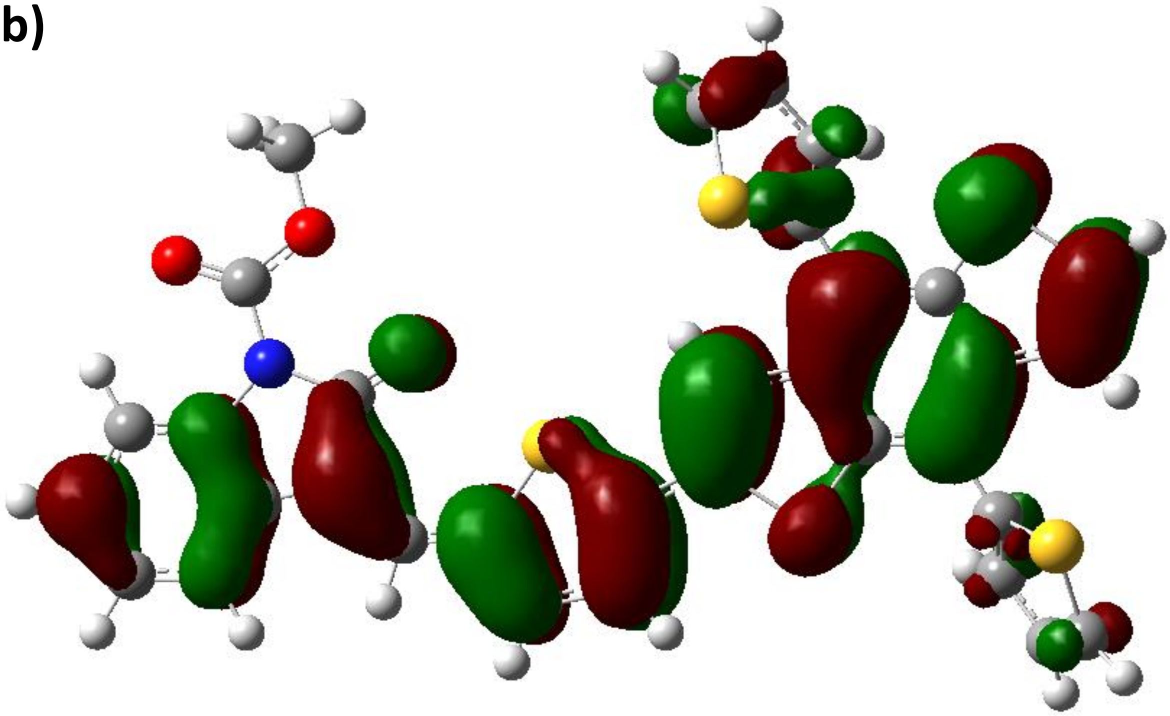

HOMO: -5.26 eV

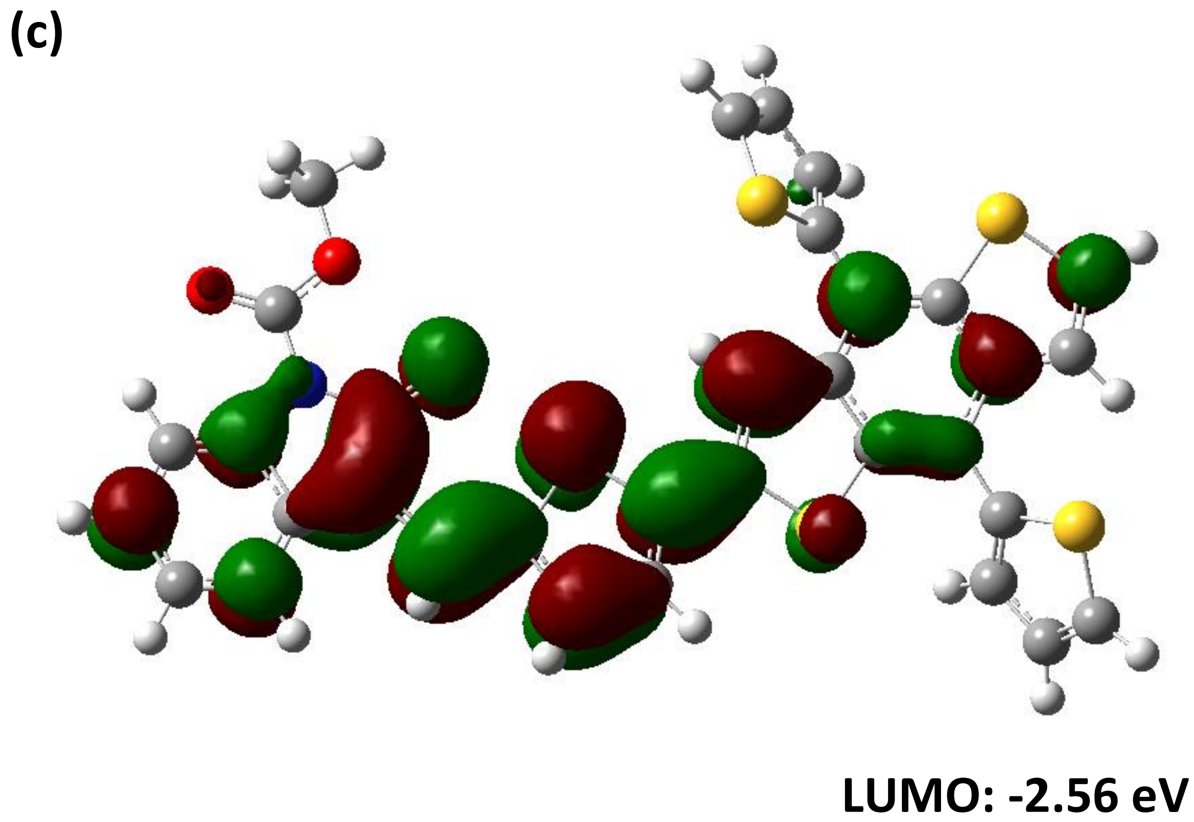

Figure 2-3 (a) Geometry of TEIBDT with carbamate chain optimized by DFT simulation **(b)** HOMO/**(c)** LUMO orbitals of PTEI with energy level respect vacuum (0 eV)

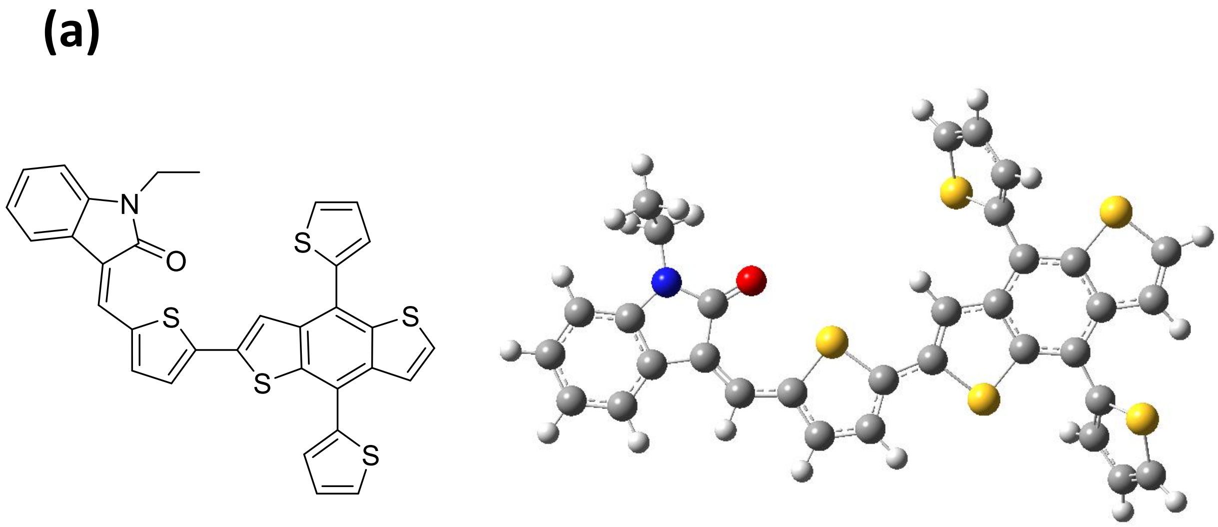

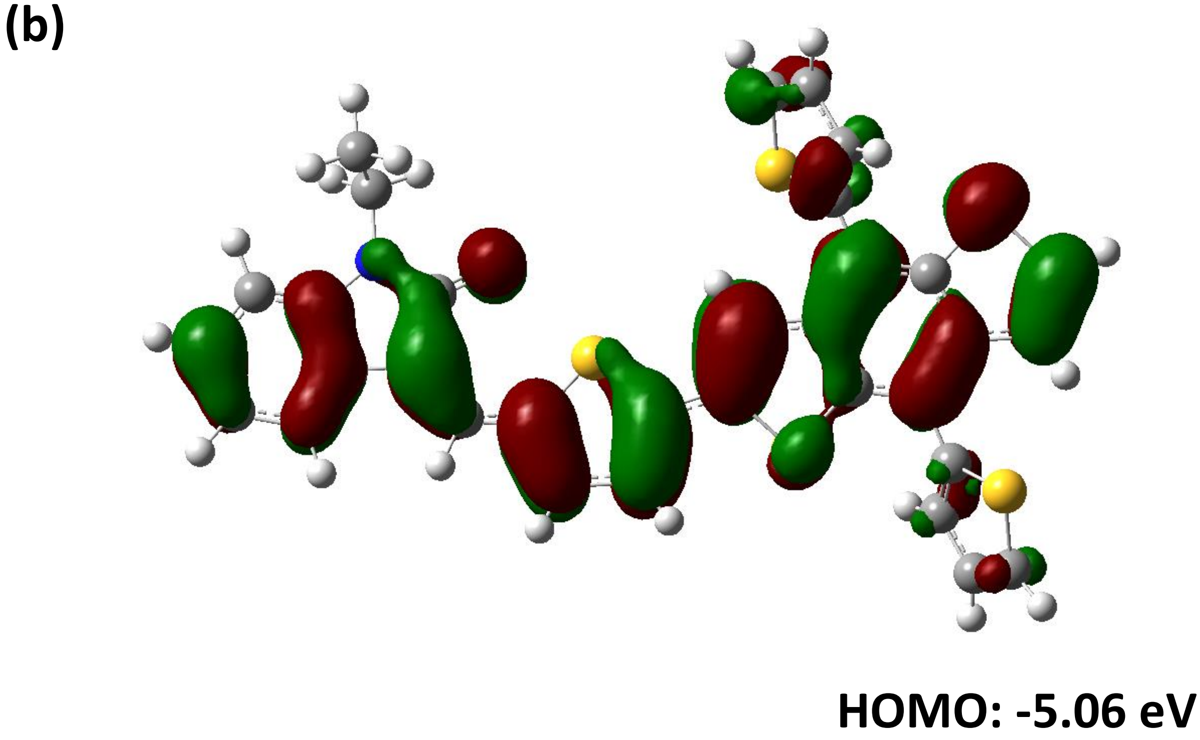

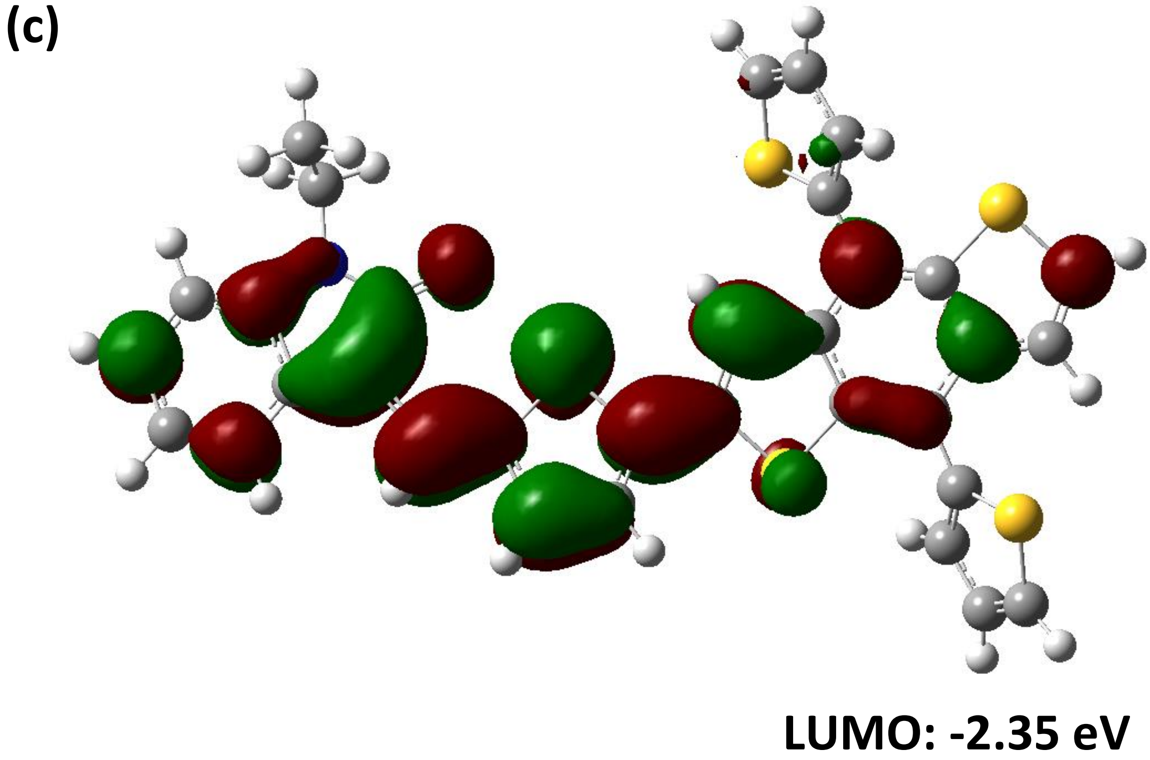

Figure 2-4 (a) Geometry of TEIBDT with alkyl chain optimized by DFT simulation **(b)** HOMO/ **(c)** LUMO orbitals of PTEI with energy level respect to vacuum (0 eV)

Table 2-1 E_{HOMO}/E_{LUMO} energy levels based on DFT

	DFT E_{HOMO} (eV)	DFT E_{LUMO} (eV)	E_g (eV)
TEI	**-5.77**	**-2.42**	**3.35**
TEIBDT (Carbamate)	**-5.26**	**-2.56**	**2.70**
TEIBDT (Alkyl)	**-5.06**	**-2.35**	**2.71**

The calculated DFT simulation reveals that substitution of the carbamate chain onto the TEI unit does yield identical planarity with the alkyl-substituted TEI polymer. Furthermore, the electrons in the polymer and monomer are evenly delocalized in both the HOMO and LUMO levels indicating good π-π stacking, and good carrier transfer along the polymer, vital for photovoltaic cells. It should be noted that the DFT simulation predicted the HOMO level of the PTEI carbamate chain to be -5.26 eV while the PTEI alkyl chain predicted -5.06 eV. From the HOMO/LUMO predictions, it is evident that PTEI carbamate gave a deeper HOMO level than the alkyl chain giving rise to a better optical bandgap which could potentially enhance the V_{OC}. The estimated low-lying and widely delocalized energy levels of the PTEI carbamate suggest an even better candidate polymer for wide bandgap donor polymers. E_{LUMO} values derived from the DFT calculations may deviate significantly from actual values. This is because the LUMO orbitals do not contain any electrons, hence the calculations assume that excited electrons fill the imaginary molecular orbitals. Moreover, it should be noted that the synthesis of TEI can result in a possible geometric isomerization due to the vinyl linkage coupling between the thiophene and indigo units. However, the Knoevenagel condensation process only results in Z-form geometric isomers. But after the addition of the carbamate chain, it gave rise to the E isomer with a Z:E ratio of 6:1.

2.2.2 Synthesis Scheme of TEIBDT Polymer

Polymer TEIBDT was synthesized in 4 steps using the route shown below. The first step involves a Knoevenagel condensation reaction between 6-bromoindolin and 5-bromothiophene-2-carbaldehyde. [68] It should be noted the bromine groups are already attached to minimize synthetic complexity. The next steps involve the substitution of the carbamate chain on the indigo nitrogen atom. But before substitution, the carbamate chain was synthesized first. This is done by converting the long decyl-tetradecanol alcohol into 2-decyltetradecyl carbonochloridate using triphosgene by a mechanism known as chloroformylation. After the successful substitution of the carbamate chain on the TEI unit, it is then verified by NMR to check purity. After verifying the purity, the TEI unit is polymerized with the BDT donor unit via Stillie coupling polymerization in the presence of $Pd_2(dba)_3/P(o\text{-tolyl})_3$ in degassed chlorobenzene. The polymer is then collected and washed with methanol to remove the remaining catalyst and other impurities. Next, the purification process of the polymer begins with Soxhlet extraction, cycling through acetone, hexane, and chloroform, respectively. The polymer is then collected in the chloroform portion which indicates high molecular weight and good solubility.

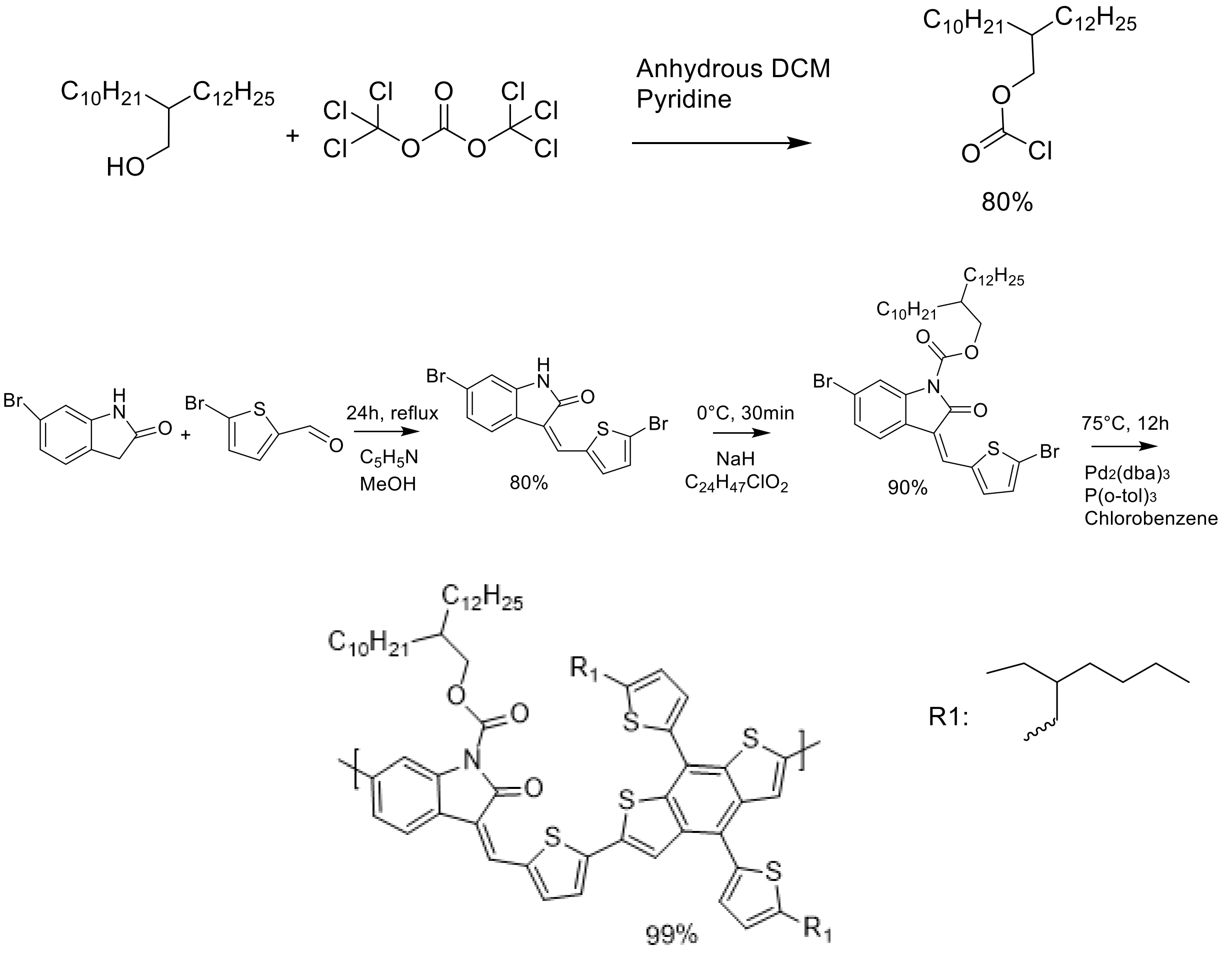

Figure 2-5 Synthesis scheme for TEIBDT carbamate substituted polymer

2.3 Characterization of TEIBDT Polymer

2.3.1 Physical Properties (GPC, TGA, and DSC)

For the purpose of determining the molecular weight of TEIBDT, high-temperature gel permeation chromatography (HT-GPC) was carried out at 150 °C with 1,2,4-trichlorobenzene serving as the eluent and polystyrene acting as the standard. The number average molecular weight (M_n) of TEIBDT is 21.8 kDa whereas the weight average molecular weight (M_w) is 52.8 kDa. The polydispersity index of the polymer is 2.42.

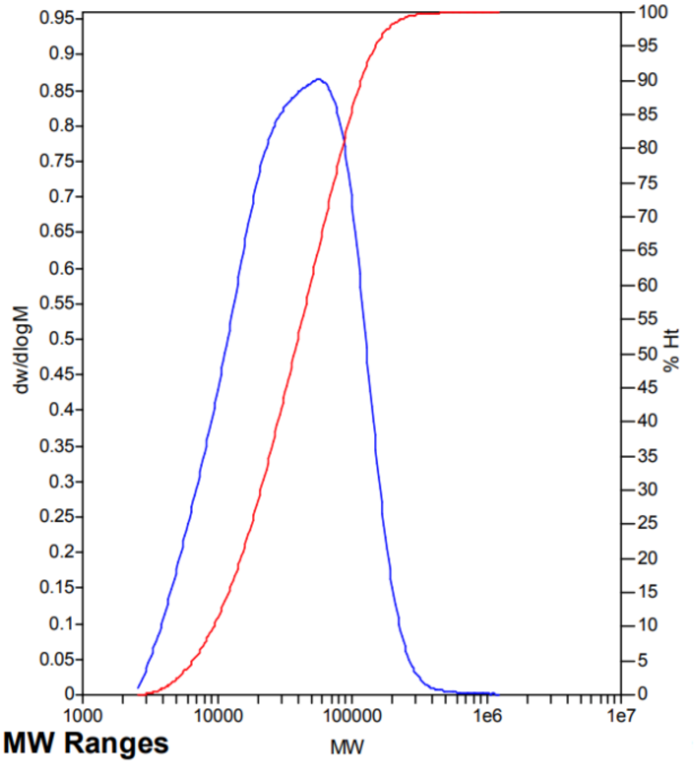

Figure 2-6 HT-GPC molecular weight distribution of TEIBDT

Table 2-2 Molecular weight and polydispersity index of TEIBDT

Polymer	M_n (kDa)	M_w (kDa)	PDI
TEIBDT	21.8	52.8	2.42

Thermalgravimetric analysis (TGA) and differential scanning calorimetry (DSC) were conducted to study its thermal stability as well as the thermolability property of the carbamate side chain. The polymer was heated in air at a heating rate of 10 °C min^{-1} from 25 °C, and held at 250 °C for 20 min, then heated at 10 °C min^{-1} until 600 °C. As shown in **Figure 2-7 (a)**, polymer TEIBDT lost 1.5 % weight at 250 °C which is much lower than the anticipated loss of 41.3%. Based on our previous studies by Ngai et al on hemi-isoindigo polymers [77-78], the theoretical loss and the anticipated loss of the side chain cleavage were quite similar to each other, however for polymer PTEI, the anticipated loss was much lower. [77] This is due to the presence of the long-branched carbon 24 chain on PTEI giving it a higher melting temperature and the ability to store more thermal energy per unit mass. This means, that the longer the carbamate chain, the more energy is required to thermally remove them.[77-78] With an increasing number of hydrocarbons on the side chains, there would be an increased molecular weight compared to the C8 chains reported previously. The higher molecular weights on the carbamate chains would have greater intermolecular forces (van der Waals attractive forces) and thus higher energy is required to trigger the thermal cleavage process. [77-78] Based on **Figure 2-7 (b)**, there were no obvious glass transitions, meaning there were no endothermic and exothermic transitions found on their differential scanning calorimetry thermograms up to 300 °C.

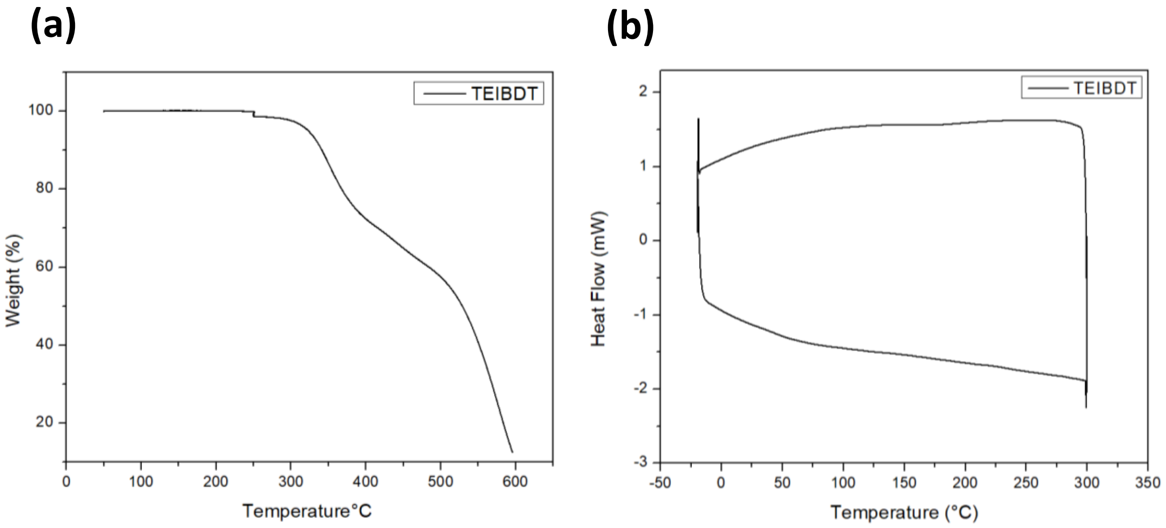

Figure 2-7 (a) TGA curve **(b)** DSC curve for TEIBDT

2.4 Optical and Electrochemical Properties of TEIBDT

The normalized UV-vis absorption spectra of polymer TEI is shown in **Figure 2-8 (a)**. Both the thin film and solution were processed in chloroform. From the spectra, TEI shows two distinct absorption bands. The band that is below ~400 nm shows the localized π-π transitions while the band between 500-650 nm shows a strong intramolecular charge transfer between the electron deficient TEI unit and the electron rich BDT unit. There is also a strong indication of aggregation effects in the solution, as their absorption peaks from the solution to the film show negligible red shifts. [68] From the UV-vis absorption, PTEI exhibits strong absorption in the range of 300-700 nm, affording well-matched complementary absorption with the acceptor Y6, indicating that the polymer:Y6 blend films possess good light-harvesting potential. [68] The electrochemical properties are exhibited on the CV plot in **Figure 2-8 (b)**. Based on the onset oxidation-reduction potential the HOMO and LUMO energy are -5.47 eV and -3.78 eV, respectively at room temperature while the annealed film at 200 °C shows a deeper HOMO level of -5.51 eV and LUMO level of -3.84 eV. When comparing the theoretical calculations by DFT to the actual values, they both show similar results. As expected the carbamate substituted TEI polymer exhibited a deeper HOMO. And thus, in consideration of this much lower-lying HOMO level, a higher V_{OC} value is expected. Also, when comparing to H. Li et al [68] work with the alkyl-substituted PTEI-H polymer, the value of the alkyl-substituted TEI polymer shows a higher HOMO level of -5.37 eV and LUMO level of -3.50 eV.

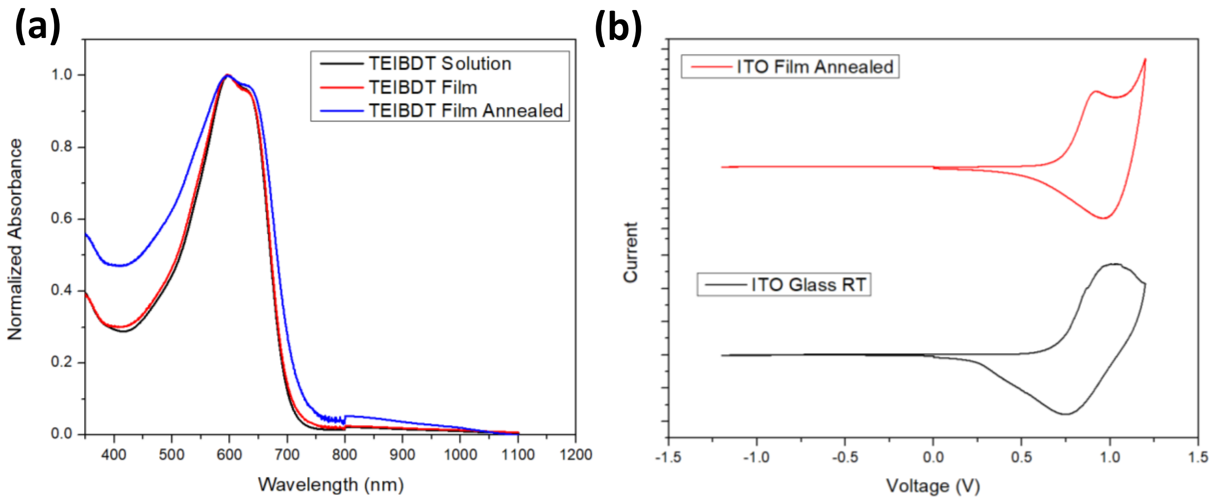

Figure 2-8 Optical and electrochemical properties of TEIBDT **(a)** Normalized UV-vis spectra of TEIBDT solution and thin films at room temperature and at 220 °C (**b)** Cyclic voltammetry profiles with 0.1M $[n\text{-}Bu_4N]^+[PF6]^-$ in acetonitrile electrolyte at a scan rate of $0.1Vs^{-1}$

Table 2-3 Optical and electrochemical properties of TEIBDT and Y6

Donor Polymer	**λ_{max}, (nm)**	**λ_{onset}, (nm)**	**E_g^{opt} (eV)**	**E_{HOMO} (eV)**	**E_{LUMO} (eV)**
PTEI	**594**	**732**	**1.69**	**-5.47**	**-3.78**
PTEI-Annealed (200°C/20min)	**593**	**743**	**1.67**	**-5.51**	**-3.84**
Acceptor	**λ_{max}, (nm)**	**λ_{onset}, (nm)**	**E_g^{opt} (eV)**	**E_{HOMO} (eV)**	**E_{LUMO} (eV)**
Y6	**830**	**933**	**1.33**	**-5.71**	**-4.10**

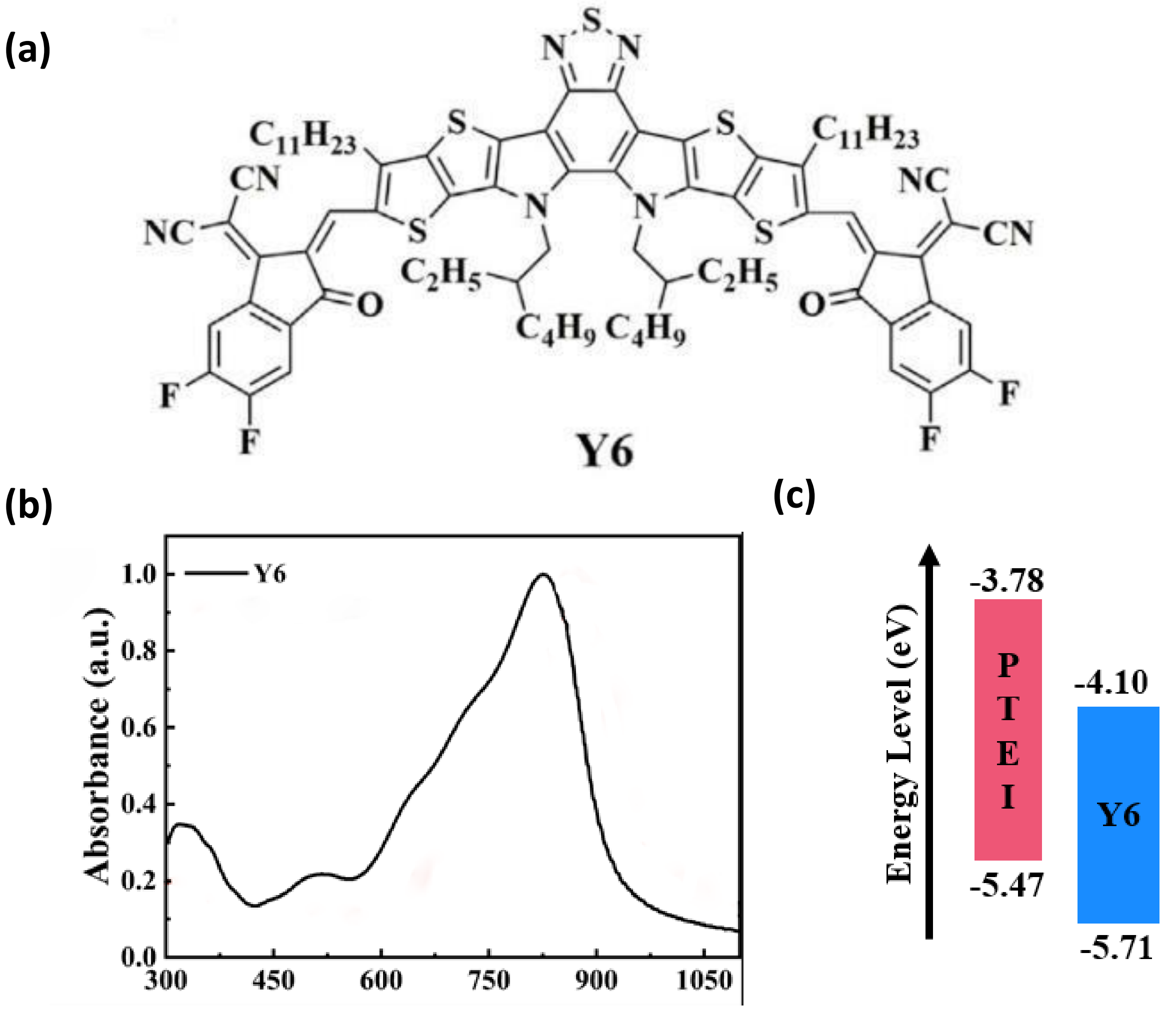

Figure 2-9 (a) Chemical structure of non-fullerene acceptor Y6 **(b)** UV-vis Spectra of Y6 [69] **(c)** energy level diagram of TEIBDT and Y6

Similar to H. Li et al work [68], polymer PTEI was chosen to match with the non-fullerene acceptor Y6 because of its broad absorption range of 600 nm to 1000 nm and its low-lying E_{HOMO} as it allows for an increased J_{SC} value. Summarized from **Table 2-3**, it is apparent that the difference between the PTEI E_{HOMO} and Y6 acceptor E_{HOMO} is about 0.24 eV which is sufficient enough for exciton dissociation in the acceptor phase. Meanwhile, the E_{LUMO} level energy offset between the PTEI and Y6 is 0.32 eV, which is preferred for limiting the energy loss of the OSC devices. Although there are other non-fullerene acceptors like (3PS)2-SiPc which is based on a silicon phthalocyanine derivative that has a relatively high E_{HOMO} and E_{LUMO} level beneficial for enhancing the V_{OC} of the acceptor component, its absorption range would render it useless because of the poor light harvesting potential for polymer PTEI.

Prior to the fabrication of OSCs, the photoluminescence quenching efficiency (PLQE) approach was used to study the exciton diffusion and dissociation performance of the donor and acceptor blend films. The polymer TEIBDT was stimulated at 610 nm, which is the wavelength of the greatest absorption peak and the lowest absorption intensity for Y6. After stimulation, the light emission is quenched in the D-A blend films due to the presence of the acceptor. The PL spectra in **Figure 2-10** reveals the PLQE of TEIBDT blending with acceptor Y6 was 96.7% whereas the PLQE of Y6 with the introduction of TEIBDT was 90.1%. It is evident that TEIBDT:Y6 shows excellent exciton dissociation performance, which is a great precursor for satisfactory solar cell performance.

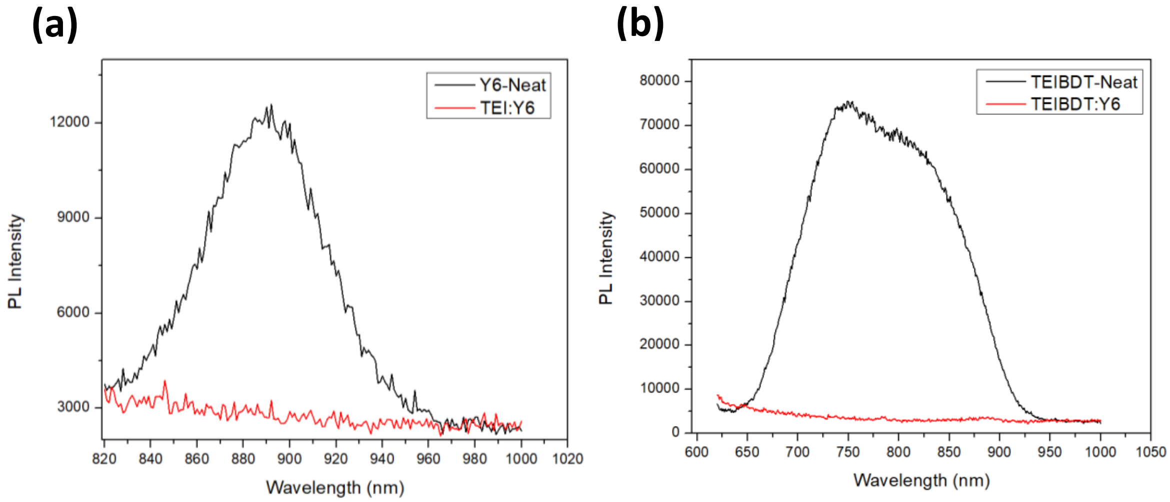

Figure 2-10 (a) Photoluminescence spectra of TEIBDT neat and Y6 neat excited at 820nm **(b)** TEIBDT neat and TEIBDT:Y6 blend film excited at 620 nm

2.5 Organic Solar Cell Performance of TEIBDT:Y6

The BHJ organic solar cells were fabricated utilizing an inverted configuration of ITO/ZnO/Active layer/MoO_3/Ag, using a 1:1 TEIBDT:Y6 ratio as the active layer. The polymer donor is processed in chloroform solution and is spin-coated on the ITO glass under different RPM, and in a nitrogen glove box at room temperature. Then are characterized under the illumination of AM 1.5G. (100 mWcm^{-2}). The hole transport layer and electron transport layer are deposited on the ITO glass using a vacuum evaporator where the vacuum allows vapor particles to travel directly to the ITO glass and condense back to their solid state. A more detailed method can be found under the experimental section in **2.9.2**.

Table 2-4 Summary of OSC performance of TEIBDT:Y6

Parameter		J_{SC} (mAcm^{-2})	V_{OC} (V)	FF	PCE (%)
Temperature (°C)	Rotation Speed (RPM)				
RT	1500	21.48	0.66	0.41	6.55
RT	2000	20.95	0.68	0.50	6.98
RT	2500	22.07	0.68	0.45	6.82
50	1500	21.63	0.67	0.42	6.49
50	2000	20.03	0.70	0.55	7.60
50	2500	21.96	0.69	0.44	6.75
100	2000	20.60	0.70	0.56	8.00
100	2500	22.01	0.69	0.51	7.50
150	2500	17.51	0.67	0.51	5.88
200	2500	16.30	0.55	0.42	3.60

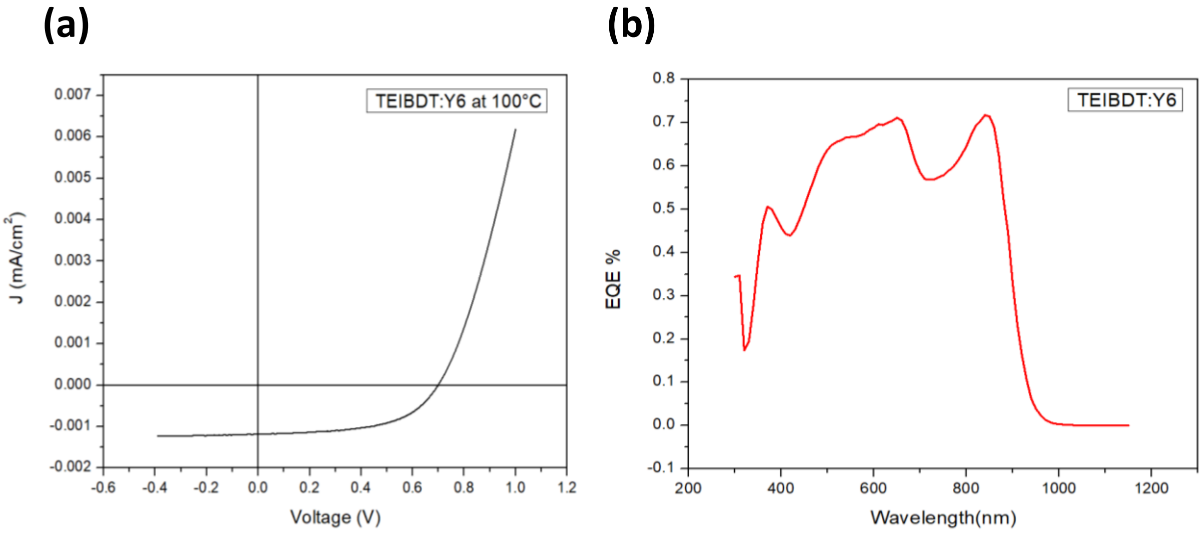

Figure 2-11 (a) J-V curve of TEIBDT:Y6 at 100°C **(b)** External Quantum Efficiency Curve of the optimized OSC based on TEIBDT:Y6

Table 2-4 summarizes the device performance based on PTEI:Y6. The study was optimized based on the annealing temperature and RPM speed of the spin coater with a 1:1 donor-acceptor ratio. And thus, the best devices were exhibited at 100 °C with an adequate PCE of 8.00 % (J_{SC} = 20.60 mAcm^{-2}, V_{OC} = 0.70, FF=0.56) and at 50°C with a similar PCE of 7.60 % (J_{SC} = 20.03 mAcm^{-2}, V_{OC} = 0.70, FF=0.55). When comparing to the alkyl-substituted PTEI:Y6 by H. Li et al, their best device was almost similar to the carbamate version. Their PCE exhibited 8.27% (8.05 % avg) with J_{SC} of 21.90 mAcm^{-2}, V_{OC} = 0.75 and FF of 50.1%. The alkyl substituted PTEI performed slightly better in terms of PCE due to a higher V_{OC} and slightly higher J_{SC}, but this all mainly comes down due to the longer side chain present on the carbamate PTEI version than the alkyl PTEI.

For this polymer, C24 was substituted instead of C20 which was used in the alkyl version to solubilize the polymer effectively in chloroform. If the C20 version of the carbamate could be processable in chloroform, then the carbamate chain would perform identically, if not better than the alkyl version. Generally, the larger the side chain, the better the solubility, but reduces the π-π interchain interaction, weakens lamellar packing, and imposes a weaker polymer domain and ultimately affecting the performance of the solar cell. The lamellar packing is greatly influenced by the orientation and steric structures at the molecular level. Higher molecular weights such as long chain lengths of the side chains tend to create a 2theta angle peak shift towards lower angles in crystalline compounds. The lower 2theta angle represents a longer d-spacing between repeating units in a crystal structure. As the side chain is larger, the pi-stacking would be reduced and the charge hopping distance between individual polymer molecules would also be shortened. This would lead to fewer charge carrier pathways within the bulk polymer and weakens charge transfer in semiconductors, so as OPV performance. Another plausible reason can be due to the fabrication process of the device hindering the PCE performance due to human error which can introduce defects such as air and chemical vapour during the vacuum deposition phase or spin coating phase to the OSC device, which can impact the overall PCE.

The carbamate substituted PTEI should have had a higher expected V_{OC} due to having a deeper E_{HOMO} level, which was also elucidated in the gaussian DFT prediction. However, the lower E_{LUMO} energy reduced the optical bandgap, and since the difference between the E_{HOMO} level and the E_{LUMO} level is low, this resulted in a medium bandgap polymer, which in turn resulted in a much lower V_{OC}. The J_{SC} was also slightly lower, which could be attributed to the optical bandgap (E_g) of the donor, as well as the weak lamellar packing discussed in the XRD section of the thesis. The FF however shows an improvement of 6% when comparing to H. Li et al's PTEI alkyl substituted polymer.

EQE was also measured for the PTEI:Y6 based organic solar cell which is the ratio of the number of charge carriers generated in a solar cell to the number of photons shining on the solar cell. This is studied to determine the photocurrent generation efficiency under different wavelengths. Based on the EQE spectrum, the highest value of 72% is shown between 500 nm - 650 nm, which indicates an unbalanced charge carrier mobility.

2.6 Charge Carrier Characteristics of TEIBDT

The charge transport characteristics in the TEIBDT blend films were investigated to further understand the polymer's photovoltaic characteristics. Thus, the space-charge-limited current (SCLC) approach was used to determine the electron/hole mobilities. The hole device was fabricated in the configuration of ITO/ PEDOT:PSS/ TEIBDT/MoO_3/Ag, and the electron-only device was fabricated in the configuration of ITO/ZnO/ TEIBDT/LiF/Al. The hole mobilities of the TEIBDT neat films are 1.06×10^{-4} $cm^2V^{-1}s^{-1}$. However, after blending with Y6, the hole mobilities of TEIBDT:Y6 decreased mildly to 9.35×10^{-5} $cm^2V^{-1}s^{-1}$. The higher SCLC hole mobility of the neat TEIBDT could be due to the enhanced crystallinity and face-on orientation tendency of TEIBDT after annealing.

In addition, the electron mobility of TEIBDT:Y6 was calculated to be 8.85 $\times 10^{-6}$ $cm^2V^{-1}s^{-1}$. For a typical high performing OSC device, the electron mobility should be $>10^4$ to achieve high PCE, however, a poorly balanced μ_h/μ_e of 0.1 was achieved with the TEIBDT:Y6 film blend. As a result, this enlarges the space charge accumulation and inhibits the charge transport and extraction, thus limiting the J_{SC} values in the corresponding devices. An alternative NFA acceptor can be used to improve the electron mobility so that the hole/electron mobility ratio can be balanced.

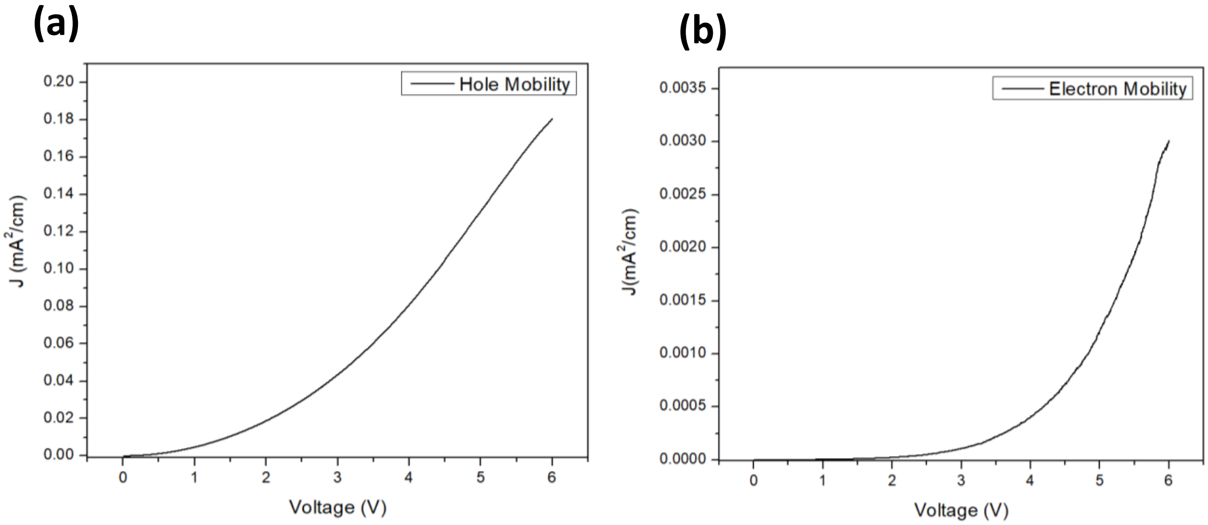

Figure 2-12 (a) Hole mobility curve **(b)** Electron Mobility Curve of TEIBDT:Y6

2.7 Morphology and Crystallinity Analysis of TEIBDT:Y6

2.7.1 Crystallinity Analysis by X-ray Diffraction

Two-dimensional grazing-incidence X-ray diffraction (2D-GIXD) of the polymer neat films with different annealing temperatures are shown in **Figure 2-13**. It is evident that TEIBDT displays an edge on orientation at $2\theta=3.6^o$ in the out of plane (OOP direction), as well as displaying a weaker second order crystalline peak (200) at $2\theta=4.92^o$ at RT, 50°C, and 100°C with similar intensity, respectively. The corresponding peaks at $2\theta=3.6^o$ and $2\theta=4.92^o$ display a lamellar d spacing of 2.45 nm and 1.79 nm, respectively. At higher annealing temperatures of 150 °C and

250 °C, the peaks disappear indicating that the polymer chain would have undergone disordered packing, and is the reason why performance dropped significantly above 100 °C. Interestingly, the in plane (IP) direction did not show any diffraction peaks.

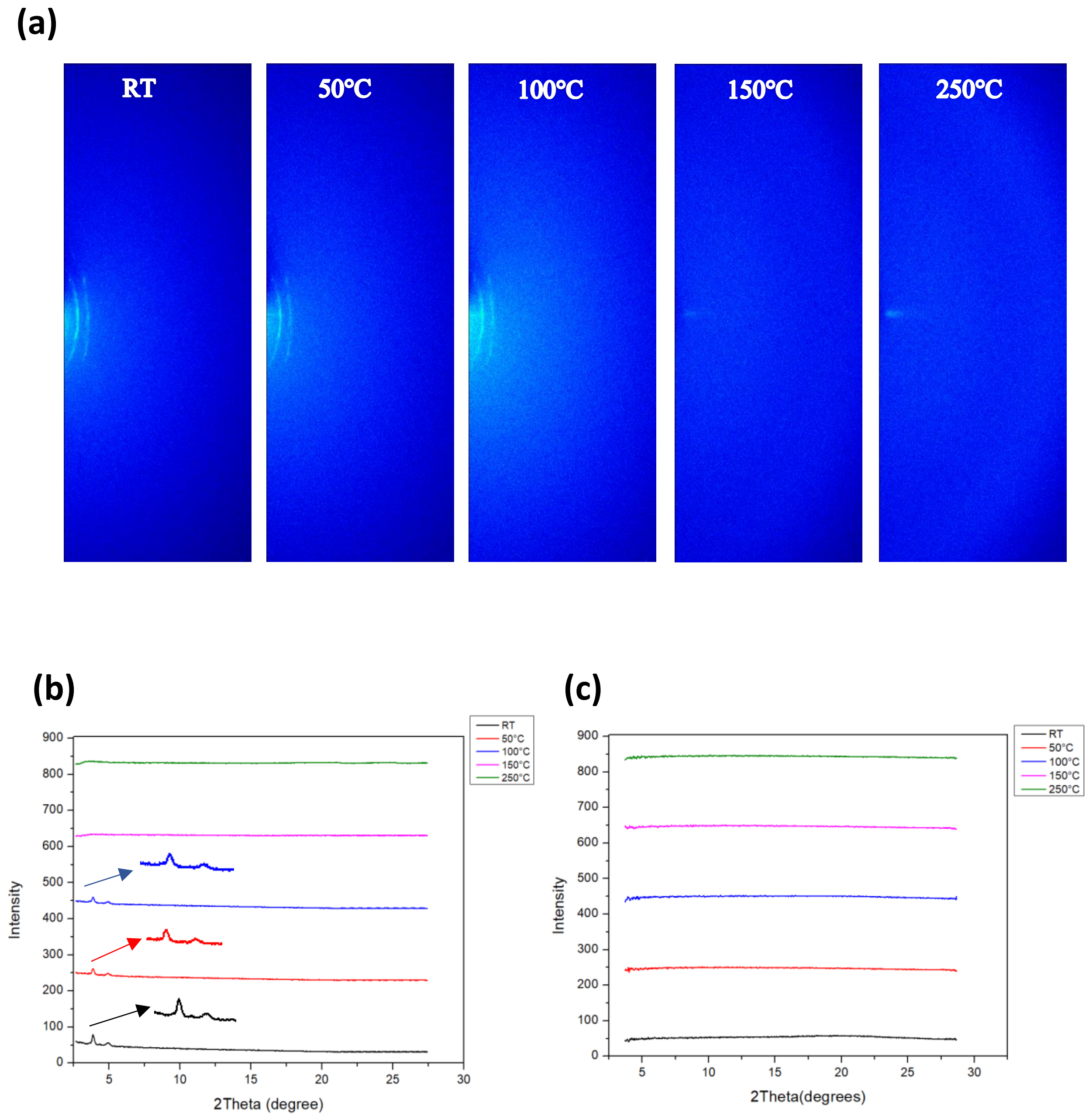

Figure 2-13 (a) GIXD images of TEIBDT at different annealing temperatures **(b)/(c)** GIXD plots in the OOP and IP direction, respectively. A closeup image is used for clarification

2.7.2 Morphology Analysis by AFM

The morphology of the TEIBDT:Y6 films were analyzed through AFM for the best optimal conditions for OSC performance. The blend films were processed in chloroform and spin coated on silicon substrates. Then annealed at 50°C and 100 °C. Based on the AFM images, it reveals that the surface morphology is slightly rough with an RMS value of 4.75 nm and 3.55 nm at 50°C and 100 °C, respectively. The crystalline characteristic of the TEIBDT correlates with the findings of the XRD, which is the cause of slight roughness in the material. In addition, average-sized domains can be observed, making the environment favorable for exciton dissociation and collection, which in turn leading to reasonable J_{SC} values. The high FF is attributed towards the miscibility between the TEIBDT and Y6 as a homogenous surface can be observed. At higher temperatures beyond 100 °C, the PCE decreases due to the RMS becoming smoother which is quite common for polymers.

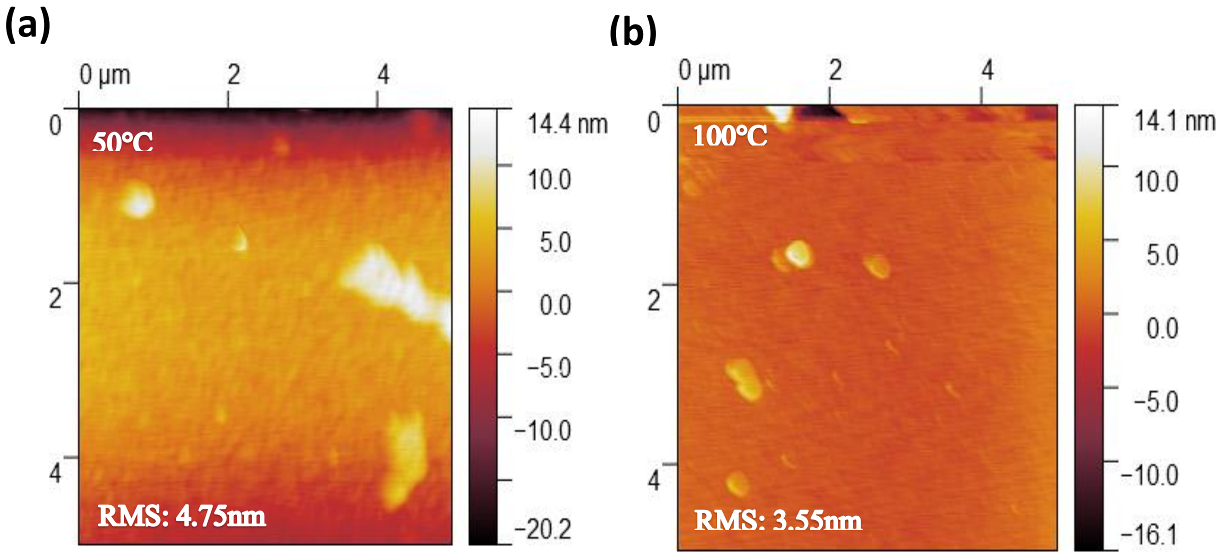

Figure 2-14 AFM height images (5µm x 5µm) of blend film **(a)** TEIBDT:Y6 at 50°C **(b)** TEIBDT:Y6 at 100°C

2.8 Summary and Future Work

In summary, a novel donor polymer based on the hemi-isoindigo backbone with the carbamate chain as the substituents were designed and synthesized. Polymer TEIBDT demonstrated a medium optical bandgap with a low-lying HOMO energy level. In essence, the carbamate chain was used to further improve upon the alkyl chain version of polymer TEIBDT. From the gaussian elucidations, the carbamate chain seemed to improve upon the HOMO level while also maintaining the backbone coplanarity and charge transfer ability, ultimately being better than the alkyl TEIBDT version. With these noteworthy findings, the V_{OC} should have been an improvement. After fabricating the OSC device based on TEIBDT: Y6 , it had achieved an adequate PCE of 8.00 % (J_{SC} = 20.60 $mAcm^{-2}$, V_{OC} = 0.70, FF=0.56) and at 50°C with a similar PCE of 7.60 % (J_{SC} = 20.03 $mAcm^{-2,}$ V_{OC} = 0.70, FF=0.55). According to the H. Li et al's alkyl version of the TEIBDT, their best PCE device exhibited 8.27% (8.05 % avg) with J_{SC} of 21.90 $mAcm^{-2}$, V_{OC} = 0.75 and FF of 50.1%. Furthermore, the SCLC mobility of TEIBDT showed a poor balance between the hole and electron mobility which is speculative upon the enlarged space charge accumulation and inhibition of the charge transport and extraction. From the two-dimensional grazing-incidence X-ray diffraction, it was evident of the importance of a face-on orientation and how it positively impacts efficiency. All in all, the carbamate PTEI version is similar in performance, if not identical to the alkyl PTEI version had the same length chain been used, but due to solubility issues, the C24 version had to be substituted. In conclusion, the carbamate chain is a great choice to improve upon performance and thus requires further studies to make the evidence more concrete.

In terms of future direction, the crystallinity of the polymer can be further improved by tuning the donor: acceptor weight ratio from 1:1 to 1:1.2. [70-73] This could potentially increase the electron mobility and balance the ratios between the hole/electron mobility to further reduce space charge accumulation and facilitate charge transportation and extraction more effectively. Similarly, other small molecule acceptors such as IT-4F or ITIC can be used to enhance the crystallinity and morphology. In regards to tuning the polymer, the donor portion of the polymer can be further enhanced by the introduction of halogen groups on the BDT which will further deepen the HOMO level and increase carrier mobility as well as improve upon crystallinity. [70-73] Other fine tuning of the polymer includes shortening of the alkyl chain to increase π-π stacking and reduce the steric effects, but is rather difficult to implement as the monomer is highly coplanar, preventing it to solubilize with shorter chains. Due to this reason, other polymer donors such as PBDTTPD should be explored so that a smaller size carbamate chain can be used to compare and contrast with the alkyl chain version.

2.9 Experimental Section

2.9.1 Materials and Characterization

Materials

All of the solvents and chemicals that were used in synthesis were purchased commercially from Sigma-Aldrich, VWR, TCL, Fluka and Armstrong. The solvents used for the purposes of fabrication and characterization were of HPLC grade with a 98.5% purity level. The silica gel (230-400 mesh) used for column chromatography was purchased from the University of Waterloo Chemstore.

NMR Spectroscopy

Nuclear Magnetic Resonance (NMR) Spectroscopy 1H NMR and 13C NMR spectroscopy were used for routine structural identification of the intermediates and the final products. The samples were dissolved in deuterated solvents such as CDCl3 (ALDRICH, 99.8 atom % D, contains 0.1 % (v/v) TMS), Acetone-d6 (ALDRICH, 99.9 atom % D, contains 0.1 % (v/v) TMS) or DMSO-d6 (ALDRICH, 99.5 atom % D, contains 0.1 % (v/v) TMS). The spectroscopies were recorded on a FT-NMR, 300 MHz (Bruker 300 UltraShield) spectrometer.

High-Temperature Gel Chromatography (HT-HPC)

HT-GPC was used to determine the weight characteristics of the polymers. More specifically, the number average (M_n), weight average (M_w) and polydispersity index were determined through the chromatograms. The measurements were performed using a Viscotek Malvern 350 HT-GPC system with 300 mm Jordi Gel DVB Mixed Bed liquid chromatography column. 1,2,4-trichlorobenzene was used as the eluent for polystyrene standards at 150 ºC and the samples were detected using a refractive index (RI) detector.

Atomic Force Microscopy (AFM)

Atomic force microscopy (AFM) images were taken with a Dimension 3100 scanning probe microscope. AFM analysis was used for the determination of surface morphology roughness of the polymer samples. AFM images were taken on dodecyltrichlorosilane modified SiO_2/p++Si substrates with a Dimension 3100 scanning probe microscope.

X-Ray Diffraction

X-ray diffraction (XRD) measurements were carried out on a Bruker D8 Advance diffractometer with Cu Ka radiation (λ = 0.15418 nm) using polymer films spin coated on SiO_2/Si substrates and polymer flakes.

Differential Scanning Calorimetry (DSC)

A differential scanning calorimeter was used to determine the melting temperature (T_m) and crystallization temperature (T_c) of the materials. For these measurements, a TA Instruments Q20 Differential Scanning Calorimeter was used. The samples were scanned at a rate of 10 °C min^{-1} for one heating and one cooling cycle in a nitrogen environment.

Cyclic Voltammetry (CV)

The oxidative and reductive potentials of the synthesized compounds were calculated using cyclic voltammetry. An electrochemical analyzer CHI600E was used to make the determination. The relevant samples were dropped and cast onto an indium tin oxide (ITO) glass and the analysis was carried out at a scan rate of 50 mVs^{-1} using a 0.1M solution of tetrabutylammonium hexafluorophosphate (Bu_4NPF_6) in acetonitrile (ACN) as the electrolyte. The internal standard was ferrocene, and its E_{HOMO} level is known to be -4.80 eV. A platinum wire served as the auxiliary electrode, while the ITO glass served as the working electrode, and silver/silver chloride served as the reference electrode.

Ultraviolet-Visible Spectroscopy

To determine the optical characteristics of the materials produced, such as absorption maximum wavelength and absorption onset, a UV-VIS absorption spectroscopy was performed. All spectra were captured using either a Cary 7000 UMS UV-Vis-NIR spectrophotometer or a Thermo Scientific GENESYS^{TM} 10S VIS spectrophotometer.

2.9.2 Fabrication of Organic Solar Cells

The OSCs fabricated followed an inverted BHJ structure and were built layer by layer in ITO/ZnO/Active layer/MoO_3/Ag. The ITO electrode served as the cathode, while the Ag electrode served as the anode. The ITO glass substrates were cleaned and sonicated in DI water, acetone, and iso-propanol, respectively, for 20 minutes each, then were dried under nitrogen for 5 minutes. The ITO glass substrates were then treated with a plasma cleaner for 10 minutes to remove further dust particles. After finishing with the plasma cleaner, the ITO glasses were placed on the spin coater to deposit the ZnO layer (40nm). The ZnO layers were then annealed at 200 °C on the hot plate for 60 minutes. Shortly after, the ITO glasses were put in the glove box so that the D:A active layer (TEIBDT:Y6) could be spin-coated on the ITO. The active layer was prepared ahead of time by mixing a 1:1 ratio of the polymer and acceptor Y6 and stirred overnight in a glovebox. Following that day, the D:A active layer was filtered using a 0.45µm PTFE syringe. After the successful deposition of the polymers via spin coating, they were annealed at the corresponding temperatures as described in the thesis. A thermal evaporator was used to deposit 10nm MoO_3 and 100nm of Ag electrode under vacuum conditions of $1x10^{-6}$ torr. The J-V curve was measured using Agilent B2912A semiconductor Analyzer with Science Tech SLB300-A Solar Simulator. Each solar cell's active area is 0.0574 cm^2. The light source was a 450W xenon lamp with an air mass (AM) 1.5 filter.

2.9.3 Synthesis Procedures

Synthesis of 2-decyltetradecyl carbonochloridate [1]

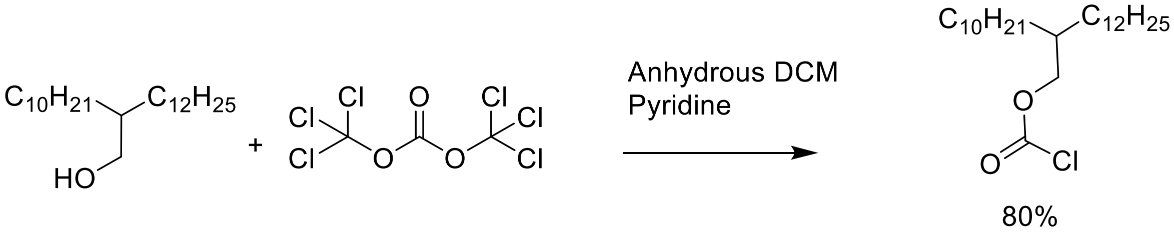

To a 500 mL two-neck round bottom flask, 2-Decyl-1-tetradecanol (11.90 mL, 33.4 mmol) was added. One neck of the flask was fitted with a condenser and the other neck was stopped with a rubber septum. The flask was then vacuumed and purged three times to allow a nitrogen only environment. Dichloromethane (70 mL) was added via a syringe and was cooled to 0 ºC with ice.

Pyridine (3.11 mL) was then added to the mixture via syringe, dropwise, resulting in a light pink solution. After 15 minutes of stirring, triphosgene (3.98 g) was added through the rubber septum by removing the septum and quickly depositing the bulk solid with weighing paper. The rubber septum was then replaced with a glass stopper. The resulting mixture was stirred at 0°C for 30 minutes. The mixture was extracted with hexane to filter out the pyridine salt formed in the reaction mixture. Column chromatography was performed with n-hexane as the eluent to afford the transparent product 2-decyltetradecyl carbonochloridate. -^{1}H NMR (300 MHz, chloroform-d) δ 4.21 (d, 2H), 8.07 (s, 1H), 1.72 (s, 1H), 1.27 (d, 35H), 0.87 (t, 8H), **(76% yield)**

Synthesis of 2H-Indol-2-one, 6-bromo-3-[(5-bromo-2-thienyl)methylene]-1,3-dihydro-,(3Z)- [2]

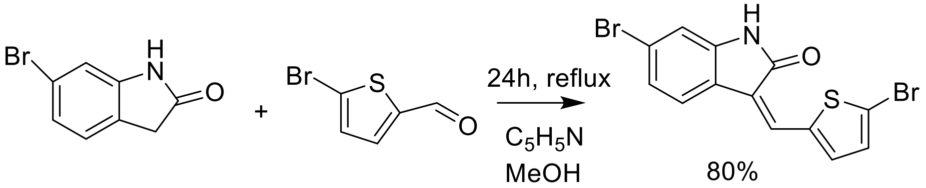

To a 100 mL two-neck round bottom flask, 6-bromooxindole (2.33 g, 11 mmol) and 5-bromothiophene-2-carbaldehyde (1.91 g, 10 mmol) were added to a solution of methanol (30mL). One neck of the flask was fitted with a condenser and the other neck was stoppered with a rubber septum. Piperidine (3.5 mL) was added dropwise via a syringe. The reaction mixture was refluxed for 24 hours in the presence of nitrogen. After 24 hours had passed, the reaction mixture was cooled and filtered by a Buchner funnel. The resulting mixture was washed with water, methanol, and ethyl acetate three times and dried under vacuum to afford the yellow solid product 2H-Indol-2-one, 6-bromo-3-[(5-bromo-2-thienyl)methylene]-1,3-dihydro-,(3Z)- ^{1}H NMR (300 MHz, dimethyl sulfoxide-d6) δ 10.69 (s, 1H), 8.07 (s, 1H), 7.66 (d, 1H), 7.61 (d, 1H), 7.37 (d, 1H), 7.23 (t, 1H), 7.01 (t, 1H), 6.87 (d, 1H), (**80% yield**)

Synthesis of 2-decyltetradecyl (Z)-6-bromo-3-((5-bromothiophen-2-yl)methylene)-2-oxoindoline-1-carboxylate [3]

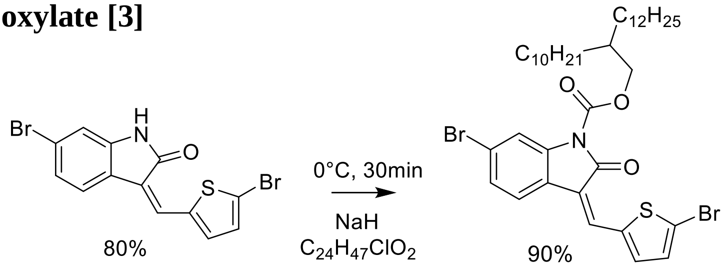

To a 100 mL two-neck round bottom flask, [2] (1 g, 2.6 mmol) was added to the flask via weighing paper. Using a nitrogen glove bag, sodium hydride (0.16 g, 6.65 mmol) was retrieved and added to the round bottom flask. The flask was fitted with a condenser and the other neck was stopped with a rubber septum. The flask was then vacuumed and purged for three times to allow nitrogen into the system. A solution of anhydrous tetrahydrafuran (20 mL) was added via syringe and cooled to 0ºC with ice. [1] was added dropwise and the reaction mixture was left to react for 30 minutes. After 30 minutes, the reaction was extracted with ethyl acetate and washed with brine 3 times. The resulting mixture was dry packed with silica to perform dry loading column chromatography. The column was eluted with 4:1 n-hexane ethyl acetate to afford a yellow solution. Rotary evaporation was used to evacuate all of the remaining solvents and then placed into the fridge overnight. After 24 hours, the solid was rinsed with methanol and sonicated. The method was repeated three times to afford the pure yellow 2-decyltetradecyl (Z)-6-bromo-3-((5-bromothiophen-2-yl)methylene)-2-oxoindoline-1-carboxylate - ^{1}H NMR (300 MHz, chloroform-d) 8.07 (s, 1H), 7.61 (s, 1H), 7.63 (m, 3H), 7.15 (s, 1H), 4.34 (d, 2H), 1.85 (s, 1H), 1.24 (m, 35H), 0.85 (s, 8H) (**90% yield**)

Synthesis of 2-decyltetradecyl (Z)-3-((5-(4,8-bis(5-(2-ethylhexyl)thiophen-2-yl)-6-methylbenzo[1,2-b:5,4-b']dithiophen-2-yl)thiophen-2-yl)methylene)-6-methyl-2-oxoindoline-1-carboxylate

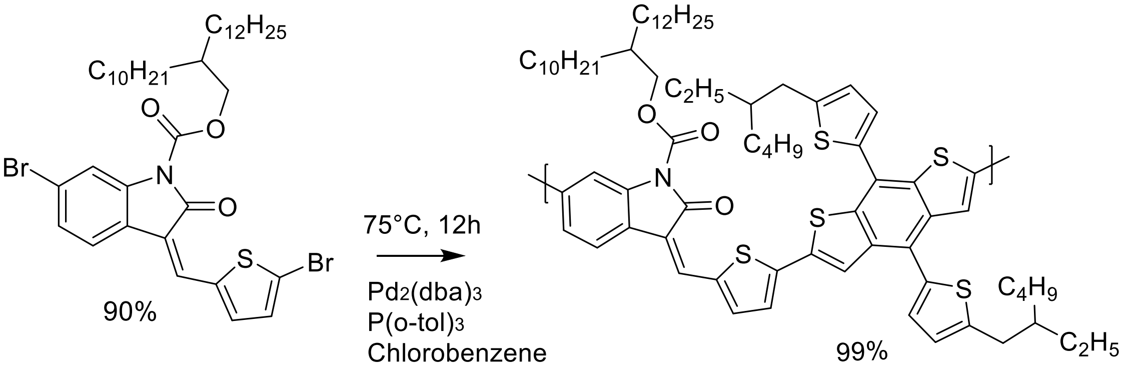

In a two-neck oven-dried round-bottom flask [3] (100 mg, 1.33 mmol) was added along with, 120 mg of 1,1′-[4,8-Bis[5-(2-ethylhexyl)-2-thienyl]benzo[1,2-b:4,5-b′]dithiophene-2,6-diyl]bis[1,1,1-trimethylstannane], 1.83 mg phosphine ligand tri(o-tolyl)phosphine (1.83 mg, 0.002 mmol). The flask was then fitted with a condenser and the other neck was stopped with a rubber septum. The flask was then vacuumed and purged for three times to allow argon into the system. Tris(dibenzylideneacetone)dipalladium(0), with a mass of 2.06 mg and a concentration of 0.002 mM, was first dissolved in 1 mL of degassed anhydrous chlorobenzene and then added to the reaction mixture. A silicon oil bath was utilized to get the temperature of the reaction mixture up to 75°C so that the Stille coupling reaction can proceed and was left to proceed unchecked for a full day before the temperature of the reaction was allowed to return to room temperature. The color of the reaction mixture changed from a yellow to a dark blue, which is an indication that the reaction progressed well. The reaction mixture was then precipitated by methanol and purified via Soxhlet extraction method, which calls for the following solvents in the following sequence: methanol, acetone, hexane, and chloroform to afford polymer 2-decyltetradecyl (Z)-3-((5-(4,8-bis(5-(2-ethylhexyl)thiophen-2-yl)-6-methylbenzo[1,2-b:5,4-b']dithiophen-2-yl)thiophen-2-yl)methylene)-6-methyl-2-oxoindoline-1-carboxylate (**99% yield**)

Chapter 3 Isoindigo Based OFET

3.1 Introduction

There have been many commercially available thin film transistors that provide good performance and high accuracy, however, they are usually based on inorganic materials such as metal oxides that require a harsh operating condition like 200-600 °C. [48-50] Harsh conditions like these can lead to potential safety issues and safety concerns due to the involvement of high power consumption. There has been great interest in the field of organic thin film transistors due to their variable applications for sensors, high sensitivity, and low cost. [48-52] Recently the advancement of organic thin film transistors has been on the rise because of the variety of applications they possess. For decades, D-A copolymer systems have been studied due to their superior TFT performance over homopolymers like P3HT. One such D-A system that is well studied is isoindigo. Their ease of synthesis and excellent optoelectronic characteristics make them extremely attractive towards OTFT-based sensors. One such example is Knopfmacher et al, which developed an isoindigo based ion sensor with silicon functionalized groups capable of sensing heavy metal ions such as mercury, in seawater. [73] Their discovery led to the potential of an inexpensive, inkjet printed, large-scale environmental monitoring device. Their polymer OFET sensor is capable of long-term stability and performance in aqueous environments with p-type behavior. In terms of performance, their $I_{ON/IOFF}$ ratio was 10^2 with mobility of 0.035 $cm^2 V^{-1}s^{-1}$. [73] All in all, the tunability of isoindigo led to a new realm of application for marine environments, which constituted a significant leap for organic electronics. Another novel study done by Lu C.F et al developed an isoindigo based gas sensor for high selectivity towards ammonia. [74] They reported excellent air stability with simple synthesis. Their systematic study was conducted to determine whether morphology control was imperative on the performance of the isoindigo gas sensor, and it revealed that strengthening the edge on morphology can enhance the sensitivity of the polymer. Another imperative study done by Saniye et al developed an anthracene isoindigo based polymer with single-walled carbon nanotubes for biosensor applications. [75] The sensor showed remarkable advantages for glucose detection including high sensitivity and low detection limit with a linear range of 0.05 mM to 1.0 mM with a sensitivity of 61.23 µA $mM^{-1}cm^{-2.}$ [75]

Thus, leveraging on the excellent stability of the isoindigo building block, in this chapter, we develop novel isoindigo-based donor-acceptor polymers that comprise of a thermo-cleavable electron donating carbamate side chain instead of a branched alkyl chain to enhance the performance of these polymers as chemical sensors. The strategy is to create abundant cavities in the polymer sensing layer through the removal of the side chain, which can facilitate the diffusion of the analyte molecules in the channel layer of OFETs, thereby increasing sensitivity. Additionally, polymer films after the removal of carbamate side chains become highly resistant to solvents, providing robust performance and long life to sensing devices.

3.2 Polymer Structure and Design

3.2.1 Computational Study of Polymer Structure

Similar to the DFT simulation performed on PTEI, polymer IDMT, IDBT and IDBDT are calculated under quantum mechanical iteration techniques provided in Avogadro 1.2.0, Gaussian 09, and Gaussian 16 software. Using the Merck molecular force field (MMFF94s) approach in Avogadro 1.2.0, a low-level energy minimization of the model compounds was done. Then, higher level geometry optimization and energy minimization of the model compounds were performed using Gaussian 09 or Gaussian 16 with the B3LYP level of theory and the 6-31G(d) basis set under tight convergence to investigate the optimized geometry and molecular orbital (MO) energy levels, respectively. The long decyl-tetradecyl chain was substituted with a methyl group to avoid computational complexity and time.

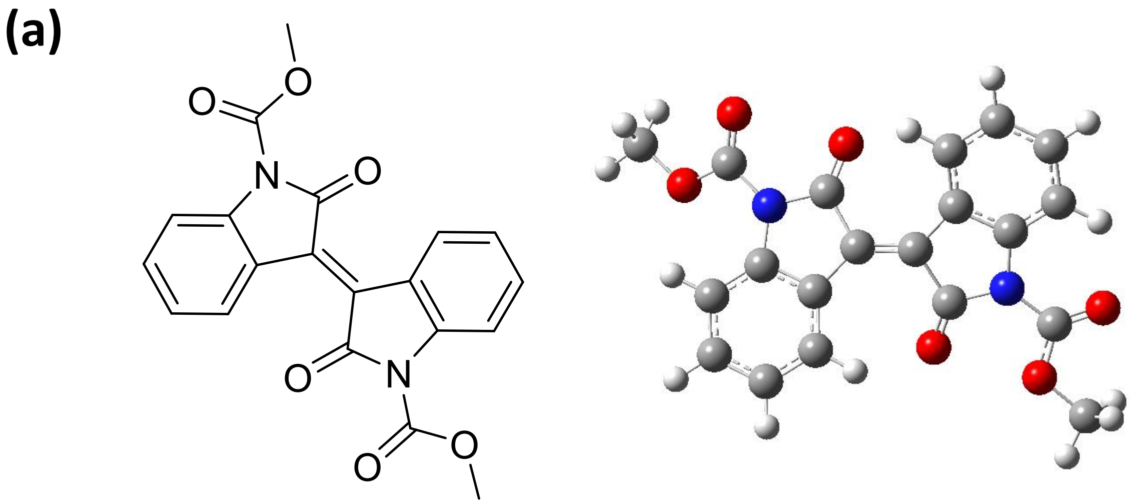

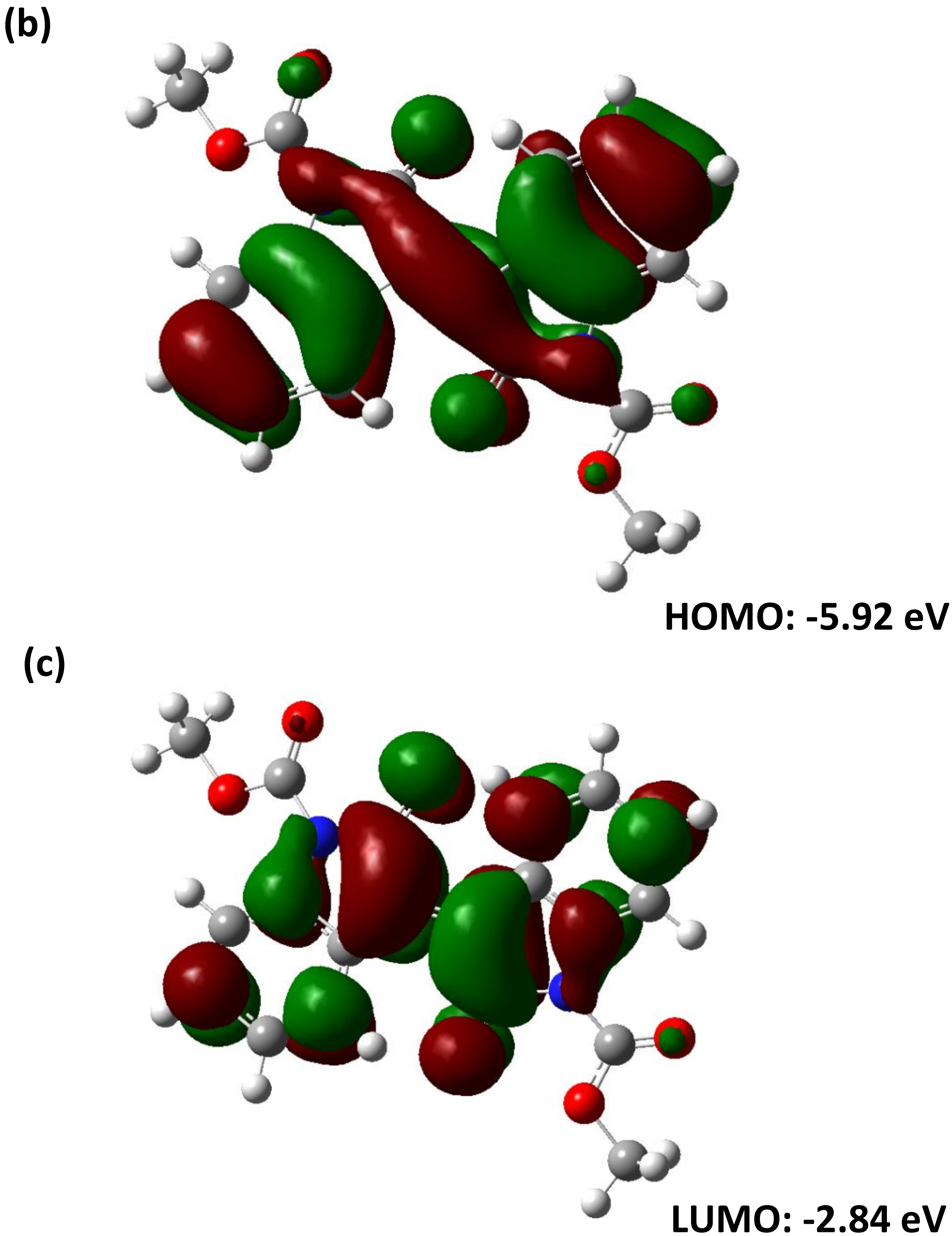

Figure 3-1 (a) Geometry of ID monomer optimized by DFT simulation **(b)** HOMO/(**c)** LUMO orbitals of ID with energy level respect vacuum (0 eV)

(a)

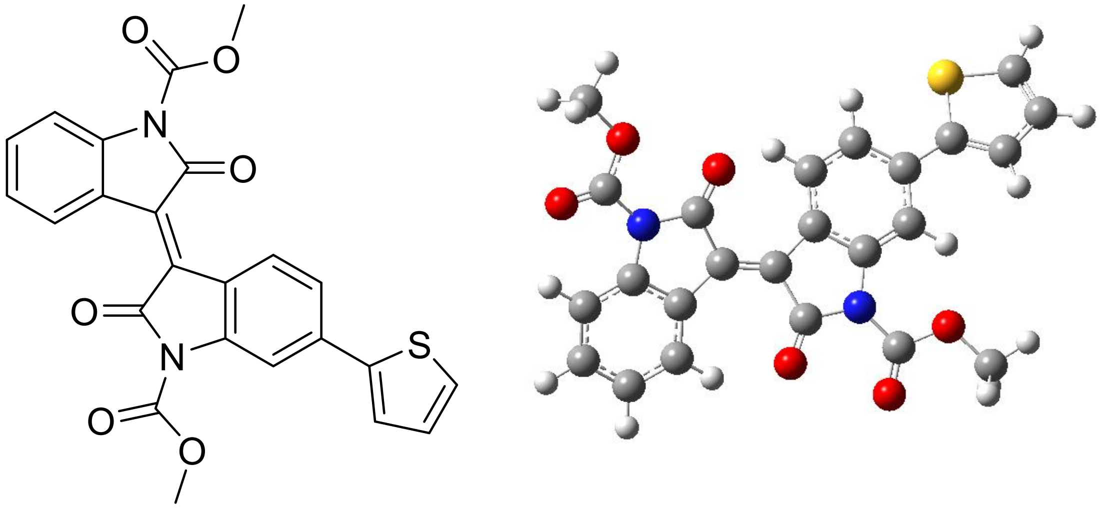

(b)

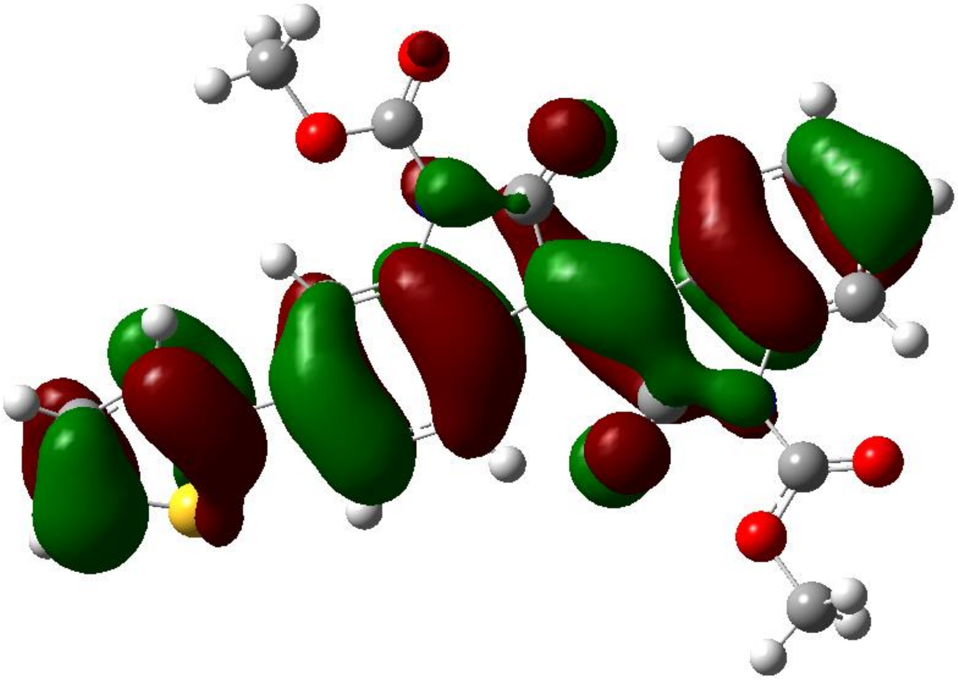

HOMO: -5.65 eV

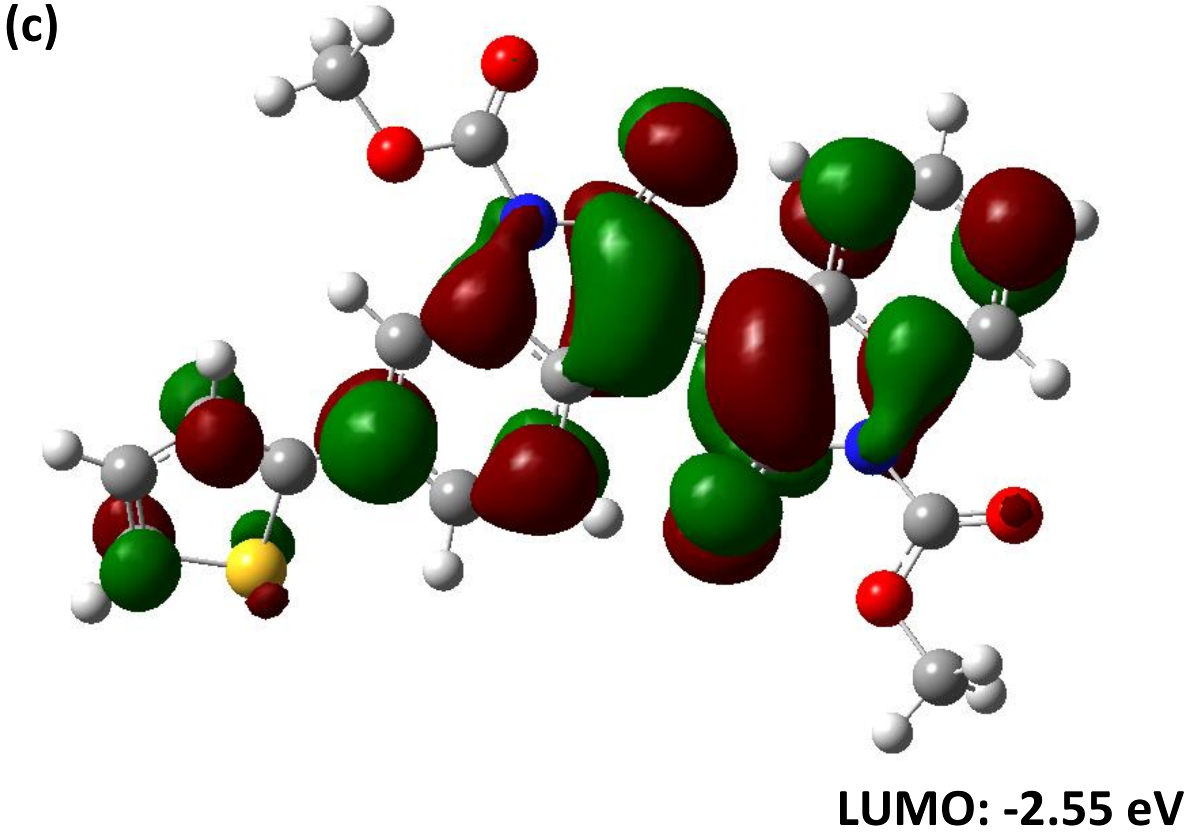

Figure 3-2 (a) Geometry of IDMT optimized by DFT simulation **(b)** HOMO/**(c)** LUMO orbitals of IDMT with energy level respect vacuum (0 eV)

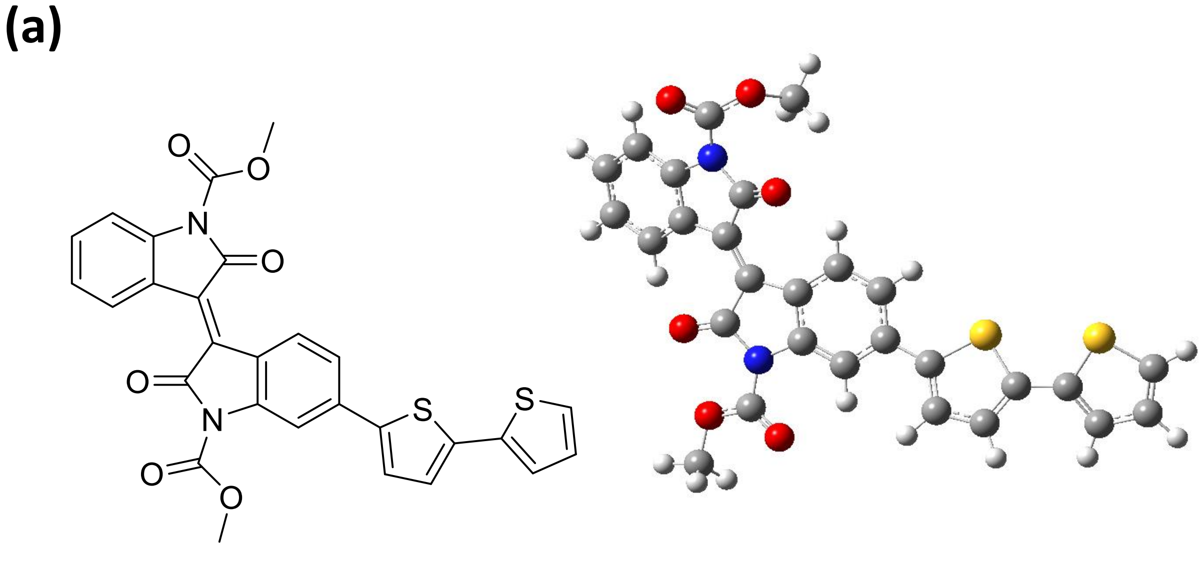

(b)

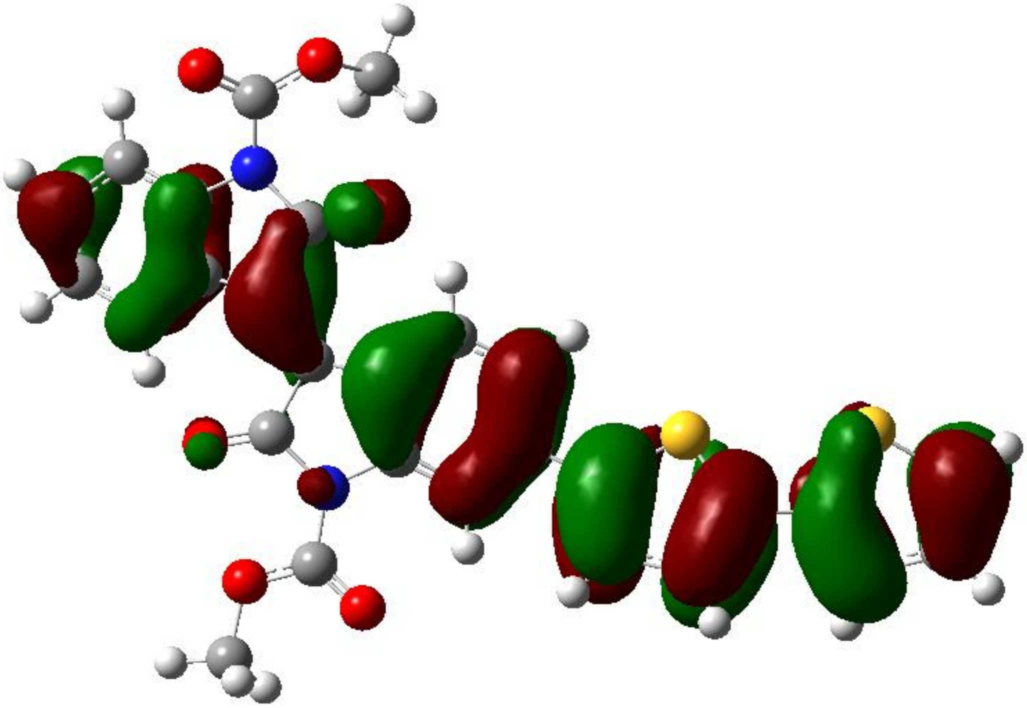

HOMO: -5.43 eV

(c)

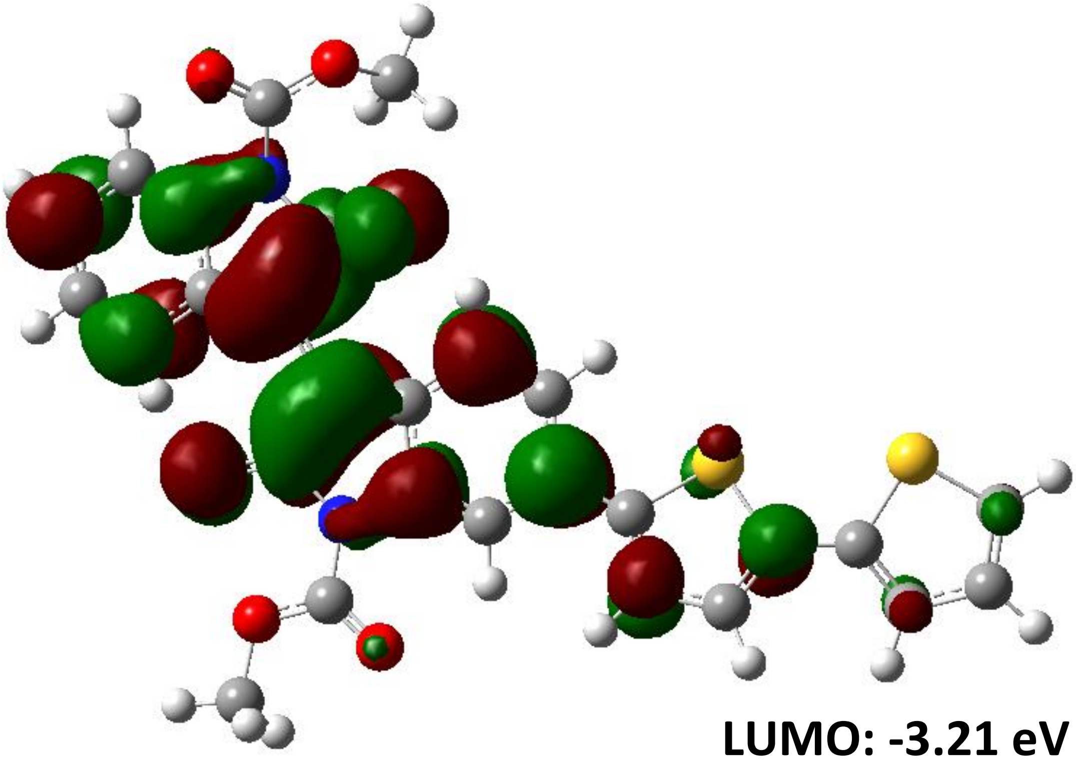

LUMO: -3.21 eV

Figure 3-3 (a) Geometry of IDBT optimized by DFT simulation **(b)** HOMO/**(c)** LUMO orbitals of IDBT with energy level respect vacuum (0 eV)

(a)

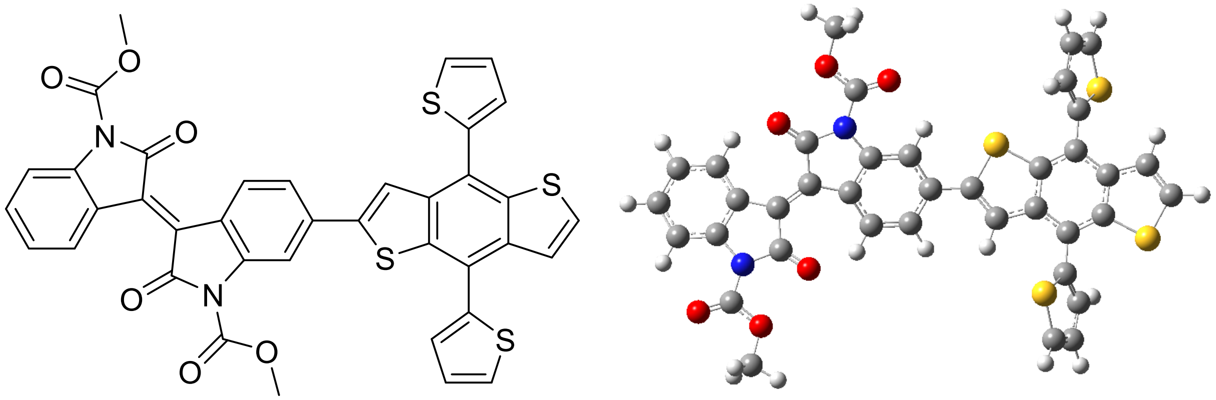

(b)

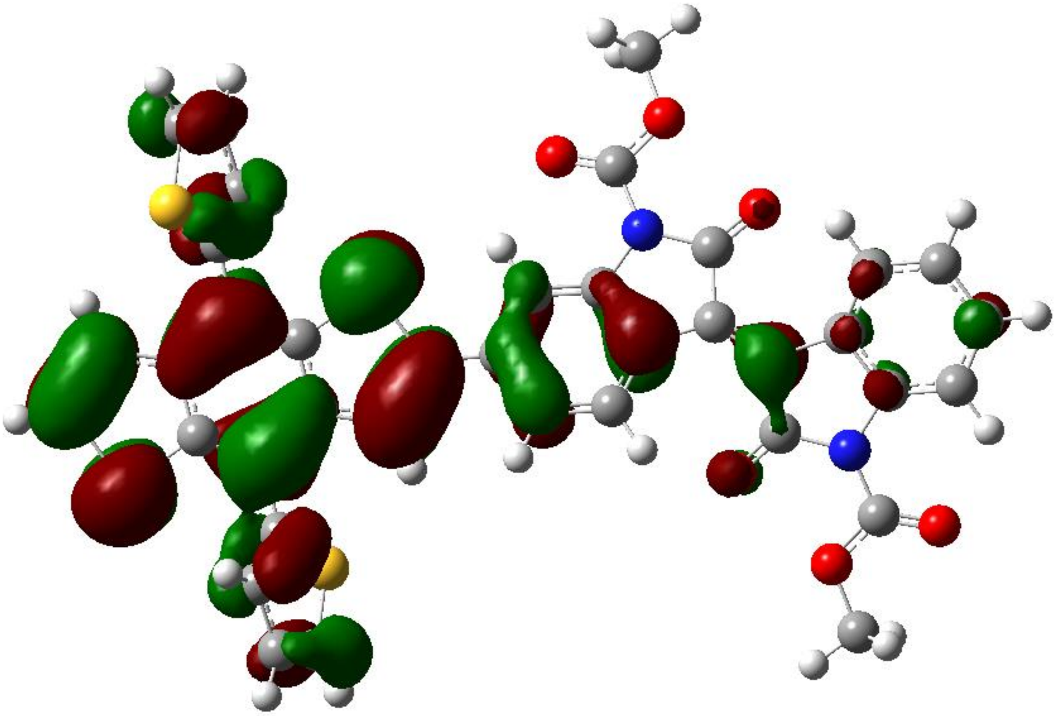

HOMO: -5.49 eV

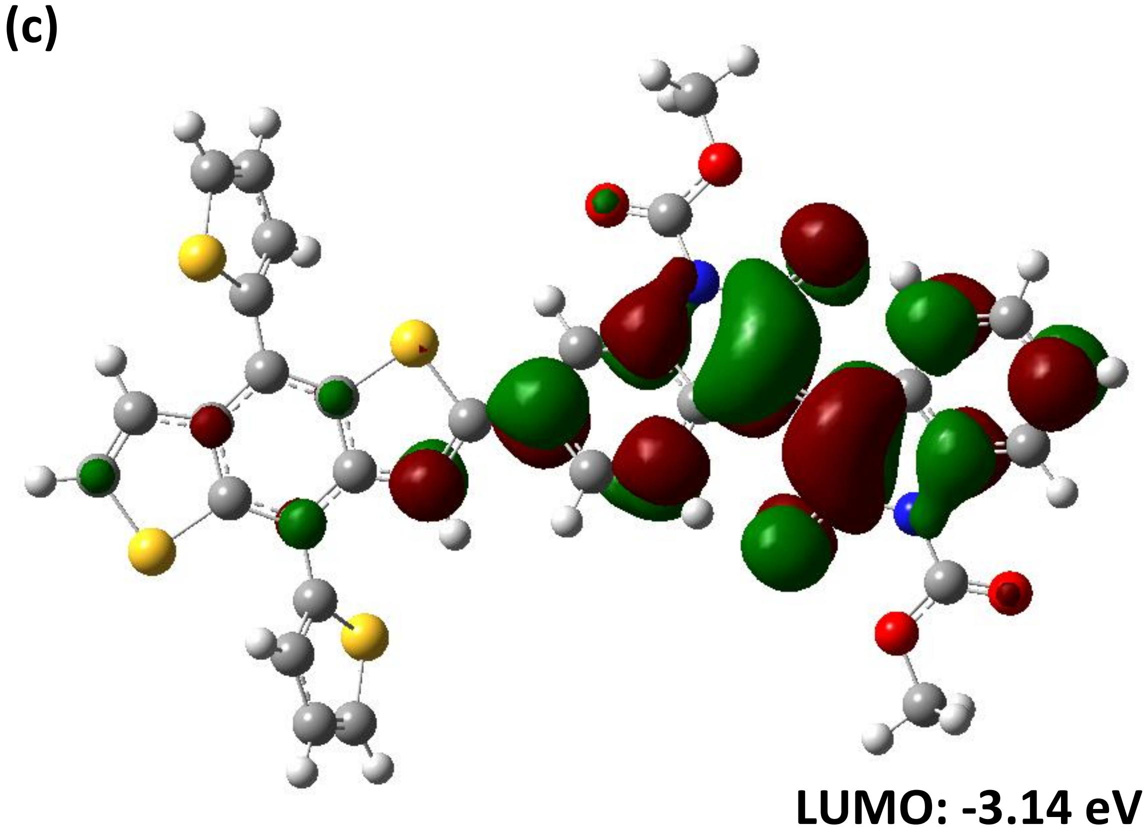

Figure 3-4 (a) Geometry of IDBDT optimized by DFT simulation **(b)** HOMO/**(c)** LUMO orbitals of IDBDT with energy level respect vacuum (0 eV)

Table 3-1 Summary of DFT calculation results of model

	DFT E_{HOMO} (eV)	**DFT E_{LUMO} (eV)**	**DFT E_g (eV)**	**Dihedral θ**
ID	**-5.92**	**-3.08**	**2.84**	**18.93**
IDMT	**-5.65**	**-3.10**	**2.55**	**18.69**
IDBT	**-5.43**	**-3.21**	**2.22**	**17.39**
IDBDT	**-5.49**	**-3.14**	**2.35**	**19.19**

The calculated DFT simulation reveals that substitution of the carbamate chain onto polymer IDMT, IDBT and IDBDT does maintain planar geometry. However, there is slight twisting on the carbon double bond which is to be expected. From **Table 3-1**, IDBDT showed the highest dihedral angle with 19.19° followed by IDMT with 18.69° and IDBT with 17.39°, respectively.

Furthermore, the electron density in all of the polymers are evenly delocalized in both the HOMO and LUMO wavefunctions for IDMT and IDBT, while the HOMO function for IDBDT is localized on the isoindigo unit and LUMO wavefunction are more localized on the BDT unit. Nonetheless, IDMT and IDBT show good π-π stacking, and good carrier transfer along the polymer, vital for organic field-effect applications. Furthermore, The DFT simulation predicts the HOMO level of the IDBT will be the highest followed by IDBDT and then IDMT, respectively. Similarly discussed before, E_{LUMO} values derived from the DFT calculations may deviate significantly from actual values as the LUMO orbitals do not contain any electrons, hence the calculations assume that excited electrons fill the imaginary molecular orbitals

3.2.2 Synthesis of PID Polymers

The synthesis of the PID polymers involves a 4-step sequence. The first step involves a chloroformylation reaction between the 2-octyldodecan-1-ol and triphosgene to form a 2-octyldodecyl carbonochloridate chloroformate chain at 0 ºC. The second step involves a condensation reaction between bromoisatin and bromo-oxindole aided by an acid catalyst such as hydrochloric acid and acetic acid to form 6,6-dibromoisoindigo. This is then followed by the substitution of the chloroformate chain on the dibromoisoindigo by deprotonation via sodium hydride at 0 ºC for 30 minutes to produce the PID monomer. After successful substitution, the PID monomer is polymerized via Stille coupling in the presence of $Pd_2(dba)_3/P(o\text{-tolyl})_3$ in degassed chlorobenzene with three different acceptors as indicated in the scheme. The polymers were then purified via Soxhlet extraction using methanol, acetone, hexane, and chloroform, respectively. To thermally cleave the carbamate chains, the polymers were subjected to 250 ºC in air for 20-30 minutes. The recovered yield for PIDMT, PIDBT and PIDBDT is about 40%, 30% and 99%, respectively. The general synthesis scheme can be seen in **Figure 3-5.**

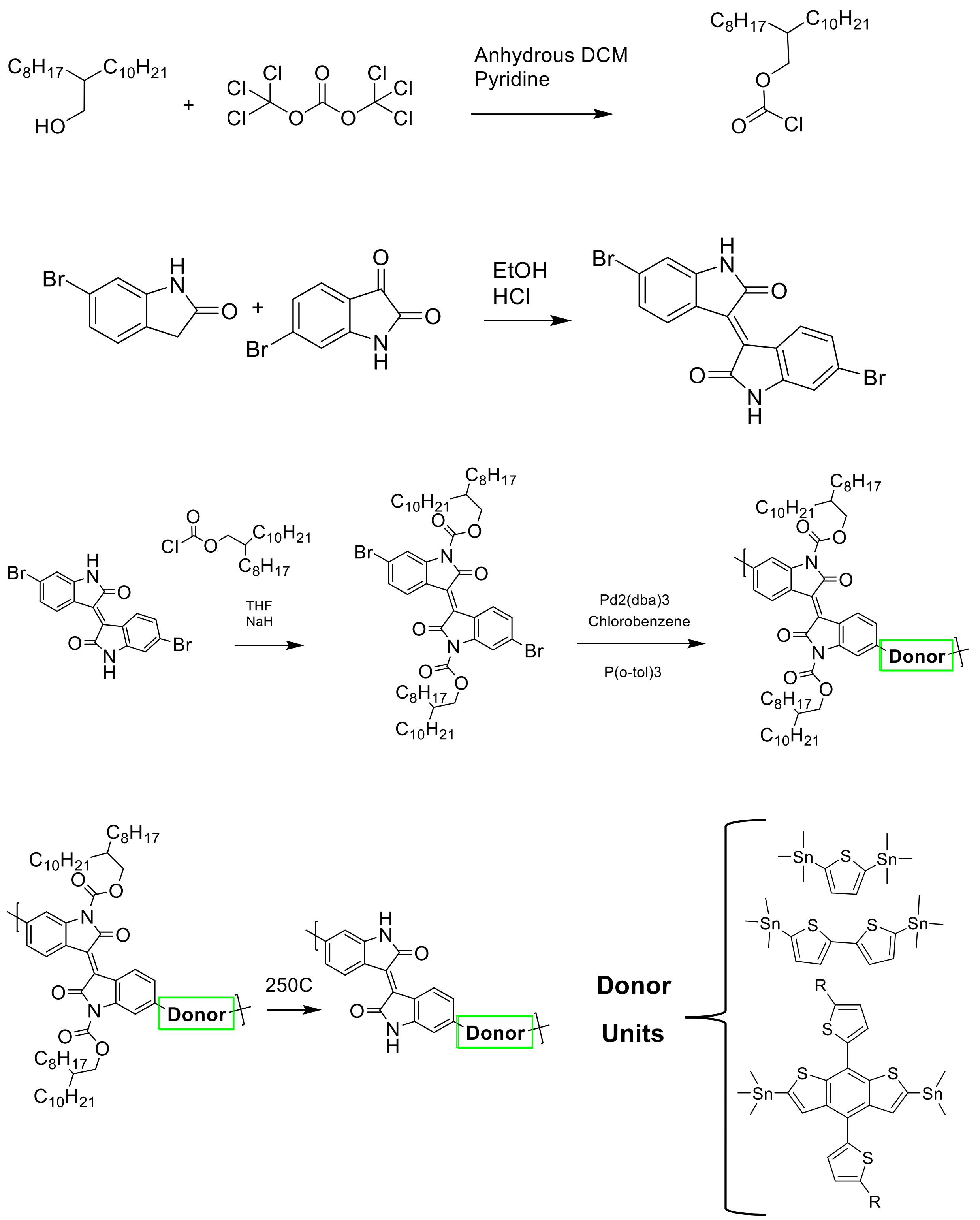

Figure 3-5 Synthesis scheme for PID carbamate substituted polymers, PIDMT, PIDBT and PIDBDT

3.3 Optical and Electrochemical Properties of PID Polymers

The optical characteristics are shown in **Figure 3-6 (a)**, in both solution and film states. Polymer PIDMT, PIDBT, and PIDBDT show two absorption characteristics that are typical for an isoindigo donor-acceptor molecule. The band between 300-450 nm represents a higher energy band which is attributed to the π- π* transition, while the band between 500-900 nm represents the intra-molecular charge transfer (ICT) between the donor and acceptor groups. In addition, the films for PIDMT and PIDBT show a slight bathochromic shift when compared to their solution counterparts, which could be due to their molecular packing. Usually, the more electron-rich a unit is, the greater the bathochromic shift.

Cyclic voltammetry (CV) was also carried out to study the electrochemical properties of the polymers, as shown in **Figure 3-6 (b)**. The calculated energy levels along with optical properties of three polymers are summarized in **Table 3-2**. CV was measured with 0.1M [n-Bu4N]+[PF6]- in acetonitrile solution as electrolyte and Ag/AgCl as the reference electrode, at a scan rate of 100 mVs^{-1}. The E_{HOMO} of the polymer corresponds to the onset oxidation potential with respect to ferrocene/ferrocenium (Fc/Fc^{+}) Thus, according to the CV spectra, the E_{HOMO} levels for PIDMT, PIDBT and PIDBDT are estimated to be -5.75, -5.42, -5.61 eV, respectively, which is similar to the gaussian computer simulation that predicted that PIDBT would have the highest E_{HOMO}. The polymer films were also annealed at 220 °C and measured for their optical and electrochemical properties and found that after annealing, the E_{HOMO} was slightly raised. The optical bandgaps were also calculated and revealed that PIDMT showed the greatest difference.

(a)

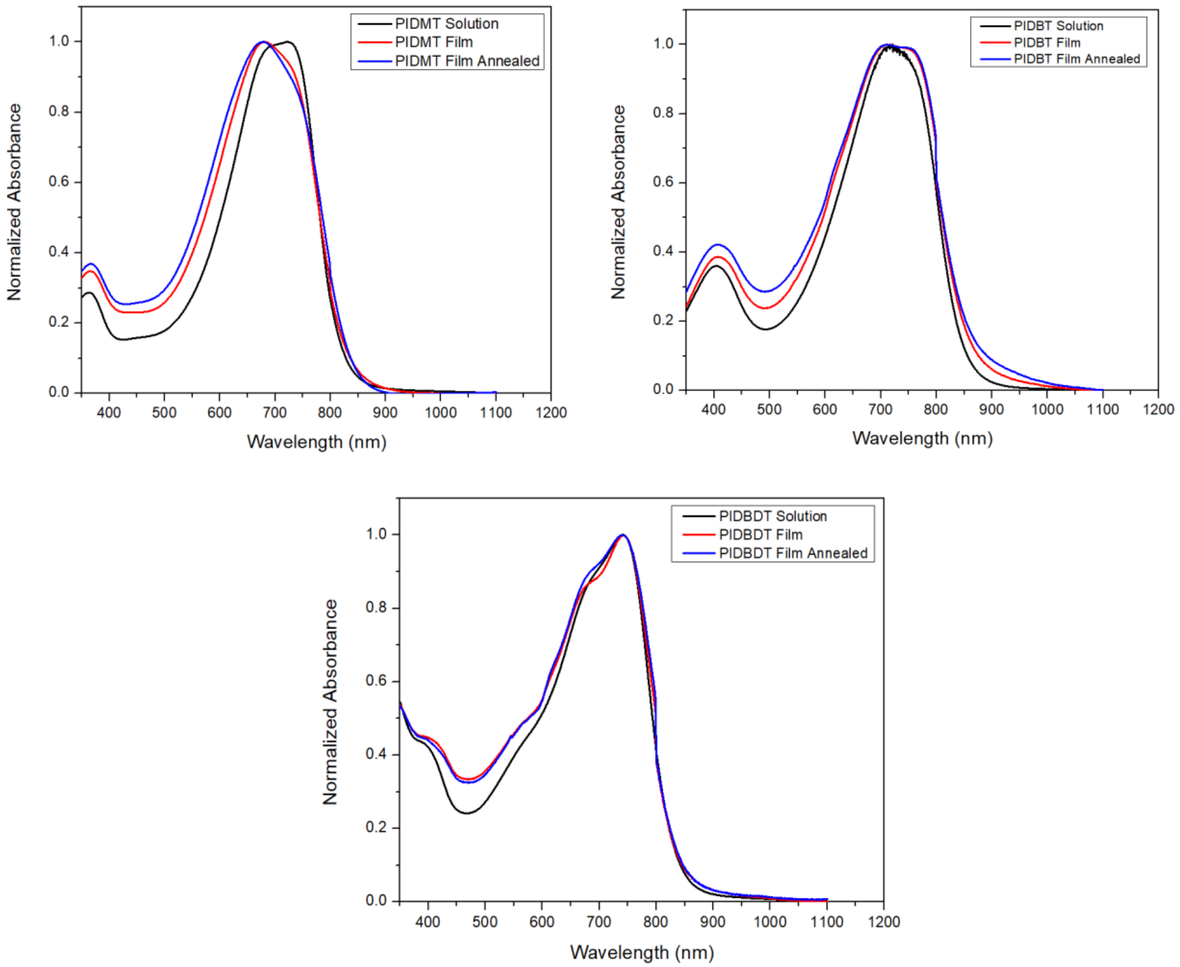

PIDMT Solution
PIDMT Film
PIDMT Film Annealed
Normalized Absorbance
0.0
0.2
0.4
0.6
0.8
1.0
400
500
600
700
800
900
1000
1100
1200
Wavelength (nm)
PIDBT Solution
PIDBT Film
PIDBT Film Annealed
Normalized Absorbance
Wavelength (nm)
PIDBDT Solution
PIDBDT Film
PIDBDT Film Annealed
Normalized Absorbance
Wavelength (nm)

(b)

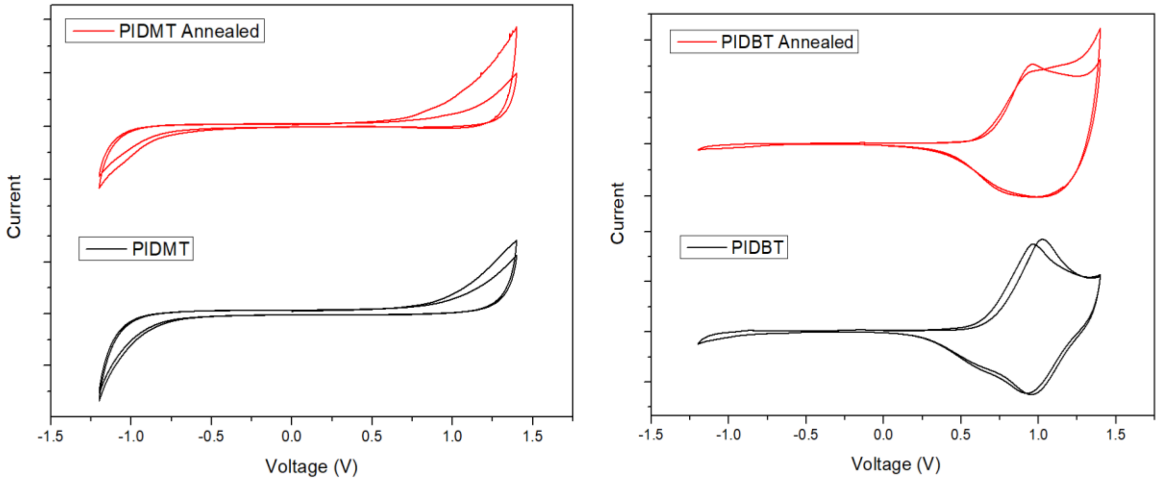

PIDMT Annealed
PIDMT
Current
-1.5
-1.0
-0.5
0.0
0.5
1.0
1.5
Voltage (V)
PIDBT Annealed
PIDBT
Current
Voltage (V)

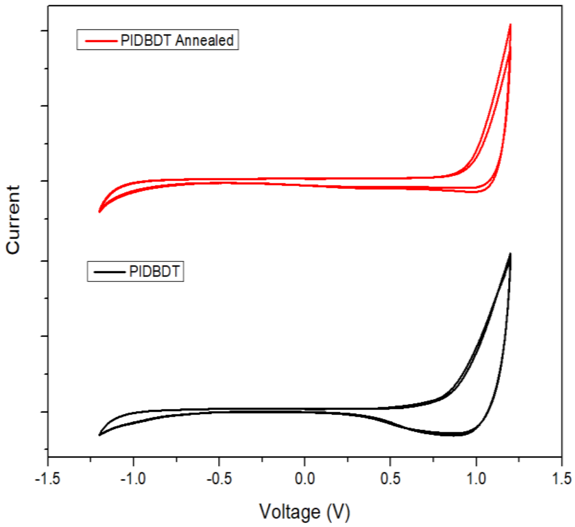

Figure 3-6 Optical and electrochemical properties of PIDMT, PIDBT and PIDBDT **(a)** Normalized UV-vis spectra of PID polymers solution and thin films at room temperature and at 220 °C (**b)** Cyclic voltammetry profiles with 0.1M [n-$Bu_4N]^+[PF6]^-$ in acetonitrile solution as electrolyte at a scan rate of $0.1Vs^{-1}$

Table 3-2 Optical and electrochemical properties of PIDMT, PIDBT and PIDBDT

Polymer	λ_{max} (nm)		λ_{onset} (nm)		E_{HOMO} (eV)	E_{LUMO} (eV)	E_g Gap (eV)
	Sol.	Film	Sol.	Film	Film	Film	Film
PIDMT	721	681	822	824	-5.75	-4.25	1.50
PIDMT N	---	678	---	825	-5.74	-4.30	1.44
PIDBT	721	716	848	867	-5.42	-4.01	1.41
PIDBT N	---	711	---	868	-5.40	-4.12	1.28
PIDBDT	741	743	835	837	-5.61	-4.13	1.48
PIDBDT N	---	743	---	837	-5.60	-4.16	1.44

3.4 Characterization of Isoindigo Based Polymers

3.4.1 Physical Properties (GPC, TGA, and DSC)

High-temperature gel permeation chromatography (HT-GPC) was performed at 150 °C with 1,2,4-trichlorobenzene as the eluent and polystyrene as the standard to determine the molecular weight of PIDMT, PIDBT and PIDBDT. The number average molecular weight (M_n) of PIDMT, PIDBT and PIDBDT are 42.8 kDa, 23.2 kDa, and 26.0 kDa, respectively. The weight average molecular weight (M_w) was determined to be 121 kDa, 110 kDa and 65.1 kDa, respectively and the polydispersity index was calculated to be 2.82, 4.77 and 2.50, respectively.

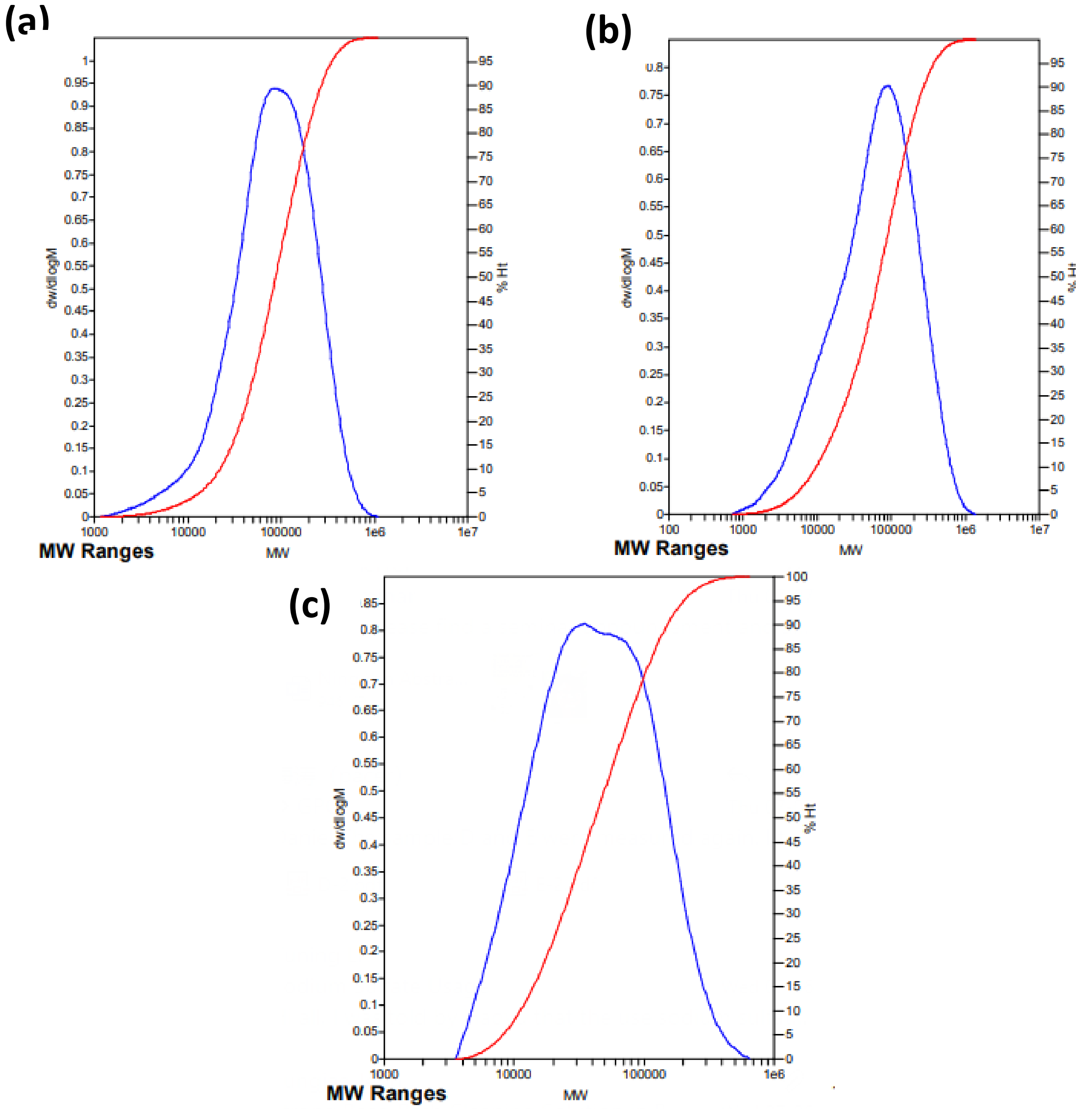

Figure 3-7 HT-GPC molecular weight distribution of **(a)** PIDMT **(b)** PIDBT **(c)** PIDBDT

Table 3-3 Molecular weight and polydispersity index of PIDMT, PIDBT

Polymer	M_n (kDa)	M_w (kDa)	PDI
PIDMT	**42.8**	**121**	**2.82**
PIDBT	**23.2**	**110**	**4.77**
PIDBDT	**26.0**	**65.1**	**2.50**

Thermalgravimetric analysis (TGA) and differential scanning calorimetry (DSC) were carried out to study the PID polymer's thermal stability as well as the thermolability property of the carbamate side chain. The polymers were heated in air at a heating rate of 10 °C min^{-1} from 25 °C, and held at 250 °C for 20 min, then heated at 10 °C min^{-1} until 600 °C. As shown in **Figure 3-8 (a)**, polymers PIDMT, PIDBT and PIDBDT lost 9.96 %, 8.59 % and 1.55% weight, respectively, at 250 °C which is much lower than the anticipated loss of 37.4%, 42.2% and 58.2% respectively, to thermally cleave the entire carbamate chain. This phenomenon is due to the presence of the long-branched carbon 20 chain on the PID polymers giving it a higher melting temperature and enhancing its ability to store more thermal energy per unit mass. Furthermore, the first thermal decomposition for PIDMT and PIDBT occurred at ~320 °C, and 349 °C for PIDBDT whereas the second thermal decomposition occurred at ~360°C. Evidently, the PID polymers show excellent thermal stability, making them an ideal candidate for OTFTs that require a high-temperature tolerance. The increased thermal stability of the PIDBDT polymer is due to the increased molar ratio of the BDT donor which is more conjugated and rigid than the isoindigo acceptor. Moreover, the differential scanning calorimetry thermograms in **Figure 3-8 (b)** revealed no obvious glass transitions, meaning there were no endothermic and exothermic transitions.

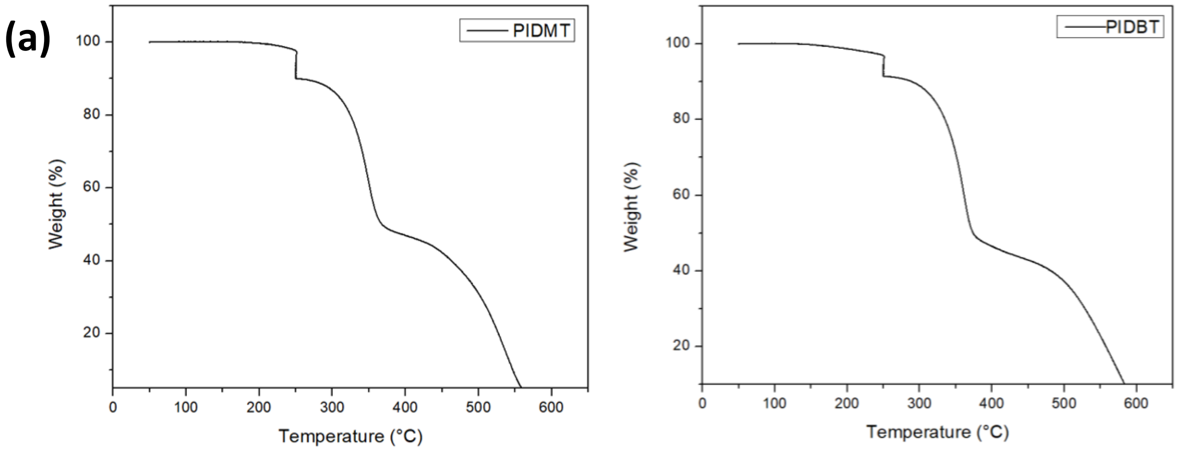

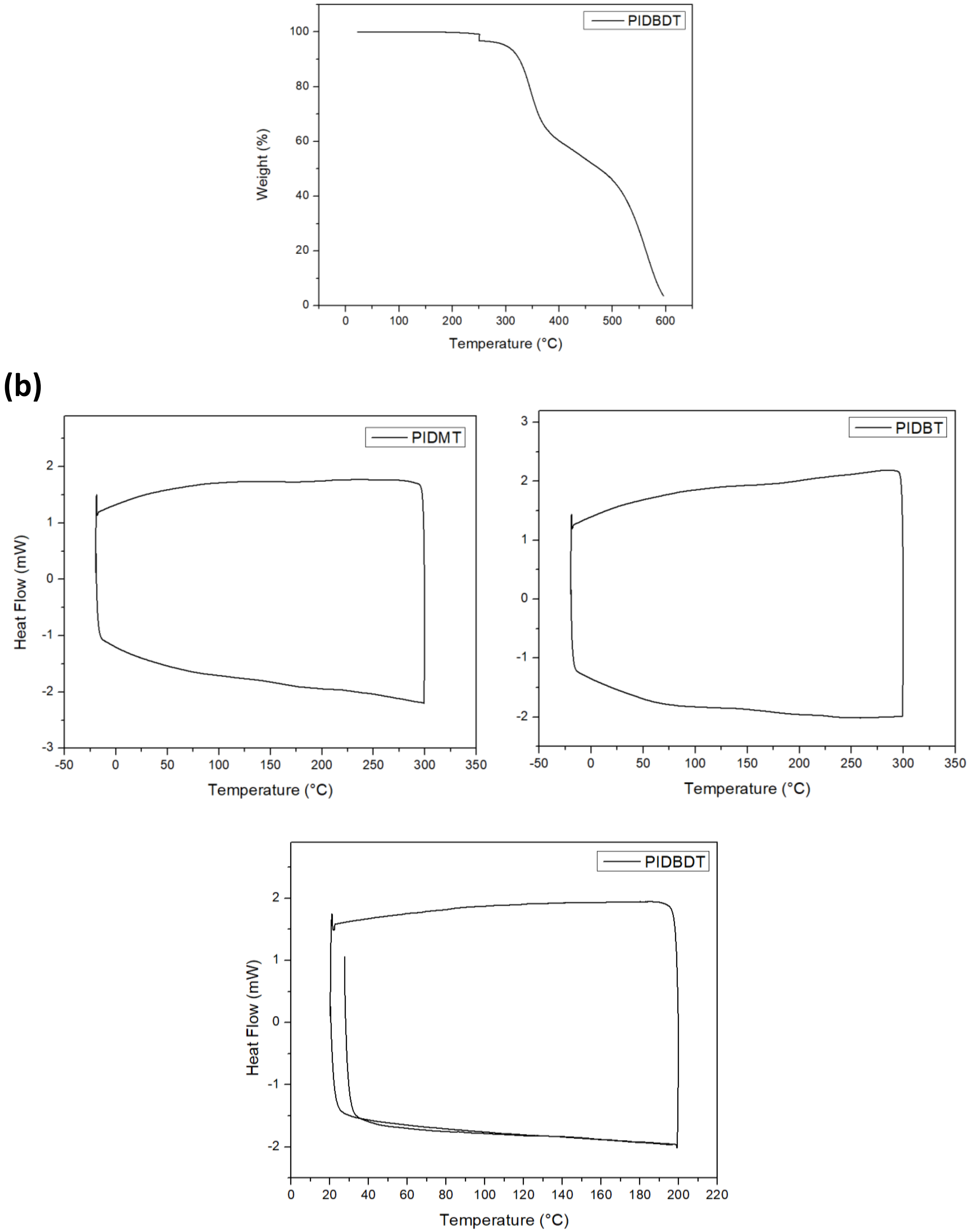

Figure 3-8 (a) TGA curve **(b)** DSC curve for PIDMT, PIDBT and PIDBDT

3.5 Solvent Resistance Test

One of the main goals of adding the thermo-cleavable carbamate chain is to make the polymers solvent resistant. This is to prevent the polymer backbone from oxidation that may occur at higher temperatures. Thus, the solvent resistance was evaluated for the PID polymers at different annealing temperatures; RT, 150°C and 250°C and at different annealing times. The polymers were processed in chloroform solution and spin-coated (50-60 nm thickness) on a glass substrate, then annealed at different temperatures described above with different annealing times. The glass substrates were then subjected to different solvents starting from the most polar solvent to the processable solvents, then were characterized using UV-vis spectroscopy. The percentages shown below denote the amount of polymer remaining on the glass substrate after soaking them in various solvents. The following information can be extracted from the UV-vis spectra; Polymers PIDMT, PIDBT and PIDBDT showed strong resistance at all temperatures towards acetonitrile and acetone but showed no resistance towards toluene and chloroform at room temperature. At 150 °C the polymers were annealed for 30 minutes and ~1 hour, respectively. Polymer PIDMT showed full resistance towards toluene at 30 minutes and 1 hour but showed partial resistance of 36% and 88% towards chloroform. Polymer PIDBT also showed full resistance towards toluene at 30 minutes and 1 hour and similarly showed partial resistance towards chloroform of 40% and 92%, respectively. Polymer PIDBDT showed partial resistance towards toluene of 33 % and 55 % and showed zero resistance towards chloroform when annealing at 150°C for 30 minutes, but became partially resistant when annealed for 1 hour. Furthermore, all of the polymers showed full solvent resistance when annealed at 250 °C for 30 minutes. A summary of the quantitative results for solvent resistance can be found in **Tables 3-4, 3-5, and 3-6** for PIDMT, PIDBT and PIDBDT, respectively.

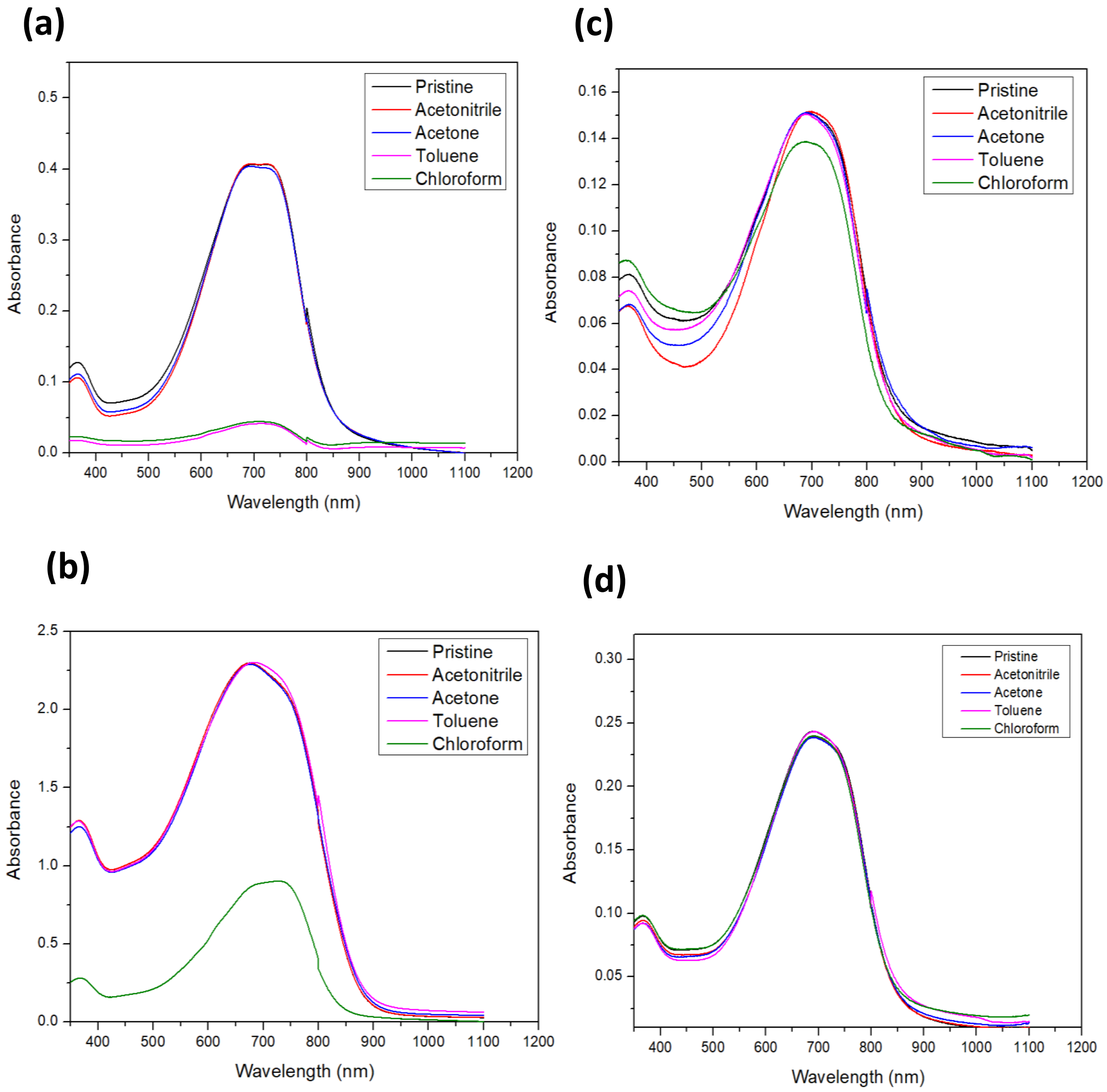

Figure 3-9 Solvent Resistance Test for polymer PIDMT through UV-vis characterization at **(a)** RT **(b)** 150 °C for 30 min **(c)** 150 °C for 60 min **(d)** 250°C for 30 min

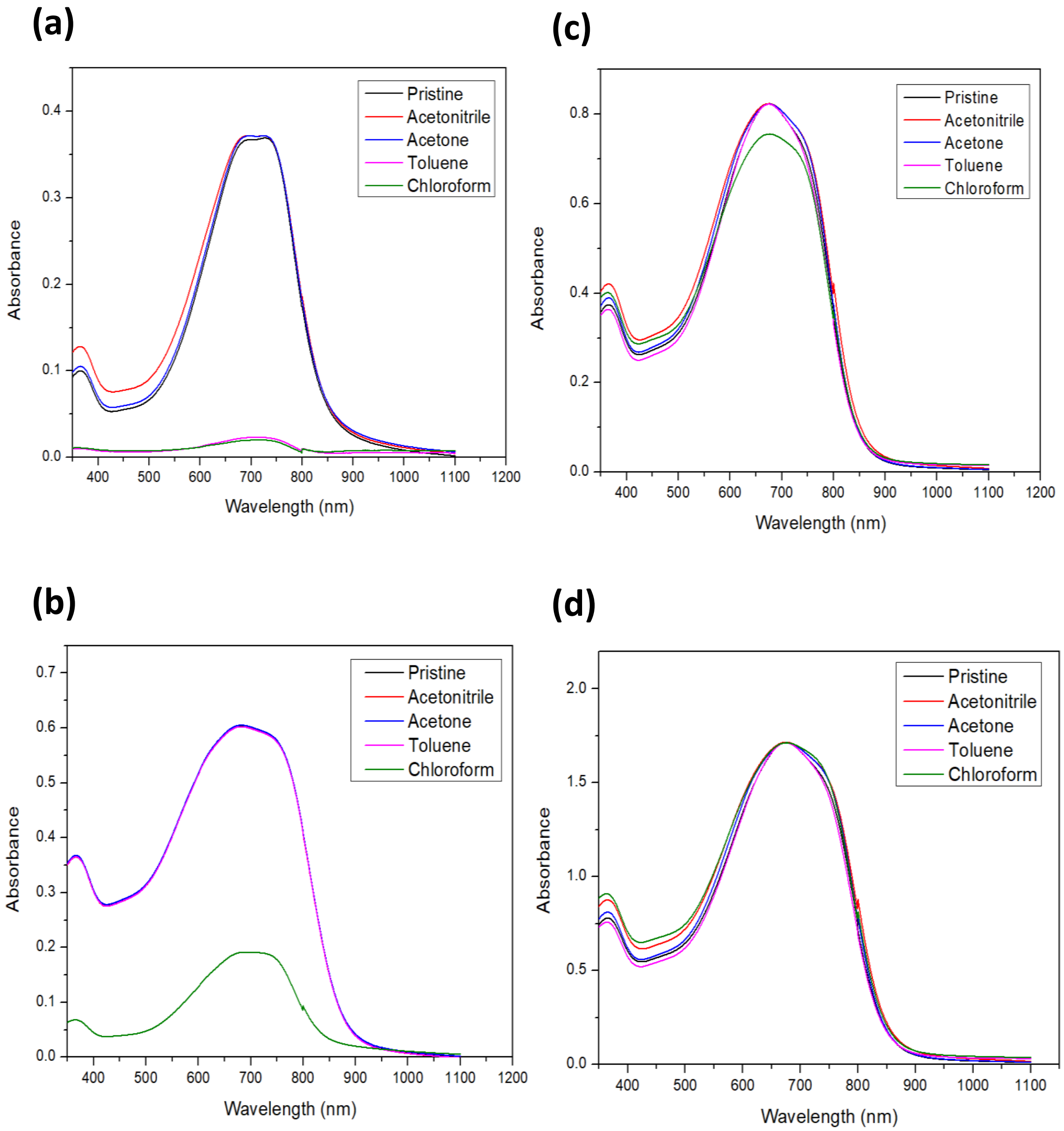

Figure 3-10 Solvent Resistance Test for polymer PIDBT through UV-vis characterization at **(a)** RT **(b)** 150 °C for 30 min **(c)** 150 °C for 60 min **(d)** 250°C for 30 min

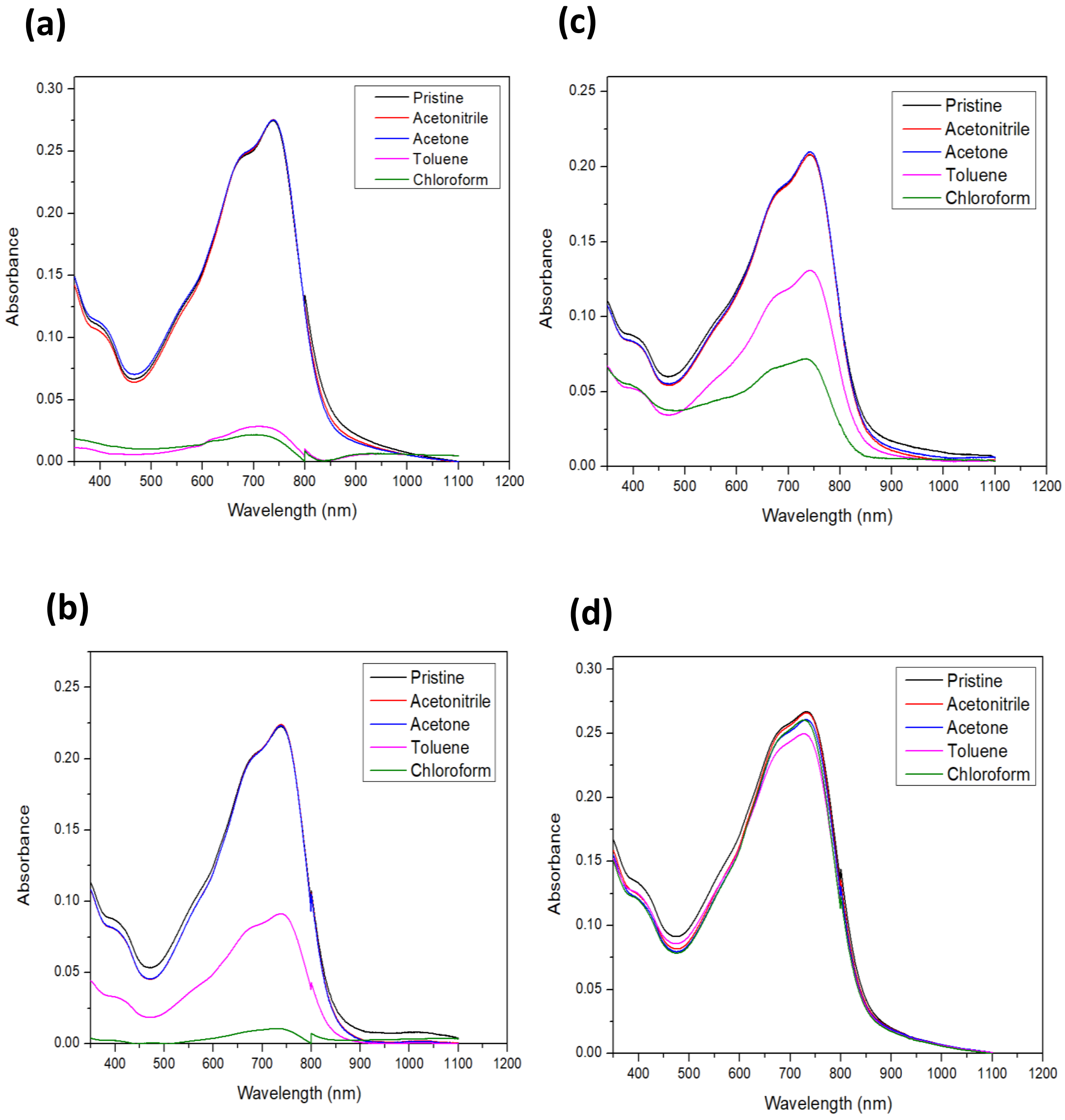

Figure 3-11 Solvent Resistance Test for polymer PIDBDT through UV-vis characterization at **(a)** RT **(b)** 150 °C for 30 min **(c)** 150 °C for 60 min **(d)** 250°C for 30 min

Table 3-4 Quantitative Results from Solvent Resistant Test for PIDMT

Polymer PIDMT					
Temperature	**Time Annealed**	**Acetonitrile**	**Acetone**	**Toluene**	**Chloroform**
Room Temp	**N/A**	**100 %**	**100 %**	**0%**	**0%**
150 °C	**30 Min**	**100 %**	**100 %**	**100%**	**36%**
150 °C	**70 Min**	**100 %**	**100 %**	**100%**	**88%**
250 °C	**30 Min**	**100 %**	**100 %**	**100 %**	**100 %**

Table 3-5 Quantitative Results from Solvent Resistant Test for PIDBT

Polymer PIDBT					
Temperature	**Time Annealed**	**Acetonitrile**	**Acetone**	**Toluene**	**Chloroform**
Room Temp	**N/A**	**100 %**	**100 %**	**0%**	**0%**
150 °C	**30 Min**	**100 %**	**100 %**	**100%**	**40%**
150 °C	**70 Min**	**100 %**	**100 %**	**100%**	**92%**
250 °C	**30 Min**	**100 %**	**100 %**	**100 %**	**100 %**

Table 3-6 Quantitative Results from Solvent Resistant Test for PIDBDT

Polymer PIDBDT					
Temperature	**Time Annealed**	**Acetonitrile**	**Acetone**	**Toluene**	**Chloroform**
Room Temp	**N/A**	**100 %**	**100 %**	**0%**	**0%**
150 °C	**30 Min**	**100 %**	**100 %**	**33%**	**0%**
150 °C	**70 Min**	**100 %**	**100 %**	**55%**	**28%**
250 °C	**30 Min**	**100 %**	**100 %**	**100 %**	**100 %**

** Quantitative results shown above denote the amount of polymer remaining on the glass substrate after soaking them in various solvents**

3.6 OFET Performance

The OFET devices are configured using a bottom gate bottom contact (BGBC) layout. The fabrication of the devices utilized Si/SiO_2 substrates with patterned gold contacts through photolithographic techniques. The PID polymers (5mg/ml) were processed in chloroform and spin-coated on the silicon substrate at 3000 RPM for 90 seconds. All the polymers were evaluated at different annealing temperatures ranging from RT to 250 ºC.

All the polymers exhibited both n-type and p-type performance indicating ambipolar performance, which is useful towards applications such as gas sensors. The mobilities typically range from 10^{-2} to 10^{-4} $cm^2\ V^{-1}s^{-1}$ with p-type being the dominant operation. The highest mobility attained was 0.01 $cm^2\ V^{-1}s^{-1}$ by PIDBT while the other polymers attained much lower mobilities. The threshold voltages are quite large, which may be caused by charge trapping. The current on/off for all polymers ranges from 10 to 10^4 with PIDBT having the best current on/off. The typical trend observed for the PID polymers is the substantial deterioration of mobility after 100 ºC which could be attributed to the polymer chain undergoing disordered packing. This may seem that the material is going through severe decomposition at high temperatures resulting in poor mobility, but the TGA data confirms that polymers have excellent thermal stability. This result is similar to Satej et al’s research in which they used alkyl-substituted isoindigo polymers to be used in OTFTs. [76] Similarly, their PID polymers reported excellent thermal stability up to 300 ºC. However, the mobility of the alkyl PIDBT polymer was significantly less (3.7 x 10^{-4} $cm^2V^{-1}s^{-1}$ at 150 ºC) for p-type operation. [76] At temperatures beyond 150 °C, the mobility severely deteriorated due to the thin film morphology. The AFM data revealed that the fibrous structures of the alkylated PIDBT did not possess any interconnected networks. [76]

Moreover, when annealing at 250 ºC to cleave the carbamate chain, the performance also significantly reduced. One interesting aspect to note is polymer PIDMT had n-type performance as the dominant mode whereas both PIDBT and PIDBDT has p-type as the dominant mode. Although these mobilities are subpar, the application of these thin film transistors can be utilized for other sensor applications and prove a better candidate for OTFTs than alkyl-substituted isoindigo polymers.

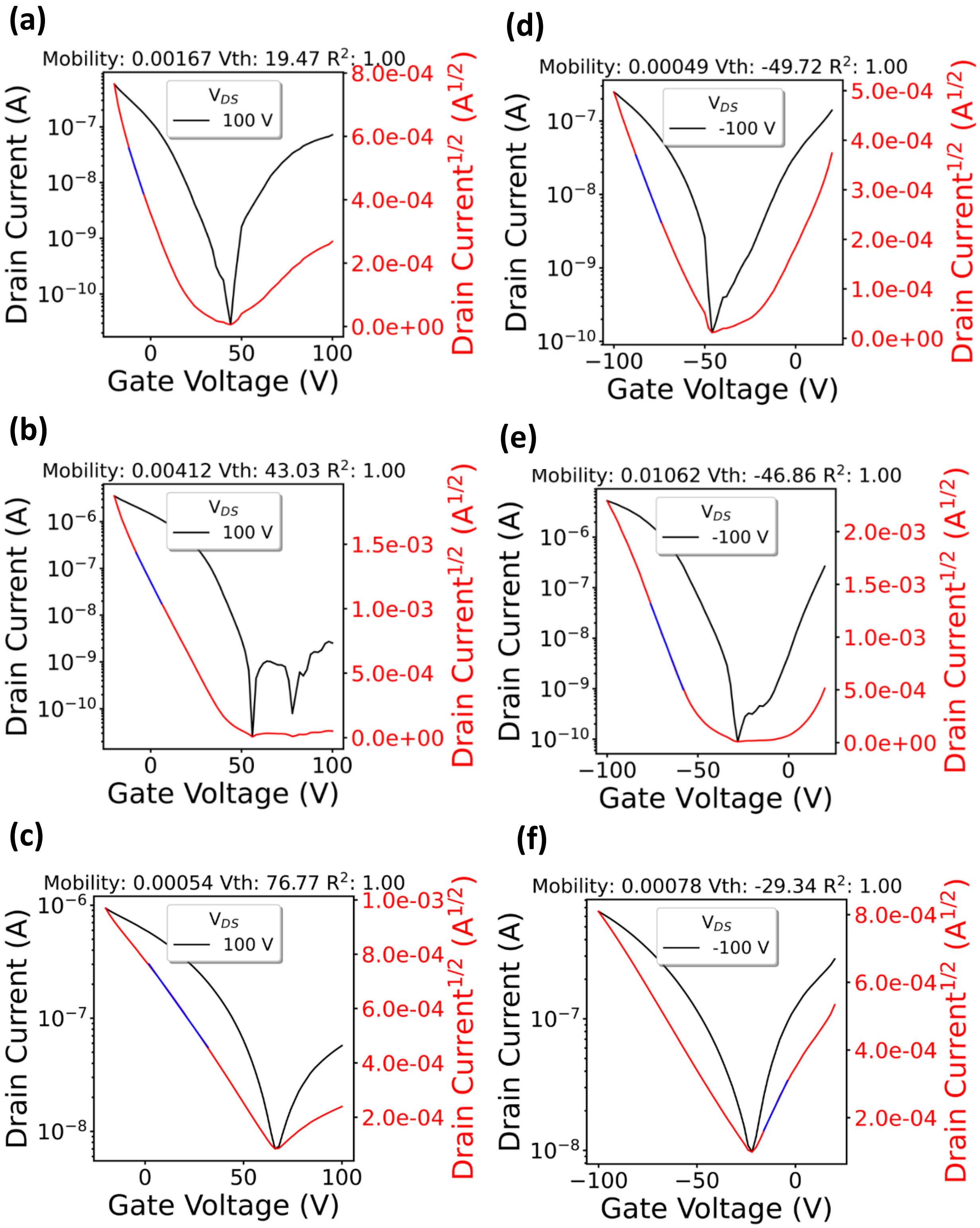

Figure 3-12 (a-c) N-Type transfer curves for PIDMT, PIDBT and PIDBDT, respectively **(d-f)** P-type transfer curve for PIDMT, PIDBT and PIDBDT, respectively, at RT, 50 ºC and 100 ºC

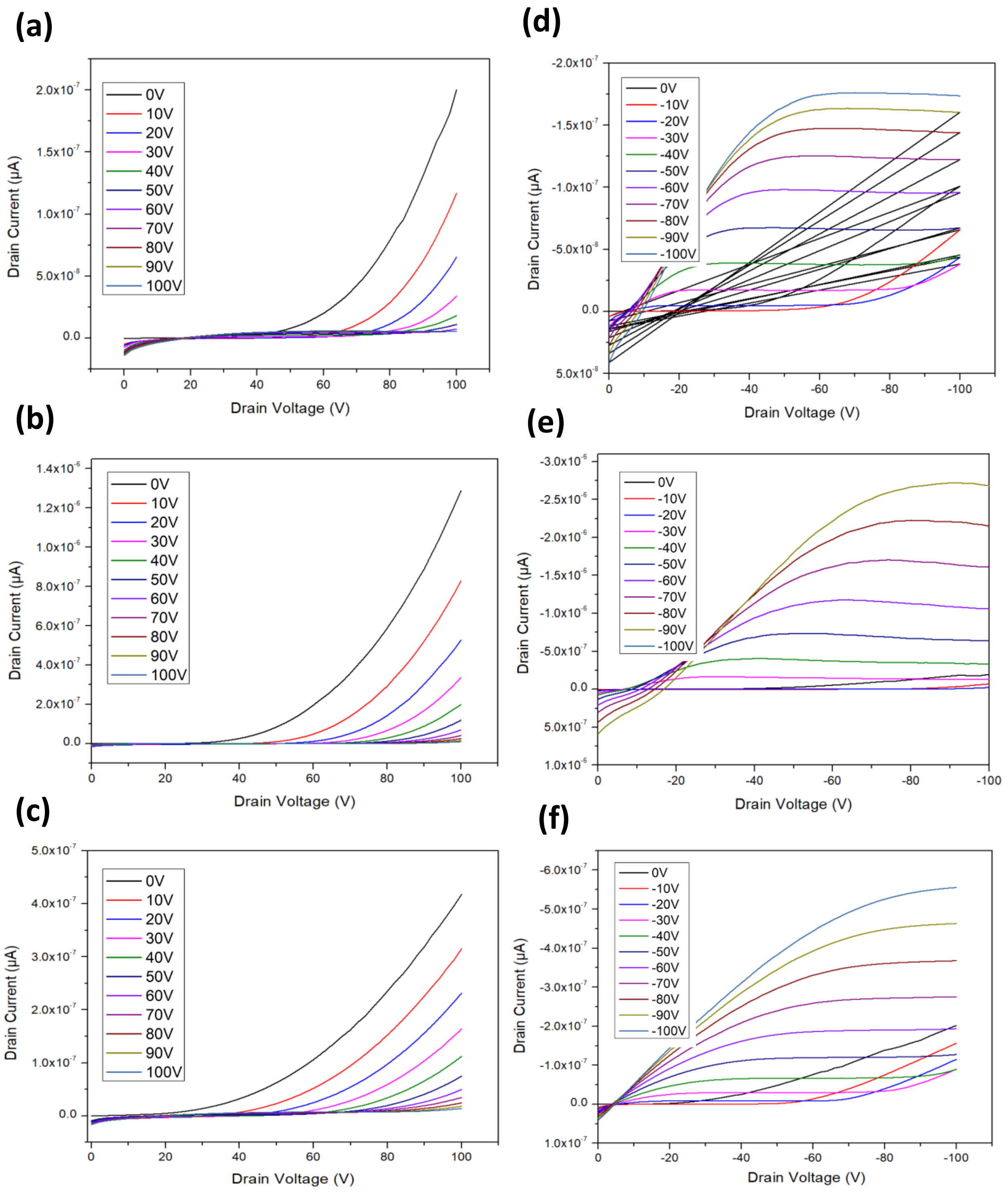

Figure 3-13 (a-c) N-Type output curves for PIDMT, PIDBT and PIDBDT, respectively **(d-f)** P-type output curve for PIDMT, PIDBT and PIDBDT at 50°C, RT,100°C, respectively

Table 3-7 OFET Performance Parameters for PID Polymers

Material		Mobility $(\mathrm{cm^2V^{-1}s^{-1}})$		$I_{On/Off}$		V_T, V	
	Temperature (°C)	P-Type	N-Type	P-Type	N-Type	P-Type	N-Type
PIDMT	RT	3.3 x10^{-4}	1.7 x10^{-3}	>10^3	>10^3	-47.96	13.56
	50	4.8 x10^{-4}	1.2 x10^{-3}	>10^3	>10^3	-49.74	24.02
	100	4.5 x10^{-4}	1.0 x10^{-3}	>10^3	>10^4	-47.54	29.08
	150	4.1 x10^{-4}	1.4 x10^{-3}	>10^3	>10^4	-40.64	29.16
	200	3.2 x10^{-4}	1.2 x10^{-3}	>10^2	>10^3	-40.34	38.60
	250	2.7 x10^{-4}	8.8 x10^{-4}	>10^3	>10^2	-42.20	51.78
PIDBT	RT	7.5 x10^{-3}	2.8 x10^{-3}	>10^4	>10^2	-31.04	41.89
	50	1.0 x10^{-2}	4.1 x10^{-3}	>10^4	>10^2	-46.96	43.02
	100	6.4 x10^{-3}	6.4 x10^{-4}	>10^3	>10^2	-44.30	50.11
	150	3.7 x10^{-3}	4.4 x10^{-3}	>10^3	>10^2	-29.04	49.51
	200	5.1 x10^{-4}	3.5 x10^{-3}	>10^3	>10^2	-52.51	48.60
	250	1.2 x10^{-4}	7.8 x10^{-4}	>10^2	>10^1	-39.02	46.86
PIDBDT	RT	1.7 x10^{-4}	3.5 x10^{-4}	>10^2	>10^1	-14.76	77.88
	50	5.2 x10^{-4}	5.4 x10^{-4}	>10^2	>10^1	-16.30	76.96
	100	7.1 x10^{-4}	5.3 x10^{-4}	>10^2	>10^1	-29.34	76.77
	150	4.3 x10^{-4}	3.1 x10^{-4}	>10^2	>10^1	-27.12	73.91
	200	3.4 x10^{-4}	2.8 x10^{-4}	>10^1	>10^1	-27.55	70.20
	250	2.0 x10^{-4}	1.0 x10^{-4}	>10^1	>10^1	-22.90	72.35

3.7 Morphology and Crystallinity of PID Polymers

Two-dimensional grazing-incidence X-ray diffraction (2D-GIXD) and AFM were used to characterize the polymer neat films on silicon substrates with different annealing temperatures. The PID polymers displayed no noticeable peaks in both the OOP and IP direction at different annealing temperatures, which suggests that all the polymers are amorphous and packed in a disordered manner. Further analysis done by AFM shows poor crystallinity with tiny crystalline domain size, thus impeding the effective π-π stacking resulting in poor mobility. The surface morphology of PIDMT and PIDBDT exhibits extremely low surface roughness, with average RMS values of 1.20 nm and 1.76 nm, respectively, according to the AFM images. Polymer PIDBT, which showed the best performance, had the roughest surface with an average RMS value of 2.73 nm. Furthermore, the surface roughness shows a declining trend for all PID polymers, suggesting that at higher temperatures there is more disordered packing. In conclusion, the interconnected domains and increased surface roughness allude to a more significant impact on charge transport in OFETs.

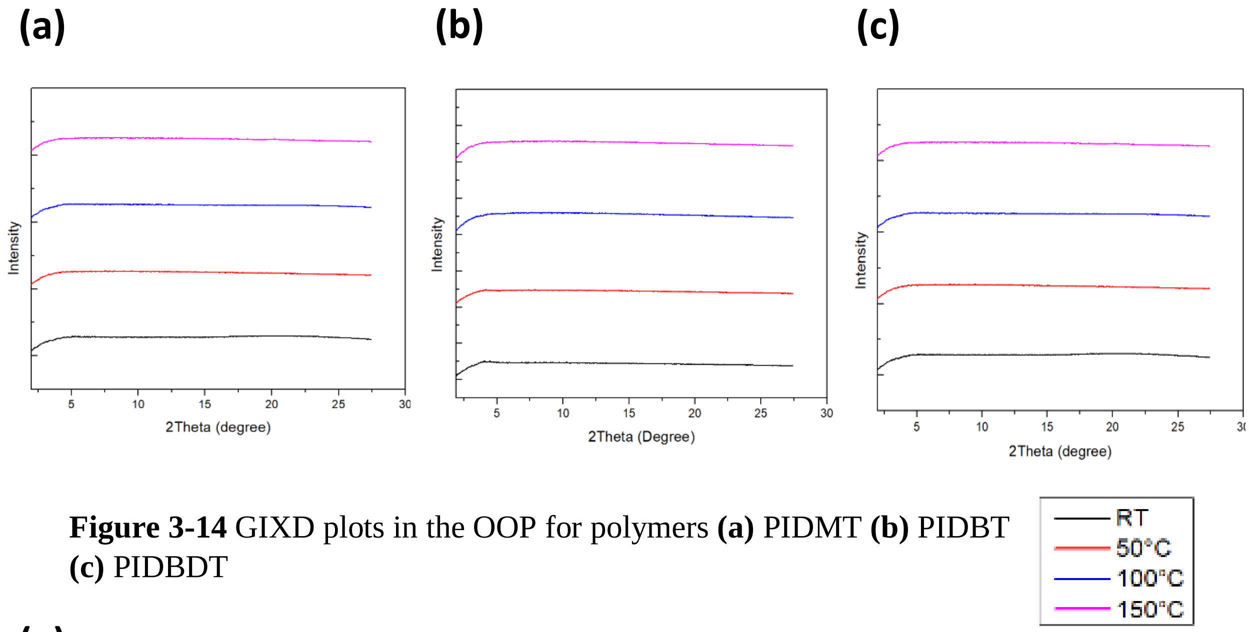

Figure 3-14 GIXD plots in the OOP for polymers **(a)** PIDMT **(b)** PIDBT **(c)** PIDBDT

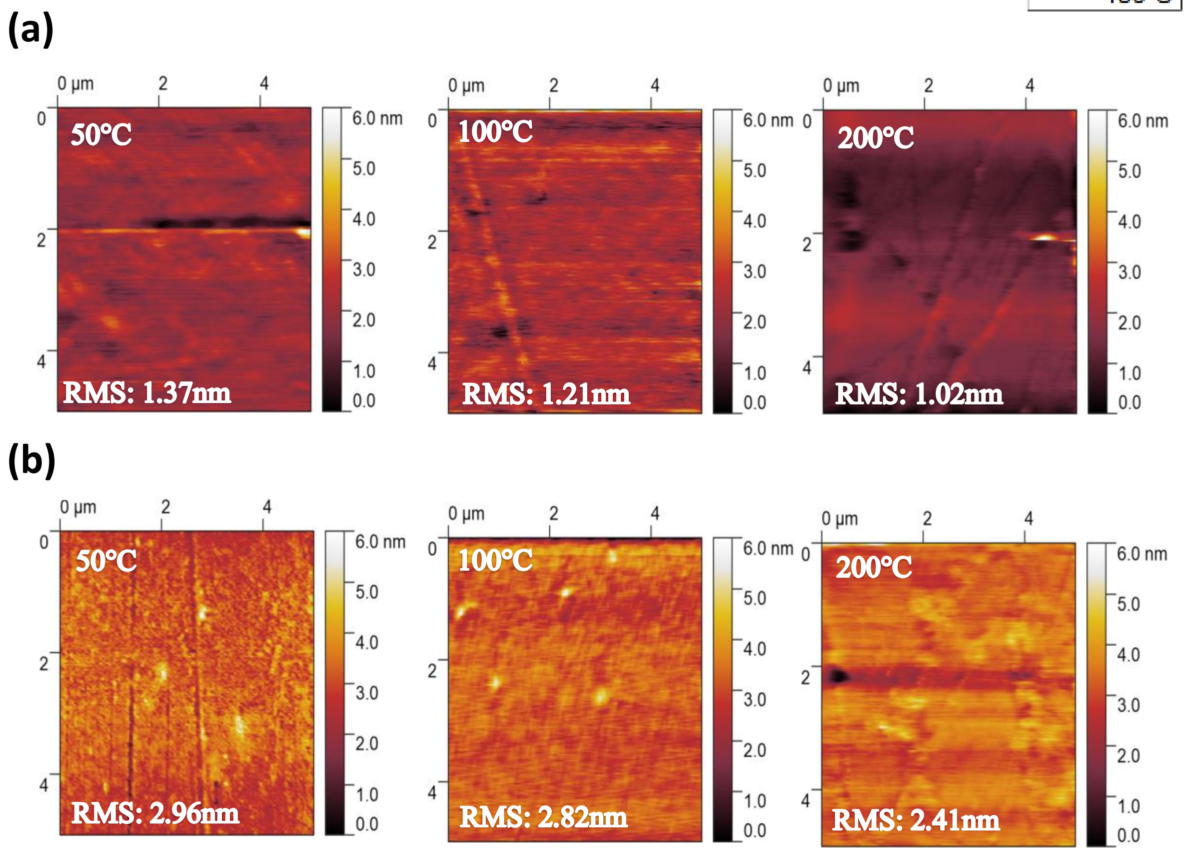

(c)

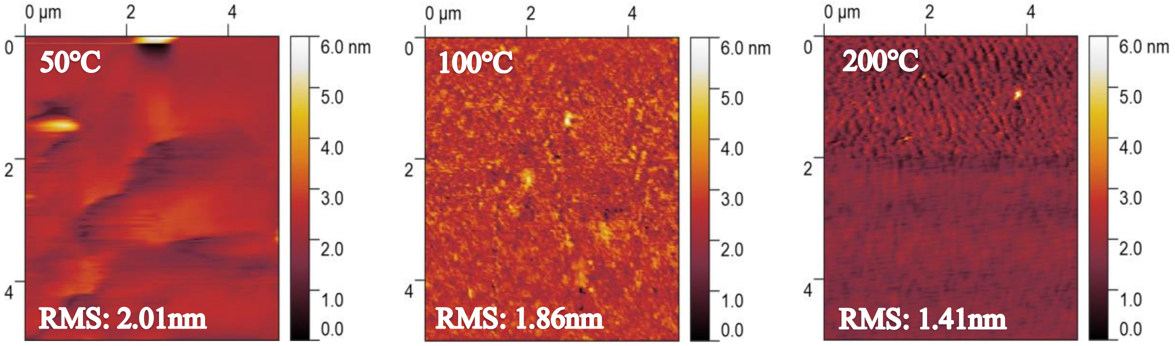

Figure 3-15 AFM height images (5μm x 5μm) of neat films at different annealing temperatures **(a)** PIDMT **(b)** PIDBT **(c)** PIDBDT

3.8 Summary and Future Direction

In conclusion, three novel donor-acceptor polymers PIDMT, PIDBT and PIDBDT were synthesized based on the isoindigo backbone unit with long carbamate side chains substituted on the hetero-nitrogen ring. The gaussian computation elucidations exhibited good π-π stacking vital for good carrier transfer ability along the polymer. The polymers were evaluated based on their transfer characteristics, mobility, and solvent resistance. With regards to solvent resistance, all of the polymers exhibited full resistance towards processing solvents such as chloroform and toluene when annealed at 250 ºC. But showed partial solvent resistance when annealed at 150° C. Polymer PIDBDT showed little to no solvent resistance at 150°C due to having long ethyl hexyl alkyl chains on the BDT unit which cannot be thermally cleaved and also having a higher weight ratio of BDT to PID. Thus, further proving that the substitution of the carbamate chain yields excellent solvent resistance. In terms of performance, the PID polymers displayed ambipolar characteristics with p-type mode being the dominant operation. The best mobility performance for PIDMT, PIDBT and PIDBDT are 0.004, 0.01 and 0.007 $cm^2V^{-1}s^{-1}$, respectively, for p-type and 0.001, 0.004, 0.005 $cm^2V^{-1}s^{-1}$, respectively for n-type with PIDBT being dominant for both modes. After removing the carbamate chain, the polymers displayed unfavorable mobilities. The low mobilities of the PID polymers can be explained through the XRD and AFM analysis which reveals that all of the polymers are amorphous with small grains that are not well connected. Although the amorphous property of the PID polymers inhibits their mobility, for OTFT applications concerning gas sensors, this could be a great venture as the polymer sensing layer can facilitate the diffusion of the analyte molecules in the channel layer of OFETs, thereby increasing sensitivity.

When comparing the alkyl version of the PID polymers (conducted by Satej et al)[76] to the carbamate version, the thermal stability is similar, as both versions exhibit stability of up to 300 °C. However, the mobility of the carbamate version improved by 250% when comparing to the PIDBT version. For future improvements, a small molecule consisting of the isoindigo backbone unit, paired with an electro-donating 3,4-ethylenedioxythiophene donor unit can potentially enhance the degree of crystallinity, resulting in higher mobility. Other future improvements include acid removal of the carbamate chain without the use of high thermal treatment. This prevents the polymer from losing its performance while maintaining the solvent resistance aspect. Further improvements involve different substituents, such as the addition of halogenic atoms, to achieve higher mobility due to the extension of the conjugation by the participation of the atoms in the LUMO energy wave functions of the polymers. This could prove useful towards semiconductors and other chemical sensor applications.

3.9 Synthesis Procedures

Synthesis of 2-octyldodecyl carbonochloridate, [1]

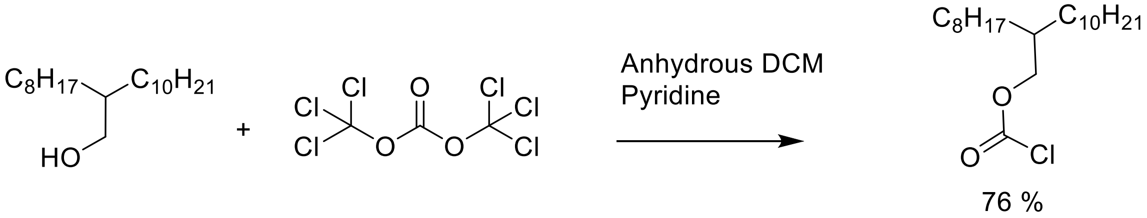

To a 500 mL two-neck round bottom flask, 2-octyl1-dodecanol (11.90 mL, 33.4 mmol) was added. One neck of the flask was fitted with a condenser and the other neck was stopped with a rubber septum. The flask was then vacuumed and purged for three times. Dichloromethane (70mL) was added via syringe and was cooled to 0 °C with ice. Pyridine (3.11 mL, 35.0 mmol) was then added to the mixture via syringe dropwise resulting in a pink solution. After 15 minutes of stirring, triphosgene (3.98 g) was added through the rubber septum by removing the septum and quickly depositing the bulk solid with filter paper. The rubber septum was then replaced with a glass stopper. The resulting mixture was stirred at 0°C for 30 minutes. The mixture was extracted with hexane to filter out the pyridine salt formed in the reaction mixture. Column chromatography was performed with n-hexane as the eluent to afford the transparent product 2-octyldodecyl carbonochloridate. ^{1}H NMR (300 MHz, chloroform-d) δ 4.21 (d, 2H), 8.07 (s, 1H), 1.72 (s, 1H), 1.27 (d, 32H), 0.87 (t, 3H), (**76% yield**)

Synthesis of (E)-6,6'-Dibromo-[3,3'-biindolinylidene]-2,2'-dione, [2]

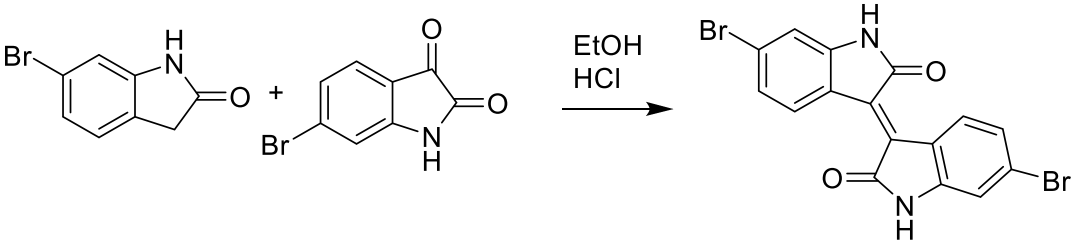

To a 100 mL two-neck round bottom flask, 6-bromoisosatin (1g, 4.6mmol) and 6-bromooxindole (1g, 4.6 mmol) were added. One neck of the flask was fitted with a condenser and the other neck was stoppered with a rubber septum. The flask was then vacuumed and purged for three times to allow nitrogen into the system. Next, 30 mL of glacial acetic acid was added via syringe through the rubber septum. The reaction was then heated to a constant temperature of 80 °C for 24 hours. Upon cooling the mixture to room temperature, the solid material was filtered with a Buchner funnel. Upon collection, the contents were thoroughly washed with water, ethanol and ethyl acetate three times then vacuumed to afford the pure red solid (E)-6,6'-Dibromo-[3,3'-biindolinylidene]-2,2'-dione. (1.95g, 95%).^{1}H NMR (300 MHz, dimethyl sulfoxide-d6) δ 11.11 (s, 2H), 8.07 (s, 2H), 9.03 (d, 2H), 7.22 (d, 2H), 7.03 (d, 2H), (**95% yield**)

Synthesis of bis(2-octyldodecyl) (E)-6,6'-dibromo-2,2'-dioxo-[3,3'-biindolinylidene]-1,1'-dicarboxylate, [3]

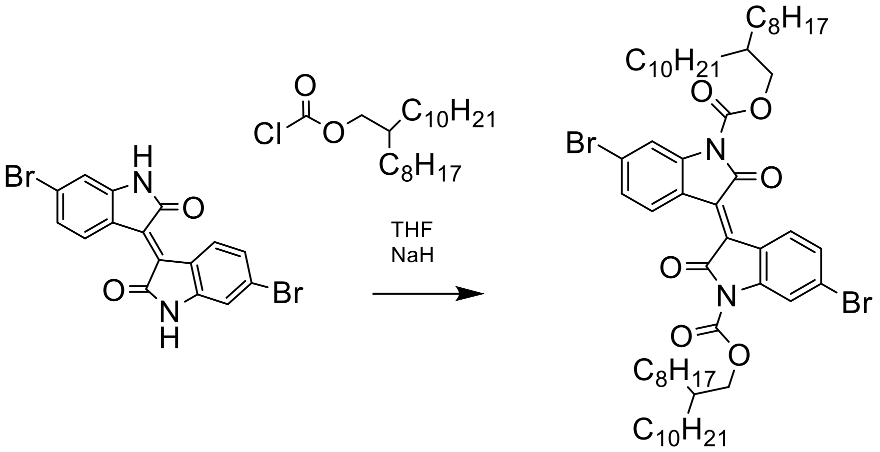

To a 100 mL two-neck round bottom flask, (E)-6,6'-Dibromo-[3,3'-biindolinylidene]-2,2'-dione was added to the flask (1 g, 2.3 mmol). Using a nitrogen glove bag, sodium hydride (0.28g, 11.5 mmol) was retrieved and added into the round bottom flask. The flask was fitted with a condenser and the other neck was stopped with a rubber septum. The flask was then vacuumed and purged for three times to allow nitrogen into the system. A solution of anhydrous tetrahydrafuran (45mL) was added via syringe and cooled to 0 °C with ice. 2-octyldodecyl carbonochloridate (1.6 g, 4.6 mmol) was added dropwise and the reaction mixture was left to react for 30 minutes. After 30 minutes, the reaction was extracted with ethyl acetate and washed with brine 3 times. The resulting mixture was dry packed with silica to initiate dry loading column chromatography. The column was eluted with 4:1 n-hexane ethyl acetate to afford a dark red solution. Rotary evaporation was used to evacuate all the remaining solvent and then placed into the fridge overnight. After 24 hours, the solid was rinsed with methanol and sonicated. The method was repeated three times to afford the pure red solid product bis(2-octyldodecyl) (E)-6,6'-dibromo-2,2'-dioxo-[3,3'-biindolinylidene]-1,1'-dicarboxylate. ^{1}H NMR (300 MHz, chloroform-d) δ 8.82 (d, 2H), 8.13 (s, 2H), 7.32 (d, 2H), 4.35 (d, 4H), 1.81 (s, 2H), 1.31(m,58H), 0.85(m,11H)(**70 % yield**)

Synthesis of bis(2-octyldodecyl) (E)-6-methyl-6'-(5-methylthiophen-2-yl)-2,2'-dioxo-[3,3'-biindolinylidene]-1,1'-dicarboxylate

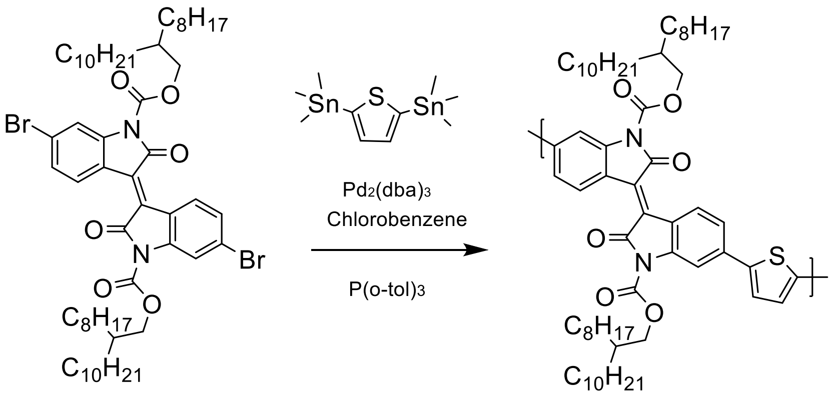

In a two-neck oven-dried round-bottom flask [3] (100 mg, 1.33 mmol) was added along with, 120 mg of 1,1′-[4,8-Bis[5-(2-ethylhexyl)-2-thienyl]benzo[1,2-b:4,5-b′]dithiophene-2,6-diyl]bis[1,1,1-trimethylstannane], 1.83 mg phosphine ligand tri(o-tolyl)phosphine (1.83 mg, 0.002 mmol). The flask was then fitted with a condenser and the other neck was stopped with a rubber septum. The flask was then vacuumed and purged for three times to allow argon into the system. Tris(dibenzylideneacetone)dipalladium(0), with a mass of 2.06 mg and a concentration of 0.002 mM, was first dissolved in 1 mL of degassed anhydrous chlorobenzene and then added to the reaction mixture. The reaction mixture was heated to 80 °C for 24 hours and was left to proceed unchecked for a full day before the temperature of the reaction was allowed to return to room temperature. The color of the reaction mixture changed from a dark maroon to a dark blue which is an indication that the reaction progressed well. The reaction mixture was then precipitated by methanol and purified via Soxhlet extraction method, in the following solvent sequence: methanol, acetone, hexane, and chloroform to afford polymer bis(2-octyldodecyl) (E)-6-methyl-6'-(5-methylthiophen-2-yl)-2,2'-dioxo-[3,3'-biindolinylidene]-1,1'-dicarboxylate. (**40% yield**)

Synthesis of bis(2-octyldodecyl) (E)-6-methyl-6'-(5'-methyl-[2,2'-bithiophen]-5-yl)-2,2'-dioxo-[3,3'-biindolinylidene]-1,1'-dicarboxylate

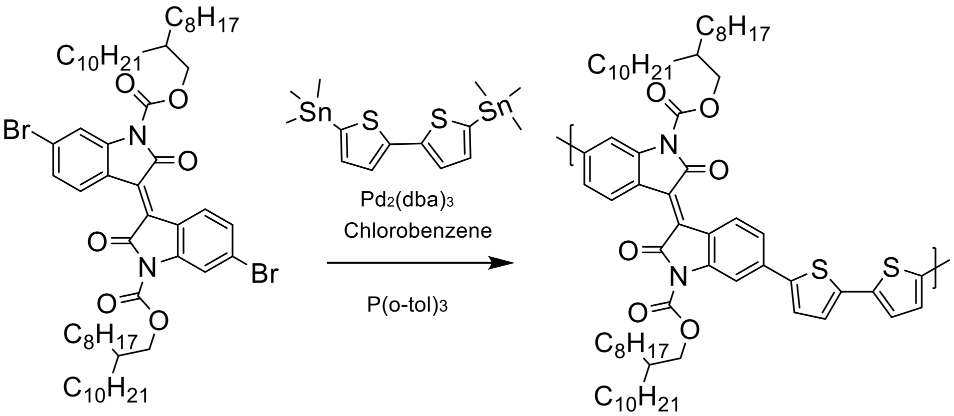

In a two-neck oven-dried round-bottom flask [3] (100 mg, 1.33 mmol) was added along with, 120 mg of 1,1′-[4,8-Bis[5-(2-ethylhexyl)-2-thienyl]benzo[1,2-b:4,5-b′]dithiophene-2,6-diyl]bis[1,1,1-trimethylstannane], 1.83 mg phosphine ligand tri(o-tolyl)phosphine (1.83 mg, 0.002 mmol. The flask was then fitted with a condenser and the other neck was stopped with a rubber septum. The flask was then vacuumed and purged for three times to allow argon into the system. Tris(dibenzylideneacetone)dipalladium(0), with a mass of 2.06 mg and a concentration of 0.002 mM, was first dissolved in 1 mL of degassed anhydrous chlorobenzene and then added to the reaction mixture. The reaction mixture was heated to 80°C for 24 hours and was left to proceed unchecked for a full day before the temperature of the reaction was allowed to return to room temperature. The color of the reaction mixture changed from a dark maroon to a dark blue which is an indication that the reaction progressed well. The reaction mixture was then precipitated by methanol and purified via Soxhlet extraction method, in the following solvent sequence: methanol, acetone, hexane, and chloroform. to afford polymer bis(2-octyldodecyl) (E)-6-methyl-6'-(5'-methyl-[2,2'-bithiophen]-5-yl)-2,2'-dioxo-[3,3'-biindolinylidene]-1,1'-dicarboxylate. (**30% yield**)

Synthesis of bis(2-octyldodecyl) (E)-6-(4,8-bis(5-(2-ethylhexyl)thiophen-2-yl)-6-methylbenzo[1,2-b:4,5-b']dithiophen-2-yl)-6'-methyl-2,2'-dioxo-[3,3'-biindolinylidene]-1,1'-dicarboxylate

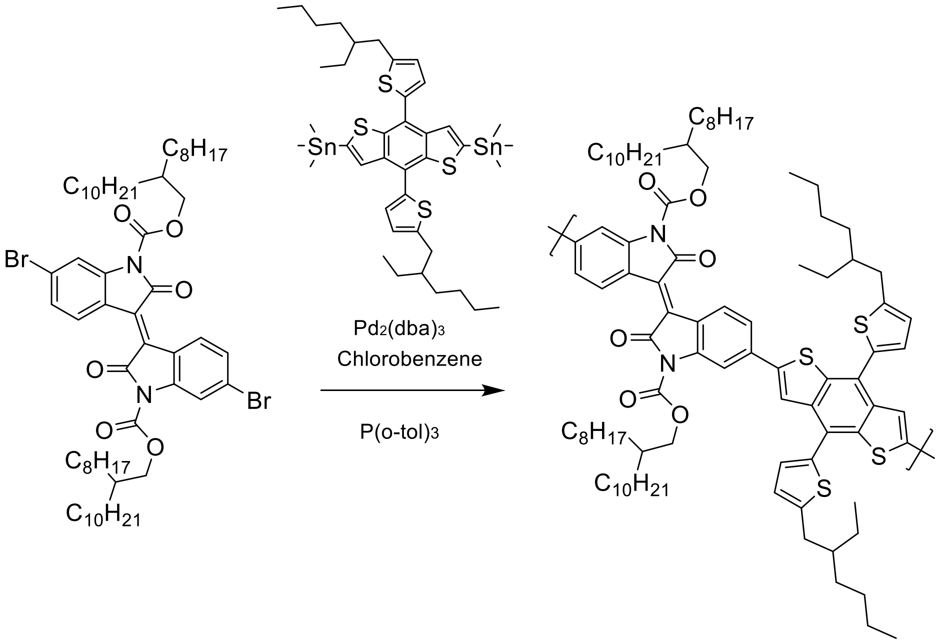

In a two-neck oven-dried round-bottom flask [3] (100 mg, 1.33 mmol) was added along with, 120 mg of 1,1′-[4,8-Bis[5-(2-ethylhexyl)-2-thienyl]benzo[1,2-b:4,5-b′]dithiophene-2,6-diyl]bis[1,1,1-trimethylstannane], 1.83 mg phosphine ligand tri(o-tolyl)phosphine (1.83 mg, 0.002 mmol. The flask was then fitted with a condenser and the other neck was stopped with a rubber septum. The flask was then vacuumed and purged for three times to allow argon into the system. Tris(dibenzylideneacetone)dipalladium(0), with a mass of 2.06 mg and a concentration of 0.002 mM, was first dissolved in 1 mL of degassed anhydrous chlorobenzene and then added to the reaction mixture. The reaction mixture was heated to 80 °C for 24 hours and was left to proceed unchecked for a full day before the temperature of the reaction was allowed to return to room temperature. The color of the reaction mixture changed from a dark maroon to a dark blue which is an indication that the reaction progressed well. The reaction mixture was then precipitated by methanol and purified via Soxhlet extraction method, in the following solvent sequence: methanol, acetone, hexane, and chloroform. to afford polymer bis(2-octyldodecyl) (E)-6-(4,8-bis(5-(2-ethylhexyl)thiophen-2-yl)-6-methylbenzo[1,2-b:4,5-b']dithiophen-2-yl)-6'-methyl-2,2'-dioxo-[3,3'-biindolinylidene]-1,1'-dicarboxylate. (**99% yield**)

Chapter 4 Summary and Future Direction

In conclusion, two different applications were explored in this thesis with the aim to improve performance. The first application addresses organic solar cells that utilizes renewable solar energy as a way to combat global emissions and conserve natural resources. While the second application addresses organic thin film transistors to be useful for sensors. Both of the applications involve novel heterocyclic aromatic amide donor-acceptor polymers, hemi-isoindigo and isoindigo with the substitution of long carbamate side chains to demonstrate the potential influence on efficiency and performance for solar cell and transistor application, respectively.

In the third chapter of this thesis, it addressed a novel C24 carbamate chain substituted TEIBDT as the active polymer donor to be used in a BHJ OSC device. It exhibits a very coplanar structure, has straight-forward synthesis as well as high quenching efficiency making it a great candidate for OSC's. The solar cell device based on TEIBDT: Y6 blend film showed an adequate efficiency of 8.00% with J_{SC} of 20.60 $mAcm^{-2}$, V_{OC} of 0.70V and FF of 0.56%. The carrier mobilities of the film for hole and electron were calculated to be 1.06×10^{-4} and 8.855×10^{-6} $cm^2V^{-1}s^{-1}$, respectively. The acceptable PCE are attributed to good film morphology with good crystallinity. Although the PCE isn't very high, it does prove that the carbamate chain can be viable for other polymer donors that already exhibit high PCE. To further improve on this structure, a higher degree of crystallinity can be attained by introducing a fluorinated BDT donor. This would enhance the electron mobility and balance the ratio between electron and hole mobility to attain a better J_{SC} as well as deepening the E_{HOMO} level further to enhance the $V_{OC.}$

The fourth chapter of the thesis focuses on three novel carbamate substituted isoindigo polymers, PIDMT, PIDBT and PIDBDT for the use in organic thin film transistors. The impact of the thermo-cleavable carbamate chain was studied for the enhancement of mobility, solvent resistance, and morphological stability. With regards to solvent resistance, all the polymers exhibited resistance towards processing solvents such as chloroform and toluene when annealed at 250 ºC. In terms of performance, the PID polymers displayed ambipolar characteristics with p-type mode being the dominant function. The mobility performance for PIDMT, PIDBT and PIDBDT are the following 0.004, 0.01 and 0.007 $cm^2V^{-1}s^{-1}$, respectively for p-type and 0.001, 0.004, 0.005 $cm^2V^{-1}s^{-1}$, respectively for n-type with PIDBT being dominant for both modes. The low mobilities are attributed to the amorphous nature of the polymer as well as their small grain size not being well connected. To further improve these polymers, the degree of crystallinity should be the focusing factor. Different substituents, such as the addition of halogenic atoms can achieve higher mobility due to the extension of the conjugation by the participation of the atoms in the LUMO energy wave functions of the polymers.

References

[1] Le Quere, C., Anew, R. M., Friedlingstein, P., Sitch, S., Hauck, J., Pongratz, J., Canadell, J. G. (2018). Global Carbon Budget 2018. Earth System Science Data, 10(4), 2141–2194. https://doi.org/10.5194/essd-10-2141-2018

[2] Federal Information & News Dispatch, LLC. (2022). Inventory of U.S. Greenhouse Gas Emissions and Sinks: 1990-2020. In The Federal Register / FIND (Vol. 87, p. 8583–). Washington.

[3] Dincer, Colpan, C. O., & Kadioglu, F. (2013). *Causes, Impacts and Solutions to Global Warming (Dincer, C. O. Colpan, & F. Kadioglu, Eds.; 1st ed. 2013.). Springer New York.* https://doi.org/10.1007/978-1-4614-7588-0

[4] He, Y. (2017). Novel N-Type π-Conjugated Polymers for All-Polymer Solar Cell. *University of Waterloo.*

[5] Iqbal, M. A. , Malik, M., Shahid, W., Din, S. Z. U. , Anwar, N., Ikram, M., & Idrees, F. *(2022).* Materials for Photovoltaics: Overview, Generations, Recent Advancements and Future Prospects. *In B. Zaidi, & C. Shekhar (Eds.), Thin Films Photovoltaics.* IntechOpen. https://doi.org/10.5772/intechopen.101449

[6] El Chaar, L., lamont, L. & El Zein, N. (2011). Review of photovoltaic technologies. *Renewable & Sustainable Energy Reviews*, *15*(5), 2165–2175. https://doi.org/10.1016/j.rser.2011.01.004

[7] Badawy, W. A. (2015). A review on solar cells from Si-single crystals to porous materials and quantum dots. *Journal of Advanced Research*, *6*(2), 123–132. https://doi.org/10.1016/j.jare.2013.10.001

[8] Hoppe, H., & Sariciftci, N. S. (2004). *Organic solar cells: An overview. Journal of Materials Research, 19(7)*, 1924–1945. https://doi.org/10.1557/JMR.2004.0252

[9] Yeh, N., & Yeh, P. (2013). Organic solar cells: Their developments and potentials. Renewable & Sustainable Energy Reviews, 21, 421–431. https://doi.org/10.1016/j.rser.2012.12.046

[10] Rafique, S., Abdullah, S. M., Sulaiman, K., & Iwamoto, M. (2018). Fundamentals of bulk heterojunction organic solar cells: An overview of stability/degradation issues and strategies for improvement. *Renewable and Sustainable Energy Reviews*, *84*, 43–53. https://doi.org/10.1016/j.rser.2017.12.008

[11] He, K., Kumar, P., Yuan, Y., & Li, Y. (2021). Wide bandgap polymer donors for high efficiency non-fullerene acceptor based organic solar cells. *Materials Advances*., 2021,2, 115-145, https://doi.org/10.1039/D0MA00790K

[12] Lu, L., Zheng, T., Wu, Q., Schneider, A. M., Zhao, D., & Yu, L. (2015). Recent advances in bulk heterojunction polymer solar cells. *Chemical Reviews*, *115*(23), 12666–12731. https://doi.org/10.1021/acs.chemrev.5b00098

[13] Lin, Y., Wang, J., Zhang, Z.-G., Bai, H., Li, Y., Zhu, D., & Zhan, X. (2015). An Electron Acceptor Challenging Fullerenes for Efficient Polymer Solar Cells. *Advanced Materials (Weinheim)*, *27*(7), 1170–1174. https://doi.org/10.1002/adma.201404317

[14] Liu, Q., Jiang, Y., Jin, K., Qin, J., Xu, J., Li, W., Xiong, J., Liu, J., Xiao, Z., Sun, K., Yang, S., Zhang, X., & Ding, L. (2020). 18% efficiency organic solar cells. *Science Bulletin.* ISSN 2095-9273. https://doi.org/10.1016/j.scib.2020.01.001.

[15] Bernardo, G., Melle-Franco, M., Washington, A. L., Dalgliesh, R. M., Li, F., Mendes, A., & Parnell, S. R. (2020). Different agglomeration properties of PC61BM and PC71BM in photovoltaic inks – a spin-echo sans study. *RSC Advances., 2020,10,* 4512-4520. https://doi.org/10.1039/C9RA08019H.

[16] Li, S., Sun, Y., Zhou, B., Fu, Q., Meng, L., Yang, Y., … Chen, Y. (2021). Concurrently Improved Jsc, Fill Factor, and Stability in a Ternary Organic Solar Cell Enabled by a C-Shaped Non-fullerene Acceptor and Its Structurally Similar Third Component. *ACS Applied Materials & Interfaces*, *13*(34), 40766–40777. https://doi.org/10.1021/acsami.1c13035

[17] Jain, A., & Kapoor, A. (2004). Exact analytical solutions of the parameters of real solar cells using Lambert W-function. *Solar Energy Materials and Solar Cells*, *81*(2), 269–277. https://doi.org/10.1016/j.solmat.2003.11.018

[18] Qi, B., & Wang, J. (2013). Fill factor in organic solar cells. *Physical Chemistry Chemical Physics : PCCP*, *15*(23), 8972–8982. https://doi.org/10.1039/c3cp51383a

[19] Deibel, C., & Dyakonov, V. (2010). Polymer–fullerene bulk heterojunction solar cells. *Reports on Progress in Physics*, *73*(9), 096401–. https://doi.org/10.1088/0034-4885/73/9/096401

[20] Nelson, J. H. & John H. (2003). *Nuclear magnetic resonance spectroscopy*. Upper Saddle River, NJ: Prentice Hall.

[21] Yoder, C. H., & Schaeffer, C. D. (1987). *Introduction to multinuclear NMR : theory and application*. Menlo Park, Calif. ;: Benjamin/Cummings

[22] Singh, M. K.& Singh, A., Chapter 14 - Nuclear magnetic resonance spectroscopy,

[23] Determann, H. (1968). Gel chromatography : gel filtration, gel permeation, molecular sieves : a laboratory handbook (2nd ed. 1968.). https://doi.org/10.1007/978-3-642-95082-7

[24] Hunt, B. J., & Holding, S. R. (1989). Size exclusion chromatography (1st ed. 1989.; B. J. Hunt & S. R. (Steve R. . Holding, Eds.). https://doi.org/10.1007/978-1-4615-7861-1

[25] Saadatkhah, N., Carillo Garcia, A., Ackermann, S., Leclerc, P., Latifi, M., Samih, S., … Chaouki, J. (2020). Experimental methods in chemical engineering: Thermogravimetric analysis—TGA. *Canadian Journal of Chemical Engineering*, *98*(1), 34–43. https://doi.org/10.1002/cjce.23673

[26] Ng, H. M.; Saidi, N. M.; Omar, F. S.; Ramesh, K.; Ramesh, S.; Bashir, S. Thermogravimetric Analysis of Polymers. *In Encyclopedia of Polymer Science and Technology; American Cancer Society*, 2018; pp 1–29. https://doi.org/10.1002/0471440264.pst667.

[27] *Thermal gravitational analysis (TGA) lab services*. Innovatech Labs. (2020, April 16). Retrieved, from https://www.innovatechlabs.com/materials-analysis-tga/

[28] Frederick, W. J.; Mentzer, C. C. Determination of Heats of Volatilization for Polymers by Differential Scanning Calorimetry. Journal of Applied Polymer Science 1975, 19 (7), 1799– 1804. https://doi.org/10.1002/app.1975.070190702.

[29] Gill, P., Moghadam, T. T., & Ranjbar, B. (2010). Differential scanning calorimetry techniques: applications in biology and nanoscience. *Journal of Biomolecular Techniques*, *21*(4), 167–193.

[30] Granite, S. by. (2020, April 28). *UV vis spectroscopy: UV vis spectroscopy applications*. Edinburgh Instruments. https://www.edinst.com/techniques/uv-vis-spectroscopy/#:~:text=UV%2DVis%20Spectroscopy%20(or%20Spectrophotometry,a%20reference%20sample%20or%20blank.

[31] Admin. (2022, April 21). *Principle of UV-visible spectroscopy - detailed explanation.* BYJUS. Retrieved from https://byjus.com/chemistry/principle-of-uv-visible-spectroscopy/#:~:text=The%20Principle%20of%20UV%2DVisible,interaction%20between%20light%20and%20matter.

[32] Workman Jr, J. (Ed.). (2000). The handbook of organic compounds, three-volume set: Nir, ir, r, and uv-vis spectra featuring polymers and surfactants. Elsevier.

[33] Su, W.-F. (2013). *Principles of polymer design and synthesis*. Heidelberg: Springer.

[34] Costa, J. C. S., Taveira, R. J. S., Lima, C. F. R. A. C., Mendes, A., & Santos, L. M. N. B. F. (2016). Optical band gaps of Organic Semiconductor Materials. *Optical Materials, 58,* 51–60. https://doi.org/10.1016/j.optmat.2016.03.041

[35] Carriedo, G. A. (1988). The use of cyclic voltammetry in the study of the chemistry of metal-carbonyls: An introductory experiment. *Journal of Chemical Education, 65*(11), 1020–. https://doi.org/10.1021/ed065p1020

[36] Elgrishi, N., Rountree, K. J., McCarthy, B. D., Rountree, E. S., Eisenhart, T. T., & Dempsey, J. L. (2018). A Practical Beginner's Guide to Cyclic Voltammetry. Journal of Chemical Education, 95(2), 197–206. https://doi.org/10.1021/acs.jchemed.7b00361

[37] Camacho, R. Polarization Portraits of Light-Harvesting Antennas: From Single Molecule Spectroscopy to Imaging, 2014. https://doi.org/10.13140/2.1.4852.5607.

[38] De Jong, M. J. M., & Vissenberg, M. C. J. M. (1998). Theory of luminescence quenching and photobleaching in conjugated polymers. Philips journal of research, 51(4), 495-510.

[39] Kabongo, G. L., Mbule, P. S., Mhlongo, G. H., Mothudi, B. M., Hillie, K. T., & Dhlamini, M. S. (2016). Photoluminescence Quenching and Enhanced Optical Conductivity of P3HT-Derived Ho3+-Doped ZnO Nanostructures. *Nanoscale Research Letters*, *11*(1). https://doi.org/10.1186/s11671-016-1630-3

[40] Oreilly, J. (1975). Fluorescence experiments with quinine. Journal of Chemical Education, 52(9), 610–612. https://doi.org/10.1021/ed052p610

[41] *Yale University*. XRD | West Campus Materials Characterization Core. Retrieved from https://ywcmatsci.yale.edu/xrd

[42] Tadmor, Z., & Gogos, C. G. (1979). Principles of polymer processing. New York: Wiley.

[43] Eaton, P., & West, P. *(2010). Atomic force microscopy. Oxford: Oxford University Press*

[44] *How AFM works*. Atomic Force Microscope Principle | AFM Scanning | How AFM Works. from https://parksystems.com/medias/nano-academy/how-afm-works

[45] Alcácer, L. (2018). Electronic structure of organic semiconductors : polymers and small molecules. https://doi.org/10.1088/2053-2571/aaddd8

[46] Katariya, A., & Rani, J. (2021). Review on two-dimensional organic semiconductors for thin film transistor application. *Materials Today : Proceedings*, *46*, 2322–2325. https://doi.org/10.1016/j.matpr.2021.04.401

[47] Zehra, N., Adil, L. R., Tanwar, A. S., Mondal, S., & Iyer, P. K. (2021). Chemical Solution Synthesis for Materials Design and Thin Film Device Applications. *Thin-film devices for chemical, biological, and diagnostic applications*. https://doi.org/10.1016/B978-0-12-819718-9.00020-0

[48] Wu, X., Ma, Y., Zhang, G., Chu, Y., Du, J., Zhang, Y., … Huang, J. (2015). Thermally Stable, Biocompatible, and Flexible Organic Field-Effect Transistors and Their Application in Temperature Sensing Arrays for Artificial Skin. Advanced Functional Materials, 25(14), 2138–2146. https://doi.org/10.1002/adfm.201404535

[49] Elkington, D., Cooling, N., Belcher, W., Dastoor, P., & Zhou, X. (2014). Organic Thin-Film Transistor (OTFT)-Based Sensors. *Electronics*, *3*(2), 234–254. https://doi.org/10.3390/electronics3020234

[50] Reese, C., Roberts, M., Ling, M.-mang, & Bao, Z. (2004). Organic thin film transistors. *Materials Today*. *7, 9, 20-27,* ISSN 1369-7021. https://doi.org/10.1016/S1369-7021(04)00398-0.

[51] Newman, C. R., Frisbie, C. D., da Silva Filho, D. A., Brédas, J.-L., Ewbank, P. C., & Mann, K. R. (2004). Introduction to Organic Thin Film Transistors and Design of n-Channel Organic Semiconductors. *Chemistry of Materials*, *16*(23), 4436–4451. https://doi.org/10.1021/cm049391x

[52] Yusof, N. S., Mohamed, M. F. P., Ghazali, N. A., Khan, M. F. A. J., Shaari, S., & Mohtar, M. N. (2022). Evolution of solution-based organic thin-film transistor for healthcare monitoring– from device to Circuit Integration: A Review. *Alexandria Engineering Journal. 61, 12,* Pages 11405-11431, https://doi.org/10.1016/j.aej.2022.05.013

[53] Zhu, J., & Li, Y. (2018). *Organic thin-film transistor based gas sensors for putrescine detection*. University of Waterloo, Waterloo, Ontario, Canada.

[54] Hamwi, S., Riedl, T., & Kowalsky, W. (2011). An organic p-i-n homojunction as ultra violet light emitting diode and visible-blind photodiode in one. *Applied Physics Letters*, *99*(5), 053301–053301–3. https://doi.org/10.1063/1.3617427

[55] Liu, J., Engquist, I., Crispin, X., & Berggren, M. (2012). Spatial Control of p–n Junction in an Organic Light-Emitting Electrochemical Transistor. *Journal of the American Chemical Society*, *134*(2), 901–904. https://doi.org/10.1021/ja210936n

[56] FESSER, K., BISHOP, A. R., & CAMPBELL, D. K. (1983). Optical absorption from polarons in a model of polyacetylene. *Physical Review. B, Condensed Matter*, *27*(8), 4804–4825. https://doi.org/10.1103/PhysRevB.27.4804

[57] Cavallari, M. R., Pastrana, L. M., Sosa, C. D. F., Marquina, A. M. R., Izquierdo, J. E. E., Fonseca, F. J., … Kymissis, I. (2020). Organic Thin-Film Transistors as Gas Sensors: A Review. *Materials*, *14*(1), 3–. https://doi.org/10.3390/ma14010003

[58] Agarwal, I., Agrawal, A., & Gupta, N. (2021). Organic Thin Film Transistors: Device Architecture, Material Selection and Modelling. 2021 IEEE Madras Section Conference (MASCON), 1–5. https://doi.org/10.1109/MASCON51689.2021.9563536

[59] Banerjee, S., & Tyagi, A. K. (2011). Functional materials : preparation, processing and applications (First edition.; S. (Srikumar) Banerjee & A. K. Tyagi, Eds.). London ;: Elsevier.

[60] Deng, P., & Zhang, Q. (2014). Recent developments on isoindigo-based conjugated polymers. *Polymer Chemistry, 5*(1), 3298–3335. https://doi.org/10.1039/c3py01598j

[61] Wang, E., Mammo, W., & Andersson, M. R. (2014). 25th Anniversary Article: Isoindigo-Based Polymers and Small Molecules for Bulk Heterojunction Solar Cells and Field Effect Transistors. *Advanced Materials (Weinheim), 26*(12), 1801–1826. https://doi.org/10.1002/adma.201304945

[62] Bogdanov, A. V., & Mironov, V. F. (2021). Recent advances in the application of isoindigo derivatives in materials chemistry. *Beilstein Journal of Organic Chemistry. 17,* 1533–1564. https://doi:10.3762/bjoc.17.111

[63] Lu, C. F., Shih, C.W., Chen, C. A., Chin, A.& Su, W.F.(2018) Tuning the Morphology of Isoindigo Donor Acceptor Polymer Film for High Sensitivity Ammonia Sensor. *Advanced Functional Materials,* 28(40):1803145. https://doi.org/10.1002/adfm.201803145

[64] Ding, Y., Jiang, L., Du, Y., Kim, S., Wang, X., Lu, H., Qiu, L. (2020). Linear hybrid siloxane-based side chains for highly soluble isoindigo-based conjugated polymers. *Chemical Communications (Cambridge, England), 56*(79), 11867–1187. https://doi.org/10.1039/d0cc01497d

[65] Ashraf, R. S., Kronemeijer, A. J., James, D. I., Sirringhaus, H., & McCulloch, I. (2012). A new thiophene substituted isoindigo based copolymer for high performance ambipolar transistors. *Chemical Communications (Cambridge, England), 48*(33), 3939–3941. https://doi.org/10.1039/c2cc30169e

[66] Randell, N. M., & Kelly, T. L. (2019). Recent Advances in Isoindigo-Inspired Organic Semiconductors. *Chemical Record*, *19*(6), 973–988. https://doi.org/10.1002/tcr.201800135

[67] Wu. J., Chen. J., Huang. H., Li. S., Wu. H., Hu C., Tang. J. & Zhang Q. (2016). (Z)-(Thienylmethylene)oxindole-Based Polymers for High-Performance Solar Cells. *Macromolecules 2016, 49, 6, 2145–2152* https://doi.org/10.1021/acs.macromol.5b02780

[68] Li, H., Sun, R., Wang, W., Wu, Y., Wang, T., & Min, J. (2020). Simple (thienylmethylene)oxindole-based polymer materials as donors for efficient non-fullerene polymer solar cells. *Nano Select*, *2*(2), 417–424. https://doi.org/10.1002/nano.202000198

[69] Jia, Z., Qin, S., Meng, L., Ma, Q., Angunawela, I., Zhang, J., Li, Y. (2021). High performance tandem organic solar cells via a strongly infrared-absorbing narrow bandgap acceptor. *Nature Communications*, *12*(1), 178–178. https://doi.org/10.1038/s41467-020-20431-6

[70] Qiu, D., Adil, M. A., Lu, K., & Wei, Z. (2020). The Crystallinity Control of Polymer Donor Materials for High-Performance Organic Solar Cells. *Frontiers in Chemistry*, *8*, 603134–603134. https://doi.org/10.3389/fchem.2020.603134

[71] Yeh, M.-L., Wang, S.-Y., Martínez Hardigree, J. F., Podzorov, V., & Katz, H. E. (2015). Effect of side chain length on film structure and electron mobility of core-unsubstituted pyromellitic diimides and enhanced mobility of the dibrominated core using the optimized side chain. *Journal of Materials Chemistry. C, Materials for Optical and Electronic Devices*, *3*(13), 3029–3037. https://doi.org/10.1039/C4TC02611J

[72] Abdulahi, B. A., Li, X., Mone, M., Kiros, B., Genene, Z., Qiao, S., Mammo, W. (2019). Structural engineering of pyrrolo[3,4-]benzotriazole-5,7(2,6)-dione-based polymers for non-fullerene organic solar cells with an efficiency over 12. *Journal of Materials Chemistry. A, Materials for Energy and Sustainability*, *7*(33), 19522–1953. https://doi.org/10.1039/c9ta06385d

[73] Knopfmacher, O., Hammock, M. L., Appleton, A. L., Schwartz, G., Mei, J., Lei, T., Bao, Z. (2014). Highly stable organic polymer field-effect transistor sensor for selective detection in the marine environment. *Nature Communications*, *5*(1), 2954–2954. https://doi.org/10.1038/ncomms3954

[74] Lu, C., Shih, C., Chen, C., Chin, A., & Su, W. (2018). Tuning the Morphology of Isoindigo Donor–Acceptor Polymer Film for High Sensitivity Ammonia Sensor. *Advanced Functional Materials*, *28*(40), 1803145–n/a. https://doi.org/10.1002/adfm.201803145

[75] Soylemez, Goker, S., & Toppare, L. (2019). A newly designed anthracene and isoindigo based polymer: synthesis, electrochemical characterization and biosensor applications. *New Journal of Chemistry, 43(35), 13979–13984.* https://doi.org/10.1039/c9nj02546d

[76] Dharmapurikar, Arulkashmir, A., Mahale, R. Y., & Chini, M. K. (2017). Synthesis of amphiphilic isoindigo co-polymers for organic field effect transistors: A comparative study. *Journal of Applied Polymer Science, 134(43).* https://doi.org/10.1002/app.45461

[77] Ngai, Polena, J., Afzal, D., Gao, X., Kapadia, M., & Li, Y. (2022). Green Solvent-Processed Hemi-Isoindigo Polymers for Stable Temperature Sensors. Advanced Functional Materials, 32(17), 2110995–n/a. https://doi.org/10.1002/adfm.202110995

[78] Ngai, Gao, X., Kumar, P., Polena, J., & Li, Y. (2021). A Highly Stable Diketopyrrolopyrrole (DPP) Polymer for Chemiresistive Sensors. Advanced Electronic Materials, 7(3), 2000935–n/a. https://doi.org/10.1002/aelm.202000935